Design and performance of fiber-optic light-transmitting cementitious composites

by

Karina HWANG ARCOLEZI

MANUSCRIPT-BASED THESIS PRESENTED TO ÉCOLE DE TECHNOLOGIE SUPÉRIEURE IN PARTIAL FULFILLMENT FOR THE DEGREE OF DOCTOR OF PHILOSOPHY
Ph.D.

MONTREAL, SEPTEMBER 9, 2026

ÉCOLE DE TECHNOLOGIE SUPÉRIEURE
UNIVERSITÉ DU QUÉBEC

BOARD OF EXAMINERS

THIS THESIS HAS BEEN EVALUATED

BY THE FOLLOWING BOARD OF EXAMINERS

Dr. Claudiane Ouellet-Plamondon, Thesis Supervisor
Department of Construction Engineering, École de technologie supérieure

Dr. Bora Ung, Thesis Co-supervisor
Department of Electrical Engineering, École de technologie supérieure

Dr. Camille Coti, President of the Board of Examiners
Department of Software Engineering and IT, École de technologie supérieure

Dr. Andy Shih, Member of the jury
Department of Electrical Engineering, École de technologie supérieure

Dr. João Claudio Bassan de Moraes, External Evaluator
Civil Engineering Division, Aeronautics Institute of Technology, Brazil

THIS THESIS WAS PRESENTED AND DEFENDED

IN THE PRESENCE OF A BOARD OF EXAMINERS AND PUBLIC

JULY 14, 2026

AT ÉCOLE DE TECHNOLOGIE SUPÉRIEURE

ACKNOWLEDGEMENTS

A Ph.D. is built slowly, through experiments that work and many that do not, and through people who make the path lighter. I am grateful to all who were part of this journey.

I would like to express my sincere gratitude to my Ph.D. directors, Prof. Dr. Claudiane Ouellet-Plamondon and Prof. Dr. Bora Ung, for their guidance, scientific rigor, and trust throughout this process. I also thank the jury members for their careful evaluation of this thesis and defense.

I am thankful to the laboratory technicians, especially Jonathan Auger, Mauricio Rios, and Sébastien Ménard, for their practical knowledge and support.

A big thank you to my colleagues and friends for the shared moments in laboratories, offices, and corridors. I am especially grateful to Camila for sharing moments of doubt, laughter, and exhaustion that made this journey lighter and more meaningful. I also thank Marco, Johnson, Jessica, Alberto, and Victor for their exchanges, and Giuliane for her constant friendship.

To my family, thank you for being my foundation. And to my husband Douglas, thank you for your patience, partnership, and belief in me, even on the days I could not believe in myself.

This research was supported by the Fonds de recherche du Québec – Nature and Technologies (FRQNT) (grant 370841), the Art Prisme programme (2022-ART-317342), and the Natural Sciences and Engineering Research Council of Canada (NSERC) (Science Exposed contest and Discovery Program). Additional support was provided by the Canada Research Chair Program (CRC-2019-00074) and the ÉTS Research Chair in Engineering Marcelle-Gauvreau.

To everyone who shared this process in ways large and small, thank you, merci, obrigada!

Conception et performance des composites cimentaires à fibres optiques transmissifs à la lumière

Karina HWANG ARCOLEZI

RÉSUMÉ

L'intégration de fibres optiques dans des matrices cimentaires est une approche prometteuse pour développer des matériaux alliant performance structurale et fonctionnalités optiques, avec des applications en éclairage naturel, en détection et en transfert d'information. Le domaine reste fragmenté : la terminologie, les méthodes expérimentales et l'interprétation des résultats varient d'une étude à l'autre, ce qui complique les comparaisons et freine le développement d'approches de conception communes. Cette thèse étudie les composites cimentaires à fibres optiques en reliant la conception du matériau, le comportement optique et la performance mécanique dans un cadre unifié, à partir d'une approche expérimentale et analytique. Dans un premier temps, la fiabilité des mesures de transmittance optique est examinée en analysant l'effet de la configuration expérimentale, notamment la distance entre le détecteur et l'échantillon. Les résultats montrent que ces conditions de mesure influencent significativement les valeurs obtenues, ce qui explique en partie la variabilité entre études. Une méthode basée sur la distribution spatiale de la lumière sortant des fibres intégrées dans la matrice est alors proposée. Elle offre une base cohérente pour la caractérisation optique et améliore la reproductibilité des mesures, tout en proposant une meilleure standardisation dans le domaine. Dans un deuxième temps, le comportement mécanique des composites avec fibres optiques est étudié par une analyse expérimentale comparative. Des échantillons avec fibres sont comparés à des échantillons avec cavités préformées de géométrie équivalente, ce qui permet de distinguer les effets du matériau de ceux liés à la géométrie. Les résultats montrent que l'interaction fibre-matrice et la perturbation géométrique contribuent toutes deux à la réponse mécanique, dans des proportions qui varient selon les conditions de chargement et la composition de la matrice. Enfin, pour aller au-delà de la simple transmission de lumière, des configurations de fibres alternatives sont explorées. Un composite à fibres optiques distribuées aléatoirement est développé, montrant qu'il est possible de modifier la propagation de la lumière pour préserver la confidentialité visuelle tout en maintenant la transmission lumineuse. Une approche de reconstruction numérique montre également que l'information brouillée par la disposition aléatoire des fibres peut être récupérée par traitement informatique, positionnant ces composites comme des systèmes hybrides physico-numériques. Dans l'ensemble, ce travail propose une compréhension cohérente des composites cimentaires à fibres optiques en liant caractérisation optique, comportement mécanique et conception du matériau, et établit des principes de conception pour des matériaux cimentaires multifonctionnels intégrant performance optique, structurale et capacités numériques.

Mots-clés : mortiers transmetteurs de lumière, transmittance optique, propriétés mécaniques, interaction fibre-matrice, béton multifonctionnel

Design and performance of fiber-optic light-transmitting cementitious composites

Karina HWANG ARCOLEZI

ABSTRACT

The integration of optical fibers into cementitious matrices offers a promising way for developing materials that combine structural performance with optical functionalities, enabling applications in architectural daylighting, sensing, and information transfer. The subject remains fragmented, with inconsistencies in terminology, experimental methodologies, and interpretation of results, limiting the development of unified design approaches and challenging comparison across studies. This thesis investigates fiber-optic cementitious composites by relating material design, optical behavior, and mechanical performance within a unified framework, using a combined experimental and analytical approach. First, the reliability of optical transmittance measurements is evaluated by analyzing the influence of experimental configuration, particularly the detector-sample distance. Experimental results show that measurement conditions significantly affect reported transmittance values, contributing to variability across studies. To address this, a physically grounded methodology based on the spatial distribution of light emerging from embedded optical fibers is developed. This approach provides a consistent basis for optical characterization and improves measurement reproducibility, thus proposing a practical contribution toward standardization in the field. Second, the mechanical behavior of composites containing embedded optical fibers is investigated through comparative experimental analysis. Samples with fibers are evaluated alongside samples containing preformed holes of equivalent geometry, enabling the separation of material and geometric effects. The results show that both fiber-matrix interaction and geometric disruption influence the mechanical response, with their relative contributions depending on loading conditions and matrix composition. Finally, to extend the functionality of these materials beyond passive light transmission, alternative fiber configurations are explored. A composite with randomly distributed optical fibers is developed, demonstrating that light propagation can be modified to achieve visual privacy while maintaining light transmission. A computational reconstruction approach further demonstrates that information scrambled by the random fiber arrangement can be digitally recovered, positioning these composites as hybrid physical-digital systems. Overall, this work provides a coherent understanding of fiber-optic cementitious composites by linking optical characterization, mechanical behavior, and material design, and establishes design principles for multifunctional cementitious materials integrating optical and structural performance with emerging digital capabilities.

Keywords: light-transmitting mortars, optical transmittance, mechanical properties, fiber-matrix interaction, multifunctional concrete

TABLE OF CONTENTS

Page

LIST OF TABLES

LIST OF FIGURES

LIST OF ABBREVIATIONS AND ACRONYMS

ASTM	American society for testing and materials
CC	Calcined clay
CSA	Canadian standards association
GOF	Glass optical fiber
ITZ	Interfacial transition zone
LC^3	Limestone calcined clay cement
LED	Light emitting diode
LF	Limestone filler
LTC	Light-transmitting concrete
LTCC	Light-transmitting cementitious composites
MK	Metakaolin
NA	Numerical aperture
NCC	Normalized cross-correlation
OPC	Ordinary Portland cement
PMMA	Polymethyl methacrylate
POF	Polymer/plastic optical fiber
RGB	Red green blue
SEM	Scanning electron microscopy
SP	Superplasticizer
TIR	Total internal reflection
UHPC	Ultra-high performance concrete

LIST OF SYMBOLS AND UNITS OF MEASUREMENT

%	Percent
°C	Degrees Celsius
μW	Microwatts
cm	Centimeters
C-S-H	Calcium silicate hydrate
dB/cm	Decibels per centimeter
dB/mm	Decibels per millimeter
D_s	Characteristic sample dimension
E_{rec}	Reconstruction error
H	Homography matrix
I(r)	Light intensity at radius r
I_0	Peak light intensity
K	Attenuation factor
kg/m³	Kilograms per cubic meter
L	Optical fiber length
M	Mapping matrix
mm	Millimeters
MPa	Megapascal
N	Number of optical fibers
n	Super-Gaussian parameter
n_1	Refractive index (optical fiber's core)

n_2	Refractive index (optical fiber's cladding)
Ø	Diameter
P	Light power
P_0	Incident light power
R	Radial distance
S_{fiber}	Fiber cross-sectional area
S_{sample}	Sample surface area
T	Light transmittance
T_{fiber}	Fiber transmission
T_{max}	Maximum transmittance
w	Beam radius
W	Watts
W/m^2	Watts per square meter
z	Distance between sample and detector cm
Z	propagation distance
Z_{opt}	Optimal detection distance
α	Transmission loss coefficient
Θ	Acceptance angle

INTRODUCTION

While cementitious materials are traditionally designed to fulfill structural functions, with limited consideration for functionalities beyond mechanical performance and durability, there is increasing interest in expanding their capabilities to include additional functionalities. In recent years, the development of multifunctional construction materials has gained increasing attention, particularly in the context of sustainable and smart infrastructure. Among these materials, cementitious composites incorporating optical fibers have been investigated as systems capable of transmitting light while also providing load-bearing capacity and additional functionalities (Chiew, Ibrahim, Sarbini, et al., 2020).

These light-transmitting cementitious composites introduce the possibility of integrating optical behavior into construction materials, enabling applications ranging from architectural daylighting to sensing and information transfer (Al-Sodani, 2025; Makul, 2020). While this potential is significant, the field is still characterized by variations in terminology, experimental methodologies, and interpretation of results. This variability can limit the development of generalized design approaches and make it more challenging to directly compare findings across studies (Bai, Zhang, Tian, Wu, & Zheng, 2024; Henriques, Dal Molin, & Masuero, 2018).

0.1 Research context and motivation

Light transmission in cementitious composites can be achieved through different approaches, including the use of optical fibers, the incorporation of waste glass particles or translucent resin-based phases (Chiew, Ibrahim, Sarbini, et al., 2020). In fiber-based systems, it is enabled by the incorporation of discrete optical fibers embedded within an otherwise opaque matrix. These fibers guide light by total internal reflection, allowing visible light to propagate through the material while the surrounding cementitious phase maintains structural continuity (Chiew, Ibrahim, Mohd Ariffin, Lee, & Singh, 2020; Kasap, 2018). Over the past two decades, research has investigated many of optical fiber types, matrix compositions, and fabrication methods, with applications including architectural elements, daylighting strategies, and structural health monitoring systems (Al-Sodani, 2025).

The integration of optical fibers into cementitious materials introduces a coupled interaction between optical performance and mechanical behavior. Parameters such as fiber content, diameter, spatial distribution, and interface characteristics influence both light transmission and structural response, often in competing ways (Henriques et al., 2018; Henriques, Dal Molin, & Masuero, 2020; Nam et al., 2024; Tahwia, Abdelaziz, Samy, & Amin, 2022; Tuaum, Shitote, & Oyawa, 2018). At the same time, significant variability exists in experimental methodologies across the literature, including differences in specimen geometry, fabrication procedures, optical measurement setups, and mechanical testing protocols. This variability affects reported optical transmittance values, mechanical performance, and overall reproducibility, limiting the ability to establish consistent relationships between material design and observed behavior (Al-Sodani, 2025; Bai et al., 2024; Chiew, Ibrahim, Mohd Ariffin, et al., 2020).

Within this context, a comprehensive understanding of fiber-optic cementitious composites requires approaches that address these aspects jointly, instead of treating them in isolation (Chiew, Ibrahim, Mohd Ariffin, et al., 2020). In particular, there is a need to better relate material design parameters, experimental conditions, and observed responses coherently, in order to support more consistent interpretation of results and to clarify how these systems can be effectively designed for multifunctional applications (Al-Sodani, 2025). This thesis describes new approaches towards linking optical characterization, mechanical behavior, and material design within a unified framework.

0.2 Research objectives

The overall objective of this thesis is to develop a coherent understanding of fiber-optic cementitious composites by relating material design, optical behavior, and mechanical performance, while exploring new functionalities enabled by alternative fiber configurations. To achieve this objective, the following specific objectives are defined:

(i) To improve the reliability and consistency of optical transmittance measurements in fiber-optic cementitious composites by investigating the influence of experimental configuration;
(ii) To analyze the mechanical behavior of these composites by distinguishing the contributions of fiber-matrix interaction and geometric disruption;
(iii) To explore advanced fiber arrangements capable of modifying light propagation and enabling additional functionalities, such as visual privacy, controlled information transfer, and digital image reconstruction.

These objectives are addressed through a combined experimental and conceptual approach, structured around the three research axes presented in Section 0.3 below.

0.3 Research framework and thesis approach

The development of fiber-optic cementitious composites involves interconnected challenges related to their optical characterization, mechanical behavior, and functional design. This thesis aims to address these aspects through a progressive approach, in which optical measurement reliability, material response, and system-level functionality are examined in a coherent sequence. Optical characterization and mechanical behavior are treated as complementary aspects of the material system, each requiring detailed investigation. The study of optical transmittance focuses on measurement consistency and interpretation, while the mechanical analysis examines the structural implications of embedding fibers in the cementitious matrix. Building on this understanding, the final stage extends the investigation toward functional material design, integrating optical and mechanical considerations to explore new capabilities.

Axis 1 – Optical transmittance: measurement and interpretation

A first limitation in the field concerns the characterization of optical transmittance. Reported transmittance values often vary significantly across studies, in part due to differences in experimental configurations that are not systematically addressed (Chiew, Ibrahim, Mohd Ariffin, et al., 2020). In particular, while previous studies have reported variations in measured light intensity with detector distance (Yue Li, Li, & Guo, 2015; Rong et al., 2023), the influence of detector positioning and light distribution remains insufficiently considered in a systematic manner. This raises the question of how measurement conditions affect the reported optical response, and how they can be defined to ensure consistent and representative results. To address this issue, the present work investigates the relationship between detector-sample distance and measured transmittance, combining experimental observations with a theoretical description of light distribution. This approach lays a physically grounded framework for improving the consistency and reproducibility of optical measurements.

Axis 2 – Mechanical behavior and constraints

The incorporation of optical fibers also affects the mechanical behavior of the cementitious matrix (Huynh Phuong Nam et al., 2022; Yue Li, Li, Wan, & Xu, 2015; Q. Lyu, Dai, & Chen, 2024; Nam et al., 2024; Tahwia et al., 2022). While previous studies report variations in strength associated with fiber inclusion, it remains unclear whether these effects arise primarily from interactions at the fiber-matrix interface or from the geometric disruption introduced by the inclusions themselves. This raises a fundamental question regarding the origin of mechanical changes and their dependence on loading conditions and matrix composition. To clarify this issue, the mechanical behavior of embedded fibers is investigated through a comparative approach in which fiber-embedded samples are evaluated alongside specimens containing preformed voids of equivalent geometry. This methodology enables the separation of material and geometric contributions, providing insight into the mechanisms governing composites' mechanical performance.

Axis 3 – Functional material systems

Building on the previous stages of optical and mechanical characterization, a third aspect of the research explores how fiber configuration can be used to extend the functionality of these composites. Conventional designs typically rely on parallel fiber arrangements that maximize light transmission but may preserve spatial coherence, allowing visual perception through the material (Luhar et al., 2021). This limitation motivates the question of how light propagation can be modified to enable additional functionalities, such as visual privacy or controlled information transfer. In response, a novel composite design based on randomly distributed optical fibers is proposed. Unlike conventional parallel arrangements, this configuration simultaneously diffuses transmitted light to suppress visual recognition and enables the computational reconstruction of transmitted information, representing a conceptual shift from passive light-transmitting materials toward hybrid physical-digital systems with active information-encoding capabilities.

0.4 Scope and limitations

The experimental investigations were conducted on laboratory-scale specimens, which enabled the precise isolation of specific variables but do not yet account for macro-structural heterogeneity, long-distance light dispersion, and casting variability that arise at structural scales. The material scope was deliberately constrained to cementitious matrices based on a CSA-guided formulation containing 60% Portland cement and 40% supplementary cementitious materials such as limestone filler and metakaolin (Class N), as well as additional mixtures with varying cement contents aimed at reducing Portland cement usage, combined with poly(methyl methacrylate) optical fibers with a nominal diameter of 1 mm. This selection allowed for systematic and controlled comparison; conclusions, therefore, apply most directly to similar material-fiber combinations, and alternative matrices such as UHPC or geopolymers, or other fiber types such as glass optical fibers, would introduce different elasticity profiles and interfacial behaviors that fall outside the current scope. The effects of fiber material and diameter were not investigated, and the conclusions therefore apply specifically to the PMMA fiber type and diameter adopted in this work.

The mechanical decoupling methodology successfully isolates material adhesion and geometric disruption contributions under controlled static loading, though in real structural systems, additional coupled phenomena, including localized microcracking evolution, long-term matrix shrinkage, and dynamic stress redistribution, may coexist in ways that extend beyond the simplified conditions required for this baseline isolation. Similarly, optical characterization was performed under controlled configurations to establish a reproducible physical reference framework; in-situ architectural applications involve dynamic angular light incidence, spectral fluctuations, and variable surface conditions that require further environmental calibration of the proposed measurement approach.

Finally, the physical-digital framework demonstrates the feasibility of encoding and retrieving visual information through randomly distributed fiber networks under controlled imaging conditions, and scaling this methodology to industrial manufacturing environments will require robust algorithmic strategies capable of accommodating manufacturing imperfections and uncontrolled optical environments. Furthermore, this work focuses on short-term optical and mechanical properties; long-term durability aspects, including polymer fiber degradation under alkaline exposure, matrix aging, interfacial transition zone stability, thermal-expansion mismatch between the polymer fibers and the cementitious matrix under thermal cycling, and resistance to moisture, representing natural extensions of the present research.

0.5 Research dissemination

The research conducted in this thesis was disseminated through peer-reviewed journal publications, conference proceedings, and scientific photography, reflecting both the technical and interdisciplinary dimensions of the work.

Axis 1: The fundamental optical properties and measurement framework for light-transmitting concrete were established in:

"Experimental and theoretical investigation of optical transmittance in light-transmitting concrete." By Arcolezi, K. H., Zimmermann, C. A., Ung, B., Ouellet-Plamondon, C. (2026) Measurement science and technology (CHAPTER 2).

This study introduces a physically based model relying on a super-Gaussian intensity distribution to describe light emission from embedded optical fibers and establishes a reproducible framework for optical characterization.

Axis 2: The development of fiber-optic cementitious systems required a clear understanding of their mechanical implications. Early results on the mechanical influence of optical fibers were first presented in:

"Influence of optical fibres on mechanical properties of mortar mixes." By Arcolezi, K. H., Ouellet-Plamondon, C., Ung, B. (2024). Proceedings of the Canadian Society for Civil Engineering Annual Conference.

This initial study explored the impact of embedded fibers on mechanical performance and informed the experimental approach later developed in:

"Mechanical strengthening of cementitious composites by optical fibers through adhesion and geometric disruption" By Arcolezi, K. H., Brial, V., Ung, B., et al. (2026). Manuscript submitted (CHAPTER 3).

Axis 3: The functional capabilities of fiber-optic cementitious composites were investigated through both a consolidated material system and exploratory interactive applications. The main contribution in this area is presented in the following journal publication:

“Randomly distributed optical fibers in translucent mortar for privacy-preserving light transmission and digital image reconstruction.” By Arcolezi, K. H., Marion, V., Ung, B., et al. (2025). Scientific Reports (CHAPTER 4)

In parallel, additional conference contributions explored different interactive applications of fiber-optic cementitious systems:

“Interactive light- and sound-sensitive mortar for architectural environments.” By Arcolezi, K. H., Ouellet-Plamondon, C., Ung, B. (2025). In: ICCCBE 2024.

This study explores a light-transmitting mortar capable of responding to acoustic stimuli by converting sound signals into visual outputs through embedded optical fibers. The system combines a low-cement matrix with optical and electronic components, demonstrating the feasibility of transforming cementitious materials into responsive architectural elements.

“Touch-interactive concrete for smart structures.” By Arcolezi, K. H., Alonso Romero, A., Ben Zaid, H., Hamel, T., Ung, B., Ouellet-Plamondon, C. (2026). Accepted for publication in the Proceedings of CSCE Annual Conference (APPENDIX A).

This work presents a cementitious composite capable of detecting touch and movement gestures through embedded optical fibers. Variations in reflected light intensity, caused by physical contact, are processed using an optoelectronic system, enabling identification of user interactions within the material.

These contributions collectively illustrate the diversity of functional possibilities enabled by fiber-optic cementitious composites, ranging from information processing to interactive material behavior.

Axis 4: Visual and interdisciplinary contributions. Beyond traditional scientific dissemination, the developed materials were also explored through their visual and expressive potential. The optical behavior of the composites, in combination with controlled composition, lighting, and imaging conditions, enabled their use as subjects for scientific photography, resulting in multiple awards and distinctions.

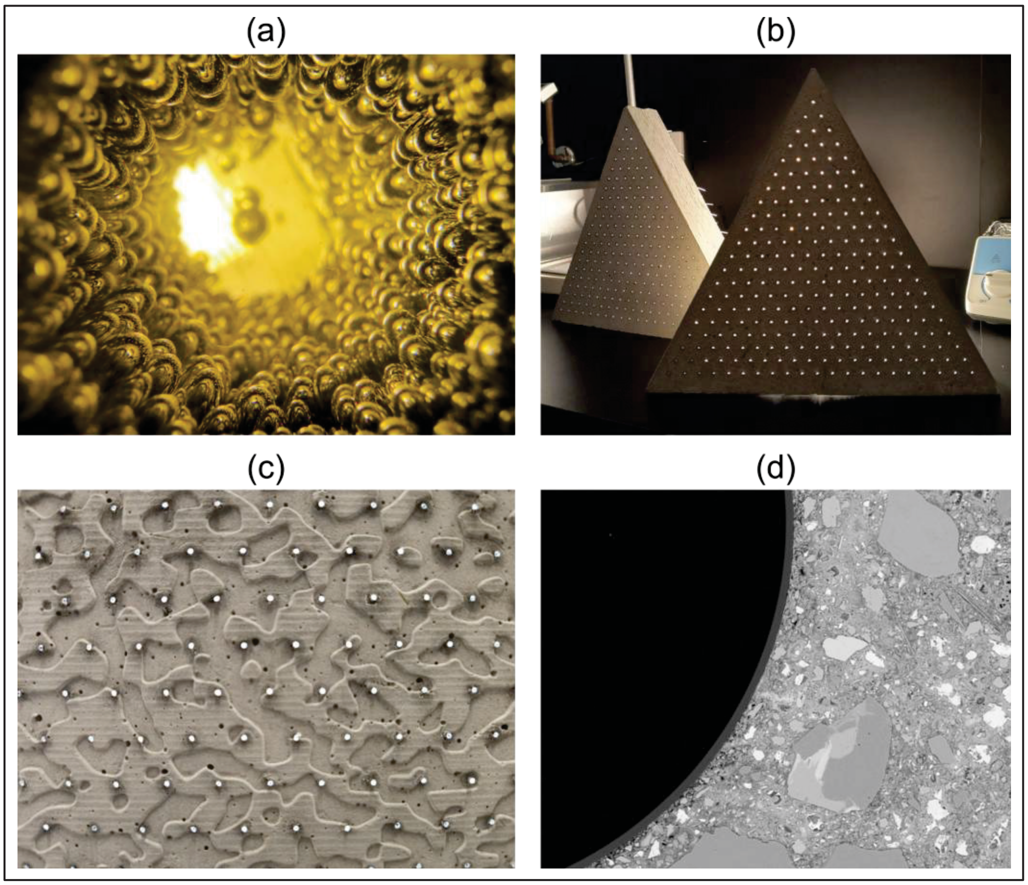

Figure 0.1 Scientific photography prizes and visual dissemination

(a) NSERC Science Exposed, jury prize (2024): This image captures an experimental attempt to use polydimethylsiloxane (PDMS), a silicon-based organic polymer, as an alternative light-transmitting medium within a cementitious composite, in contrast to the optical fibers used throughout this thesis. The resulting air bubbles, caused by fabrication limitations, highlight the challenges of combining materials with different properties. At the same time, they create unexpected visual effects.

(b) Triangular light-transmitting cementitious composites with optical fiber for an artistic exhibition – From Quantum Science to Artistic Experience, by the INTRIGO Collective, at the Exhibition Centre, Amos, QC (2025): This exhibition explores the translation of quantum science concepts into tangible, human-scale experiences through interactive and immersive artistic installations.

(c) ÉTS photo contest, art and culture category – Winner (2025): This image presents a textured mortar surface designed with a noise-like pattern. Light transmitted through embedded optical fibers highlights its contours, transforming this physical pattern into a perceptible surface that can be visually read and physically sensed. These samples were also featured at the artistic exhibition (Intrigo), showcasing six different texture patterns.

(d) Acfas, La preuve par l'image (2026), image selected among the 20 featured works: This scanning electron microscopy image shows the cross-section of an optical fiber embedded in a cementitious matrix, highlighting the interface between the fiber and the surrounding material.

0.6 Thesis outline

This thesis follows a manuscript-based format and is organized into four main chapters.

CHAPTER 1 presents a literature review on fiber-optic cementitious composites, establishing the conceptual framework and identifying key challenges related to optical behavior, mechanical performance, and fabrication methods.

CHAPTER 2 investigates the measurement of optical transmittance, focusing on the influence of experimental configuration and proposing a physically based approach for a more consistent characterization.

CHAPTER 3 analyzes the mechanical behavior of composites containing embedded optical fibers, with emphasis on distinguishing material interaction effects from geometric disruption under different loading conditions.

CHAPTER 4 explores an alternative material design based on randomly distributed optical fibers, addressing light diffusion, visual privacy, and the potential for digital reconstruction of transmitted information.

Finally, the conclusion synthesizes the main findings of the thesis, summarizing the results in relation to the overall and specific objectives. It is followed by recommendations for future research and a summary of contributions, including lists of journal articles, conference papers, posters, and awards that contributed to the dissemination of the research conducted during the doctoral studies.

CHAPTER 1

FIBER-OPTIC LIGHT-TRANSMITTING CEMENTITIOUS COMPOSITES: CLASSIFICATION FRAMEWORK, FABRICATION, AND PERFORMANCE

Abstract: Light-transmitting cementitious composites (LTCCs) have gained increasing interest as multifunctional construction materials. Light transmission in cementitious composites can be achieved through the incorporation of optical fibers within an otherwise opaque matrix, enabling simultaneous structural and optical functions in a single system. Over the past two decades of growing research, the available literature remains dispersed across different fabrication methods, test procedures, and terminology. This review investigates the current knowledge on LTCCs through the relationship between constituent materials, processing methods, and resulting performance. It consolidates fundamental concepts and recent advances to support a more coherent understanding of this material class and to clarify how material design influences optical and mechanical behavior. The study covers four main aspects: optical behavior, mechanical performance, fabrication methodologies, and application domains. It also discusses sources of variability in reported results, including differences in measurement approaches and experimental conditions, which affect the interpretation of experimental data. The review concludes with a discussion of current challenges and future perspectives, including standardization issues and opportunities for more systematic design approaches.

1.1 Introduction

Embedding optical fibers in a cementitious matrix to produce a structural element capable of transmitting light has been investigated since the early 2000s, when a Hungarian architect, Aron Losonczi demonstrated the feasibility of this concept through the commercial system LiTraCon (LitraCon®, 2026). The principle is straightforward: discrete fiber cores guide light through an otherwise opaque matrix by total internal reflection, allowing visible light to pass from one face of the element to the other while the surrounding cementitious phase maintains structural continuity (Al-Sodani, 2025; Bai, Zhang, Tian, Wu, & Zheng, 2024; Chiew, Ibrahim, Mohd Ariffin, et al., 2020; Luhar et al., 2021; Said, 2020). Over the following two decades, research expanded to include a range of fiber materials, including polymer optical fibers (POF), most commonly based on polymethyl methacrylate (PMMA) and glass optical fibers (GOF), embedded in matrices ranging from conventional Portland cement mortars (Yue Li, Xu, Gu, & Bao, 2012; Kavitha Karthikeyan, Keerthana, & Shanmugapriya, 2016) to ultra-high-performance concrete (Navabi, Javidruzi, Hafezi, & Mosavi, 2021) (UHPC), geopolymers, and sulfoaluminate cement systems (Yue Li, Li, & Guo, 2015). Commercial products have reached the market, architectural installations have been documented across multiple continents, and structural health monitoring through embedded fiber networks has emerged as another application with promising engineering value (Al-Sodani, 2025; Bai et al., 2024; Chiew, Ibrahim, Mohd Ariffin, et al., 2020; Qiao et al., 2023).

The material system presents a design challenge that is not common in conventional fiber-reinforced composites. The embedded inclusions must satisfy two independent functional requirements simultaneously. Optically, the fibers must transmit light with sufficient efficiency and spatial control to meet the intended application, whether for passive daylighting, aesthetic purposes, or sensor-integrated monitoring. Mechanically, their incorporation must not compromise the load-bearing capacity of the cementitious matrix beyond acceptable limits. These two requirements are not independent. Fiber volume fraction, diameter, surface condition, and spatial distribution all influence both optical transmittance (Altlomate, Alatshan, Mashiri, & Jadan, 2016; Henriques et al., 2018; Yue Li, Li, Wan, et al., 2015; Tuaum et al., 2018) and mechanical response (Huynh Phuong Nam et al., 2022; Yue Li, Li, Wan, et al., 2015; Nam et al., 2025, 2024; Tahwia et al., 2022; Tuaum, Shitote, Oyawa, & Biedebrhan, 2019), often in opposing directions. Increasing fiber content increases transmittance but also tends to introduce interfacial porosity, which reduces compressive and flexural strength (Bai et al., 2024; Li, Li, Wan, et al., 2015; Mei Chiew, Syahrizal Ibrahim, Azreen Mohd Ariffin, Lee, & Kumar Singh, 2022; Henriques et al., 2018, 2020; Nam et al., 2024). Although surface treatments can improve fiber-matrix bonding, they may disrupt optical coupling at the fiber ends (Chiew, Ibrahim, & Mohd Ariffin, 2024; Henriques et al., 2018; Shafei, Kazemian, Dopko, & Najimi, 2021). The fiber-matrix interface thus acts simultaneously as a mechanical discontinuity and an optical boundary, and its behavior under loading and environmental exposure remains insufficiently characterized.

At the same time, progress in light-transmitting cementitious composites has not yet led to a common methodology. No standardized protocols currently exist for fabrication procedures, optical transmittance measurement, or mechanical evaluation in fiber-embedded cementitious systems. Experimental configurations differ in instrumentation, specimen geometry, matrix composition, fiber content specification, and reporting format, often with insufficient details to reproduce the measurement conditions (Al-Sodani, 2025; Bai et al., 2024; Chiew, Ibrahim, Mohd Ariffin, et al., 2020; Henriques et al., 2018). As a result, direct comparison across studies remains limited, and performance trends that appear consistent within individual studies often become less clear when examined across the broader literature. This limitation reflects a broader issue in the field, where material response, fabrication conditions, and measurement configuration lack a consistent framework in reported results, that prevent a coherent interpretation across studies. Specifically, the field lacks a unified conceptual framework that links optical behavior, material design parameters, and mechanical performance. Existing studies tend to focus on isolated aspects, such as transmittance optimization or strength characterization, without establishing consistent relationships between these domains. As a result, the interpretation of reported results often depends on study-specific conditions, which limits a more global understanding of the key parameters, challenges and the development of generalized design guidelines.

In this context, this review summarizes the fundamental properties of fiber-optic light-transmitting cementitious composites (LTCCs) and discusses recent advances. The main objective is to establish a structured framework that connects optical transmission behavior with material design, fabrication methodology, and mechanical response, while explicitly addressing sources of variability in experimental results. The paper is organized around a framework that relates optical transmission behavior to material design, together with the key parameters that drive LTCC performance, including constituent materials, fabrication methods, optical and mechanical properties, durability, sustainability, current applications, and future research needs.

1.2 Terminology and classification framework

The designation of cementitious composites capable of transmitting light has not yet converged to a standardized terminology in literature. The terms *light-transmitting*, *transparent*, *translucent*, and, infrequently, *pellucid* appear across studies to describe the same class of material, yet one that leaves physically meaningful distinctions unaddressed. This is understandable in the absence of a formal nomenclature in this emerging field. However, these terms are not synonyms; and instead, each carries a specific meaning tied to the spatial distribution and coherence of the transmitted optical wavefront through the LTCC sample. The conflation of these concepts in technical literature is therefore more than an inconsistency of style, as it can affect how the optical behavior of these materials is interpreted, particularly when distinguishing between light intensity transmission and spatial information transmission. Early developments, including the work of Losonczi, who commercialized and marketed such systems under the designation "transparent concrete," have also influenced the terminology used in both commercial and academic contexts (LitraCon®*, 2026*; Losonczi & Bittis, 2005).

Table 1.1 shows the results of a bibliographic search conducted in the Scopus and Web of Science databases, which gives an overall assessment of the frequency in which the terms "light-transmitting", "translucent", "transparent", and "pellucid" are referenced in the published literature on LTCC research from 2000 to 2026. Each considered term was combined with cementitious material descriptors ("concrete", "mortar", "cement", "cementitious") and searched across titles, abstracts, and author keywords. Exclusion filters were applied to remove records from unrelated domains, including dentistry, transparent soils, resin-based cements, and non-cementitious systems. Results from both databases were merged, duplicates removed, to retain only studies on cementitious composites capable of transmitting light.

Table 1.1 Bibliometric search results by terminology term across Scopus and Web of Science, performed on July 2026

Term	**Dataset**
Light-transmitting	76
Translucent	67
Transparent	34
Pellucid	2

The annual distribution of publications (Figure 1.1a) indicates that research activity in LTCC has a marked increase from 2015 onward. No single term consistently dominates across the timeline, reflecting the absence of a shared reference framework rather than deliberate terminological choice. The patent literature offers a complementary perspective, reflecting terminological choices made in technological and commercial contexts. A search conducted in Google Patents, restricted to title-field occurrences of each term combined with cementitious material descriptors and covering the period 2000-2026, retrieved 185 records under “light-transmitting”, 21 under “translucent”, and 28 under “transparent”. The annual distribution of these records (Figure 1.1b) suggests a temporal pattern similar to that observed in the academic literature: activity across the three terms remained low until approximately 2015, after which “light-transmitting” became the most frequent designation in patent titles, particularly from 2018 onward. “Transparent” remained present throughout the timeline, in line with its historical use in the early dissemination and commercialization of these materials. “Translucent” appeared less frequently and more intermittently. Although patent terminology is influenced by legal, commercial, and search-strategy factors, these results provide additional support for adopting “light-transmitting” as the primary designation in the present review. For this reason, the terminology adopted in this review is based on definitions from classical optics which provide a reference for distinguishing transmission regimes.

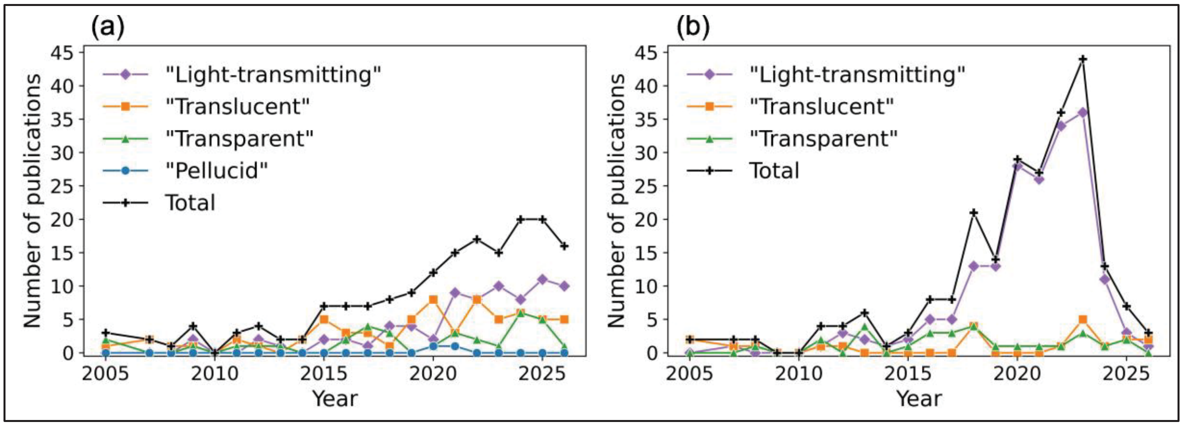

Figure 1.1 Annual record count by optical terminology term in (a) the academic literature (Scopus and Web of Science) and (b) the patent literature (Google Patents, title field, by priority year)

In optics, transparency denotes specular transmission, in which the spatial coherence of the wavefront is preserved, and an observer on the receiving side can resolve objects from the source side (Born & Wolf, 1999; Hecht, 2017). Translucency denotes diffuse transmission. In this case, light passes through the material, but internal scattering disrupts wavefront coherence, so perceived brightness and motion may be registered, but spatial resolution is mostly lost (Born & Wolf, 1999; Hecht, 2017; Wang et al., 2013). In opaque materials, incident flux I_0 is fully absorbed or scattered with no transmission (Tuaum et al., 2019). The term light-transmitting is used here in a broader sense, indicating that measurable visible-wavelength flux reaches the receiving face without implying any preservation of spatial information. These distinctions are schematically illustrated in Figure 1.2.

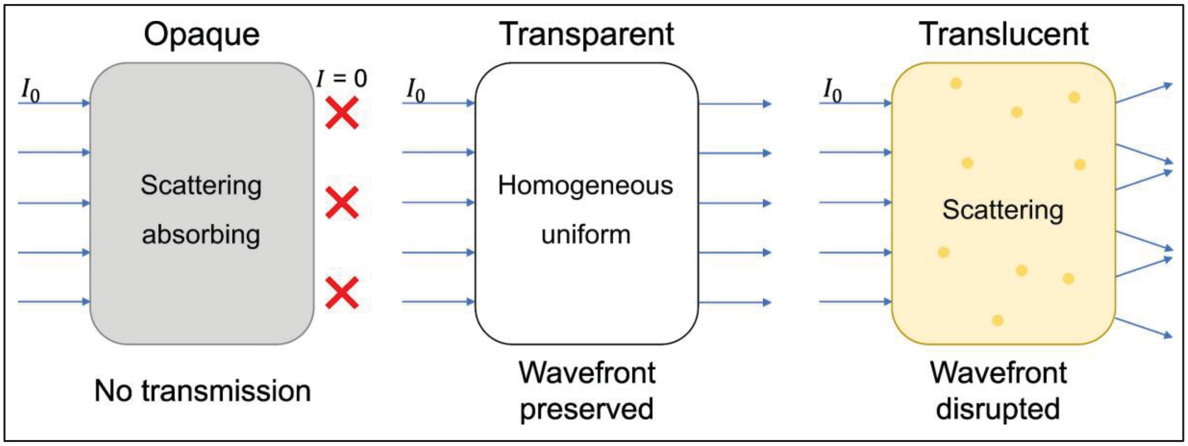

Figure 1.2 Schematic representation of optical transmission regimes: opaque, transparent, and translucent (I_0: incident light flux)

In fiber-based cementitious composites, light propagates through discrete optical fiber cores by total internal reflection, governed by the numerical aperture and the refractive index contrast between core and cladding (Kasap, 2018; Saleh & Teich, 2019). Transmission therefore occurs as a guided process along individual “cables” rather than as free-space propagation through the matrix, distinguishing these systems from intrinsically transparent materials such as glass or optical-grade resins (Chiew, Ibrahim, Mohd Ariffin, et al., 2020; Kasap, 2018). This mechanism influences the optical response at the macroscopic scale and provides the basis for the classification proposed here (Figure 1.3).

In this framework, composites are classified according to the optical outcome observed at the receiving face, rather than the internal transmission mechanism. Translucent systems preserve enough spatial definition for shapes and motion to be perceived, whereas light-transmitting systems, in a narrower sense, provide measurable luminance without preserving spatial information. The geometric configuration of the fiber network, including fiber trajectory, distribution pattern, and spatial arrangement, introduces an additional design dimension that influences which optical regime can be achieved for a given system, and is discussed in detail in Section 1.3.2.

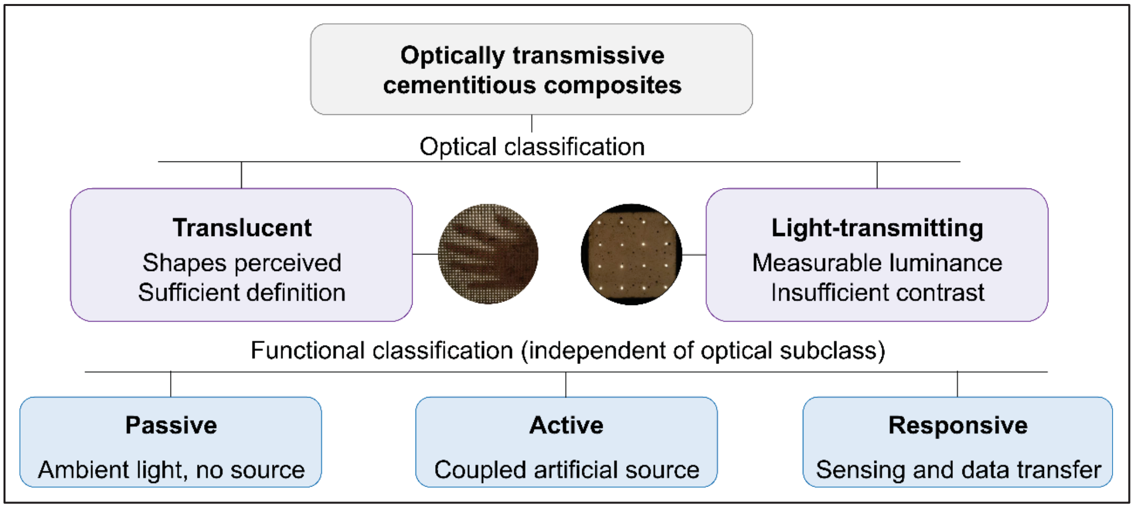

Figure 1.3 Proposed classification framework for optically transmissive cementitious composites

The term transparent concrete, while widely used in commercial and popular contexts, as reflected by the 34 records retrieved under this designation in the present search, does not align with the optical definition of transparency adopted here, since the matrix remains opaque and light are guided through discrete fiber channels rather than transmitted through a homogeneous medium. This terminology can be traced in part to its early use in the introduction and dissemination of the material, where naming conventions were influenced not only by physical description but also by communicative and commercial considerations. Its use in technical writing is noted where it appears in the sources reviewed. The present work adopts light-transmitting as the default designation, while the term translucent is used for systems in which spatial transmission has been directly reported by the authors or clearly documented through optical images of the transmitted pattern.

This distinction is relevant for the interpretation and comparison of results reported in the literature. Studies describing similar systems may appear to report different optical behavior depending on the terminology adopted, even though the underlying transmission mechanism is the same. The use of a consistent classification based on observable optical outcome can therefore support more reliable comparison between studies and clearer identification of design-performance relationships. It also provides a more direct link between material behavior and application requirements, particularly in cases where spatial information transmission is relevant.

Beyond optical classification, systems may be further characterized by their functional operational mode. Passive systems rely solely on ambient daylight without an auxiliary source and are primarily designed to reduce artificial lighting demand in architectural applications. Active systems are coupled to an external powered source, such as integrated light-emitting diodes (LEDs) or laser arrays, enabling controlled luminance output from the composite surface regardless of ambient conditions. Responsive systems represent a third operational mode in which the embedded fiber network extends beyond illumination to enable data transfer or structural health monitoring. In this configuration, the fiber act as a sensing medium where variations in light transmission, including attenuation, fiber Bragg grating-based measurements, or trajectory-encoded reconstruction, allow the composite to sense and respond to mechanical stress, structural cracking, or environmental stimuli (Inaudi, Posenato, & Glisic, 2005; Leung et al., 2015; Merzbacher, Kersey, & Friebele, 1996; Sharifi, Navabi, & Mosavi, 2023; Taheri, 2019). These operational modes relate to how light is used within the system rather than how it propagates and may therefore overlap within a single composite depending on the application context.

1.3 Constituent materials and design parameters

The performance of fiber-optic LTCCs is jointly determined by three material subsystems: the optical fibers that serve as discrete light-guiding elements, the cementitious matrix that provides structural continuity, and the interface between them. Each subsystem introduces design parameters that influence both the light transmission capacity and the load-bearing behavior of the composite, and their interactions are not independent. Changes in fiber geometry or surface condition, for example, influence both optical coupling efficiency and interfacial bonding, along with local matrix porosity. This section reviews the principal constituent types and the design parameters associated with each subsystem.

1.3.1 Optical fiber

Glass fibers and polymer optical fibers are the two main fiber types reported in optical fiber-based LTCC systems (Chiew, Ibrahim, Mohd Ariffin, et al., 2020). Fused silica glass fibers provide superior transmission over long distances and are widely used in telecommunications (Shafei et al., 2021; Snoeck, Debo, & De Belie, 2020); however, their application in LTCC is limited by higher cost and brittleness, which complicates handling during fabrication. In contrast, PMMA fibers are more commonly adopted in experimental and architectural LTCC systems owing to their lower cost, high flexibility (even for large fiber diameters), ease of cutting and installation, and overall practicality in embedding processes, as reported by Han, et al., (2017), and Chiew et al., (2020). Across the literature, the choice between glass and polymer fibers reflects a trade-off between optical efficiency and practical implementation. Glass fibers offer better intrinsic transmission properties, while polymer fibers are generally preferred in LTCC systems due to their compatibility with fabrication constraints and large-scale integration (Bai et al., 2024; Chiew, Ibrahim, Mohd Ariffin, et al., 2020; Momin, Kadiranaikar, Jagirdar, & Inamdar, 2014).

From a structural standpoint, an optical fiber consists of a transparent core with refractive index (n_1), surrounded by a cladding layer with a lower refractive index (n_2), as illustrated in Figure 1.4. The difference between the core/clad refractive indices ($n_2 < n_1$) enables light to be confined within the core and transmitted along the fiber length through the phenomenon of total internal reflection (TIR). The light coupling capability of the fiber is quantified by the numerical aperture (NA), which is expressed as $NA = \sqrt{n_1^2 - n_2^2}$ (Kasap, 2018). This parameter is directly associated with the acceptance cone angle ($\theta = arcsin(NA)$) shown in Figure 1.4, defining the maximum angle at which light can enter (or exit) the fiber and still be guided by total internal reflection.

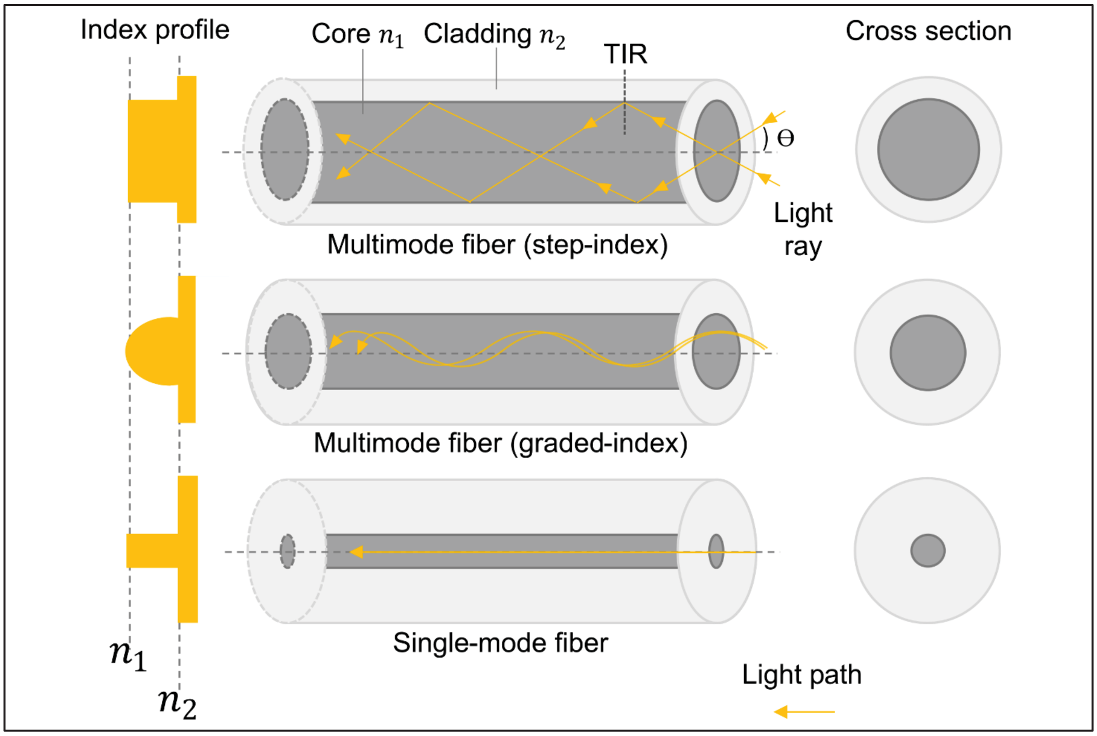

Figure 1.4 Schematic representation of an optical fiber and light propagation modes

In the context of design, this angular constraint influences both experimental configurations and reported transmittance values, particularly in setups where the incident light rays deviate strongly away from the fiber axis (Chiew et al., 2022). From a structural-optical perspective, multimode fibers are predominantly used in LTCC applications. Their higher numerical aperture (NA) increases the coupling of incident light over a wider range of angles, improving coupling efficiency under non-ideal alignment conditions (Su, Zhang, Liu, et al., 2022). In PMMA fibers, the acceptance angle is typically around 30°, meaning that incident light outside this angular range is not effectively guided through TIR, as discussed by (Huang & Lu, 2020; Su et al., 2022). This geometric constraint directly influences experimental configurations and contributes to the sensitivity in measured transmittance values.

Geometric parameters such as fiber diameter and spacing are consistently identified as important design variables. (Altlomate et al., 2016) and (Sangeetha, Subathra, Divahar, & Aravind Raj, 2022) report that increasing fiber diameter tends to increase transmitted light by enlarging the effective light-carrying area within the matrix, while larger spacing between fibers reduces overall transmittance due to the decrease in fiber density per unit area. These parameters are geometrically coupled through the fiber volume fraction, and their effects are therefore not independent within a given system. More recent studies by (Chiew et al., 2022; Shenoy, Nayak, Tantri, Shetty, & Shendkar, 2023) further confirm that changes in spacing and diameter (Bai et al., 2024) can lead to significant variations in light transmission, even under similar nominal fiber densities.

The spatial arrangement of optical fibers within the cementitious matrix constitutes an additional design variable that influences both optical performance and fabrication methodology (Arcolezi et al., 2026). Several distribution patterns are reported in the literature, as illustrated in Figure 1.5. The most common configuration in experimental studies is the regular grid arrangement, in which fibers are positioned at uniform intervals, enabling controlled variation of spacing and volume fraction (Arcolezi et al., 2026; Mei Chiew et al., 2022; Navabi, Amini, Rahmati, & Tahbaz, 2023; Su, Zhang, & Liu, 2023). Staggered layouts follow a similar principle while increasing packing density (Dinesh, Mercy, & Suji, 2019). Other configurations include random placement in the cross-sectional plane, where fibers remain parallel but lack positional regularity (Henriques et al., 2020), and fully random distribution for which the fibers' position differ between the input and output surfaces (Arcolezi, Marion, et al., 2025). In parallel systems, each fiber runs straight through the element and exits at the same position on the opposite face where it entered, preserving point-to-point spatial correspondence between faces. In randomly distributed systems, fibers are not constrained to a straight path between corresponding points, and each fiber exits at a position on the receiving face that is independent of its entry point (Ambali, Lolo, Handyaningtyas, Tasik, & Goran, 2023; Arcolezi, Marion, et al., 2025). At the macroscopic scale, this distinction affects the optical outcome: parallel composites may achieve translucency, transmitting spatial information, whereas randomly distributed composites are inherently light transmitting, while spatial information is not preserved, although it may be reconstructed computationally when fiber mapping is known (Ambali et al., 2023; Arcolezi, Marion, et al., 2025). Bundled arrangements, in which fibers are grouped into localized clusters, are also reported and can produce non-uniform light output across the specimen surface (Tahwia et al., 2022; Tahwia, Abdel-Raheem, Abdel-Aziz, & Amin, 2021). These configurations are primarily used in controlled studies to investigate geometric effects, while practical applications may adopt less constrained layouts depending on fabrication and design requirements.

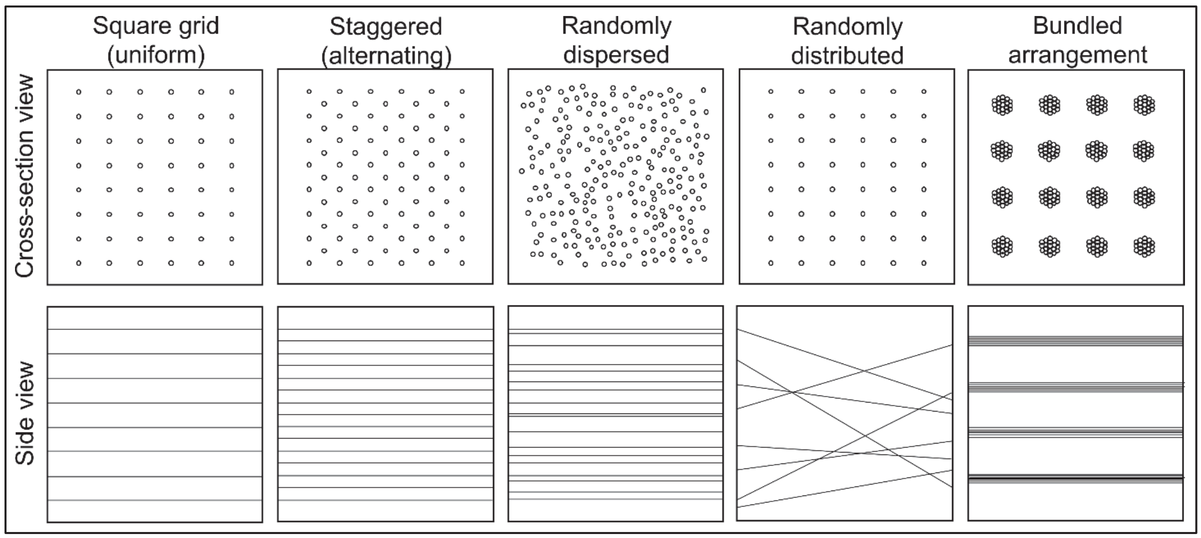

Figure 1.5 Schematic representation of optical fiber distribution patterns in LTCC cross-sections. Fiber diameter, distribution pattern, volume ratio, and spacing can vary

1.3.1.1 Fiber surface condition and treatment

The interaction between optical fibers and the cementitious matrix is influenced by the surface characteristics of the fibers. PMMA fibers present smooth and hydrophobic surfaces, which generally limit adhesion at the fiber-matrix interface (Cui et al., 2025; Drechsler et al., 2019). As a result, different surface modification and post-processing strategies have been investigated to adjust interfacial behavior and optical performance.

One approach involves the use of chemical treatments. Li, Li, & Guo, (2015) applied silane coupling agents to PMMA fibers to modify surface chemistry and potentially improve interaction with the surrounding matrix. This treatment is associated with increased surface roughness and may contribute to changes in interfacial bonding behavior. However, Chiew et al., (2020) report that the effectiveness of silane treatment is not consistent across all systems, suggesting that its influence depends on factors such as matrix composition and curing conditions.

In addition to chemical modification, mechanical aspects related to fiber surface condition are also relevant. The quality of the fiber end faces has a direct influence on light transmission. Studies by Henriques et al., (2018) and Huang et al., (2022) indicate that irregular or poorly cut surfaces promote light scattering, reducing the intensity of transmitted light. For this reason, post-processing procedures such as polishing or grinding of the specimen surfaces are commonly applied after curing to ensure that fibers are properly exposed and aligned with the surface (Navabi et al., 2023).

Surface protection strategies have also been reported. The application of epoxy coatings at the specimen surface can improve resistance to environmental exposure and reduce permeability at the fiber exit region (Pilipenko, Bazhenova, Kryukova, & Khapov, 2018; Saleem, Elshami, & Najjar, 2017). While this approach is not directly related to interfacial bonding within the bulk material, it contributes to the preservation of optical performance over time by protecting the exposed fiber ends. Overall, fiber surface condition affects both interfacial characteristics and optical transmission, although these effects are not always evaluated independently in the literature. As a result, the role of surface treatment in LTCC performance remains highly dependent on the specific combination of materials and fabrication procedures adopted in each study.

1.3.2 Cementitious matrix

The cementitious matrix provides structural continuity and defines the embedding environment for the optical fibers. In LTCC systems, mortar-based mixtures are more commonly adopted than conventional concrete due to their improved workability and finer aggregate structure, which facilitates fiber placement and reduces mechanical interference during casting. Self-compacting mortar and cement paste systems are frequently reported, particularly in laboratory-scale studies, as they allow the material to flow around closely spaced fibers and ensure more uniform embedding conditions (Tahwia et al., 2021).

The selection of aggregate size is a critical geometric constraint in these systems. The maximum aggregate size is typically limited to values below the characteristic spacing between fibers, in order to avoid obstruction during casting and to reduce the risk of fiber displacement or damage. When this condition is not satisfied, local heterogeneities may develop around fiber regions, affecting both internal uniformity and the continuity of the optical paths (Al-Sodani, 2025; Bai et al., 2024; Chiadighikaobi et al., 2023; Chiew, Ibrahim, Mohd Ariffin, et al., 2020; Han et al., 2017; Said, 2020).

Beyond granular composition, the type of binder influences both durability and fiber compatibility. Ordinary Portland cement systems are widely used; however, their relatively high alkalinity has been associated with potential degradation risks, especially in glass fiber-based configurations. In this context, Li, Li, & Guo, (2015) propose sulfoaluminate cement as an alternative due to its lower pH environment and rapid early strength development, which can be advantageous in applications requiring early demolding or handling.

Supplementary cementitious materials are frequently incorporated to modify pore structure and interfacial characteristics. Silica fume is commonly reported by Henriques et al., (2020) and Navabi et al., (2021) as a means of refining the matrix microstructure and improving the region surrounding the fiber surfaces. This densification of the matrix can reduce microvoid formation and contribute to a more stable embedding environment for the optical fibers. Fly ash and slag have also been investigated, particularly in studies such as Pagliolico et al., (2015); Spiesz, Rouvas, & Brouwers, (2016), where their use is associated with improved durability and mitigation of alkali-silica reaction in systems that incorporate waste glass, and glass fibers (fillers).

At the microstructural level, observations reported by Henriques et al., (2018) indicate the presence of interfacial voids and discontinuities at the fiber-matrix boundary. These features are frequently observed in PMMA and glass optical fiber systems and are associated with reduced compressive strength relative to conventional cementitious materials without embedded optical elements. The formation of these voids is influenced by both mixture rheology and fiber placement conditions, suggesting that matrix design and fabrication process are closely coupled in determining interfacial quality.

A recurring theme across studies is that matrix modifications can influence mechanical behavior and fiber-matrix interaction, although the relationship between these effects is not always consistent. Mixtures with higher flowability are often associated with improved fiber embedding and reduced local defects, while potential changes in the hardened pore structure may affect mechanical response depending on the specific system (Navabi et al., 2021). Conversely, denser matrices may improve compressive strength (Golewski, 2023) but can also make fiber placement more sensitive to processing conditions, particularly in systems with high fiber content or complex spatial arrangements.

The cementitious matrix in LTCC functions as both a load-bearing phase and a medium that influences the conditions of optical embedding, where small variations in composition can simultaneously affect mechanical response, internal continuity, and fiber-matrix interaction. These observations indicate that matrix effects in LTCC systems are better understood in conjunction with processing conditions and fiber configuration, instead of being treated as isolated material properties.

1.3.3 Fiber-matrix interface

As discussed in Section 1.3.1.1, the surface characteristics of optical fibers influence the development of the fiber-matrix interface in LTCC, which influences both the mechanical and optical performance of the composite. Unlike conventional fiber-reinforced cementitious composites, where interfacial bonding is intended to maximize stress transfer (Chang et al., 2025), this interface in LTCC must satisfy two functional requirements: mechanical continuity to limit premature crack initiation, and optical continuity to reduce light scattering and coupling losses at the fiber entry and exit faces (Antony Samy, Ayyanar, Ganesan, Singamuthu, & Veeriah, 2025). These requirements are not always compatible, and their relative importance depends on the intended application and material configuration.

From a mechanical standpoint, the interfacial transition zone (ITZ) in LTCC is particularly sensitive to the surface characteristics of the optical fibers. PMMA fibers with smooth and hydrophobic surfaces that limit adhesion to the surrounding cementitious matrix, can lead to the formation of interfacial gaps during hydration and hardening (Chiew et al., 2021). This effect reduces the effective load-bearing area and facilitate microcrack initiation under loading, contributing to the reductions in compressive and flexural strength reported in the literature (Ashraf & Rucka, 2023; Meng, Ying, Yu, & Hong, 2022). The extent of this effect varies with matrix composition. In denser matrices with low water-to-binder ratios, the porosity increase caused by fiber incorporation is smaller, whereas in more porous systems interfacial defects become more pronounced and their influence on mechanical response increases (Yue Li, Li, Wan, et al., 2015; Navabi et al., 2021).

The formation of the ITZ is also influenced by matrix rheology during casting (Kenny & Katz, 2015). In self-compacting and highly fluid mixtures, the matrix can flow more effectively around closely spaced fibers, thus mitigating incomplete encapsulation and void formation (Chiew, Ibrahim, Mohd Ariffin, et al., 2020; Tahwia et al., 2021). In stiffer mixtures, limited flow around fiber surfaces can produce larger interfacial discontinuities and higher local porosity (Akeed et al., 2022; Navabi et al., 2021). This interaction between rheology, interfacial quality, and mechanical performance shows that matrix design and fabrication conditions cannot be considered separately in LTCC systems.

From an optical standpoint, the interface mainly affects light transmission at the fiber end faces rather than along the fiber length. Since light propagates through total internal reflection at the core-cladding boundary, the surrounding cementitious matrix does not affect light guidance. However, the condition of the interface at the specimen surfaces where light enters and exits the embedded fibers, determined by cutting and polishing after curing, influences the efficiency of light coupling into and out of the fibers. Irregular or poorly finished surfaces increase scattering at the entry and exit points, reducing transmitted intensity (Henriques et al., 2018; Yue Li, Li, Wan, et al., 2015). Grinding and polishing are therefore commonly used to ensure that fiber ends remain exposed, flush with the surface, and free of residual matrix that could obstruct the optical path (Navabi et al., 2021).

In summary, the fiber-matrix interface acts simultaneously as a mechanical discontinuity and an optical boundary, so modifications that improve one subsystem can reduce the other. Fiber surface treatments that increase roughness may improve mechanical bonding at the fiber-matrix interface but can also affect the quality of the fiber end faces, increasing scattering losses at the light entry and exit points. This trade-off has not been systematically quantified in the LTCC literature, which limits the ability to define unified design rules for simultaneous optimization of mechanical and optical performance.

1.4 Casting and fabrication methodologies

The fabrication of LTCC requires careful control of fiber placement, as the spatial distribution of optical elements influences both light transmission and mechanical performance (Altlomate et al., 2016; Arcolezi et al., 2026; Bai et al., 2024; Chiew, Ibrahim, Mohd Ariffin, et al., 2020). The methods reported in the literature can be broadly classified according to the stage at which fibers are introduced relative to matrix casting. Bai et al., (2024) categorized fabrication procedures into two main groups, depending on whether the fibers are incorporated before or after casting. Beyond this procedural distinction, fabrication methods also influence the reproducibility of fiber distribution and the formation of local defects, which contribute to variability in both optical and mechanical performance.

Among the approaches in which fibers are introduced prior to casting, the most common methods include perforated formwork, in which molds are prepared with predefined holes to guide and position the fibers; textile-based insertion, where optical fibers are integrated into a mesh or fabric structure that is subsequently placed within the mold before the cementitious material is introduced; and extrusion-based 3D printing, a more recent and emerging technique in which fibers are incorporated during the layer-by-layer deposition of the cementitious material. These approaches are illustrated in Figure 1.6.

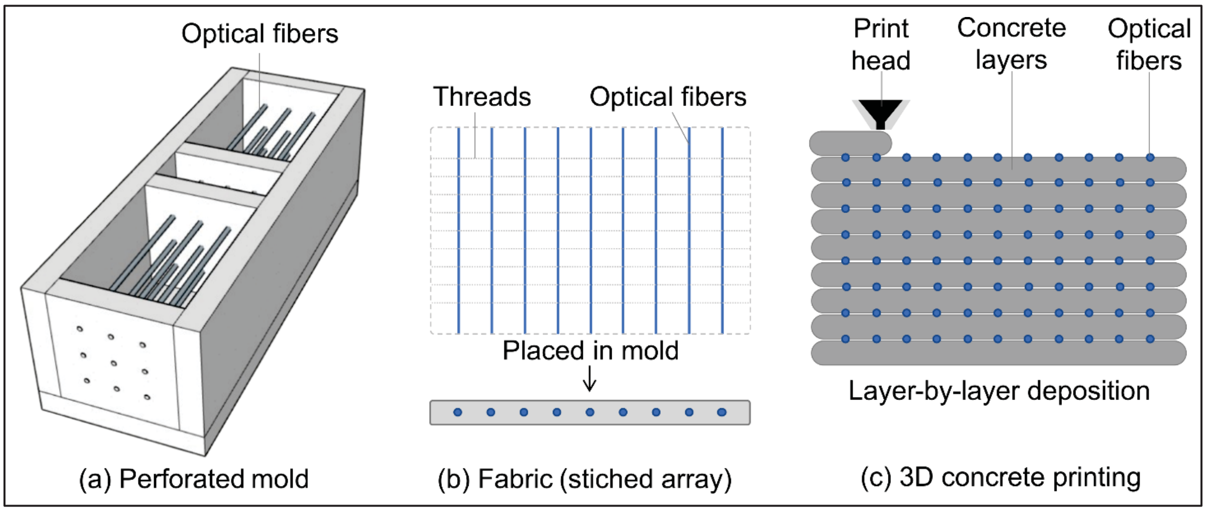

Figure 1.6 Representative fabrication methods for fiber-optic LTCC: (a) perforated formwork with pre-positioned fibers; (b) textile-based fiber insertion for layered placement; (c) extrusion-based 3D printing with controlled fiber integration

LTCC offers considerable versatility across both structural and non-structural applications. Owing to its visual and architectural appeal, it is frequently used in non-structural applications, including artistic and design-oriented projects (Chiew, Ibrahim, Mohd Ariffin, et al., 2020). In these contexts, fabrication priorities may differ, and the level and nature of control over fiber placement depend on the intended outcome. While scientific studies emphasize controlled and repeatable procedures to enable systematic evaluation, other applications prioritize visual effect, patterning or architectural integration. Consequently, fabrication approaches should be understood as application-dependent rather than as uniformly defined across all LTCC applications.

The most widely adopted strategy in literature is pre-insertion, in which fibers are positioned within the mold prior to casting. Perforated formwork represents the most common implementation of this method (Altlomate et al., 2016; Nam et al., 2025; Navabi et al., 2021;

Tahwia et al., 2021). In this way, fibers of predefined length are threaded through perforated molds, using the drilled plates as positioning guides based on the target fiber content and diameter. This approach allows controlled alignment and spacing of fibers during casting. However, the degree of positional control varies across studies, ranging from regularly spaced perforations designed to promote uniform fiber distribution to configurations where fiber placement is introduced with limited positional constraint. As shown in Figure 1.6a, the method remains labor-intensive, particularly at higher fiber densities, due to the need for individual fiber placement (Al-Sodani, 2025; Bai et al., 2024; Chiadighikaobi et al., 2023; Chiew, Ibrahim, Mohd Ariffin, et al., 2020).

As an alternative approach, Li, Li, Wan, et al., (2015) and Roye et al., (2009) proposed integrating optical fibers into textile structures. In this method, fibers are arranged unidirectionally and fixed at their ends using threads, forming a fabric that can be placed into the mold in layers. This method, illustrated in Figure 1.6b, improves placement efficiency and promotes regular spacing, although it introduces constraints related to fiber alignment stability and handling and during casting.

A more recent alternative is extrusion-based 3D printing, in which the cementitious material is deposited around pre-positioned fibers. Lyu et al., (2024) investigated this approach and reported that compressive strength decreases when loading is applied parallel to the fiber alignment, while higher values are observed under perpendicular loading. This directional dependence indicates that fiber orientation introduced during fabrication can lead to anisotropic mechanical response. Mbabazi et al., (2026) reported improved buildability using printed cellular geometries (hollow internal structure in the printed layer), which enhanced structural stability while maintaining reduced thermal conductivity and allowing significant light transmission in the composite. As shown in Figure 1.6c, this method also allows geometric control compared to formwork-based techniques but requires careful adjustment of mixture rheology to ensure printability and adequate fiber-matrix interaction.

Additional fabrication strategies are also reported. In the post-insertion method, fibers are introduced into pre-drilled holes after matrix hardening. Post-insertion methods provide high positional accuracy but modify the fiber-matrix interface, which can influence both mechanical continuity and optical coupling. As a result, these approaches shift the source of variability from placement control to interfacial behavior (Bai et al., 2024). A related variant involves casting with conventional molds followed by cutting or surface finishing of the hardened material to expose fiber ends and enable light transmission. This approach simplifies fabrication but provides limited control over fiber distribution within the bulk material (Henriques et al., 2020). For resin-based systems, Juan & Zhi, (2019) produced prefabricated light guides inserted prior to casting, while Pilipenko et al., (2018) created voids later filled with resin. These approaches enable geometric flexibility but introduce material compatibility considerations.

Across the reported methods, maintaining fiber position during casting remains a practical concern, and its effectiveness depends on a combination of mixture rheology, fiber arrangement, and processing conditions. In more fluid systems, the matrix can more easily flow around and between closely spaced fibers, improving mold filling and reducing local defects. In mixtures with low workability, flow may be insufficient to fully surround dense fiber arrangements, increasing the risk of voids or incomplete filling (Navabi et al., 2021). External compaction can further modify these conditions by promoting matrix rearrangement and affecting internal fiber positioning (Arcolezi, Marion, et al., 2025). More broadly, fabrication methodology acts as a source of variability in LTCC systems rather than only a processing step. Differences in rheology, placement stability, and compaction conditions influence fiber distribution, interfacial quality, and defect formation, which are reflected in both optical and mechanical performance. This perspective is important when comparing results across studies, as differences in fabrication can produce variations in performance that are independent of material composition.

1.5 Optical performance

In fiber-optic LTCC, light transmission defines how much light can pass through an opaque structural element. In these composites, light is guided through the cementitious matrix by embedded optical fibers, whose transparent cores act as discrete pathways between the two faces of the material (Kasap, 2018). From a physical standpoint, optical performance in LTCC systems is influenced by two coupled components: the overall light transmittance of the fiber network and the efficiency of light coupling into and out of the fibers. Optical performance in fiber-optic LTCCs is determined by how efficiently light is guided through the embedded fiber network across the thickness of the element. The measured transmittance depends on both specimen-related parameters, such as fiber surface density, diameter, spacing, and sample thickness (Henriques et al., 2018; Huynh Phuong Nam et al., 2022; Yue Li, Li, Wan, et al., 2015; Mei Chiew et al., 2022), and experimental conditions, including source and detector distances, angle of incidence, and measurement environment (Huynh Phuong Nam et al., 2022; Yue Li, Li, & Guo, 2015; Sharifi et al., 2023 Tahwia et al., 2022). These two groups of parameters are not independent in reported results, as experimental configurations influence how intrinsic material properties are observed and quantified.

For clarity, these parameters can be grouped into two categories: intrinsic parameters, which define the maximum transmittance of the composite, and set-up-dependent parameters, which determine the actual transmittance measured in a given experiment. The distinction between specimen-intrinsic and setup-dependent parameters is relevant for the interpretation of results across studies. Reported optical responses may reflect differences in composite design as well as variations in the light source, detector, measurement geometry, and calculation procedure. Figure 1.7 illustrates these parameters and the optical characterization arrangement most commonly reported in the literature.

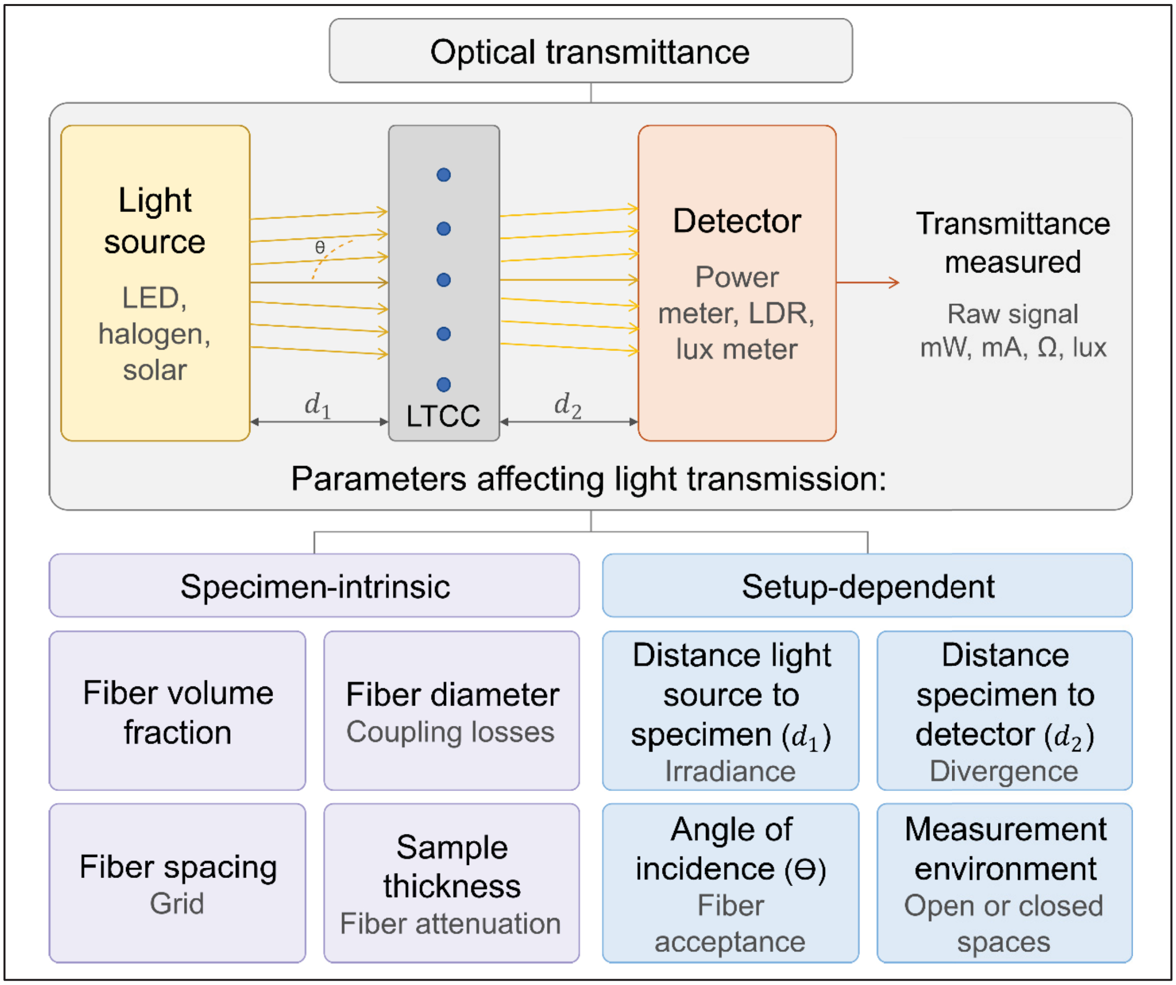

Figure 1.7 Schematic representation of the optical transmittance measurement configuration and classification of parameters that may influence the reported optical response of fiber-optic LTCCs

Optical transmittance is a central component of LTCC performance characterization; however, no standardized test protocol currently exists for measuring it. Experimental configurations vary substantially across the literature in terms of test environment, instrumentation, and reported quantity (Bai et al., 2024; Chiew, Ibrahim, Mohd Ariffin, et al., 2020; Henriques et al., 2018). This variability limits direct comparison between studies. Part of the variation in reported values is therefore associated with differences in measurement conditions, in addition to intrinsic material behavior. Measurements have been conducted in both open spaces and enclosed dark chambers. The latter approach (Altlomate et al., 2016; Chiew, Ibrahim, Mohd Ariffin, et al., 2020; Henriques et al., 2018; Huang & Lu, 2020; Rong et al., 2023) isolates the specimen from ambient light and ensures controlled incidence conditions, improving reproducibility. Open-space configurations (Nam et al., 2025, 2024), in contrast, introduce uncontrolled ambient light contributions that can inflate apparent transmittance values. To mitigate this, the authors (Nam et al., 2025, 2024) employ a lens-based setup in which a first lens focuses the light source onto the specimen face, and a second lens collects and directs the transmitted light toward the detector.

Beyond the test environment, the instrumentation used to quantify transmitted light further complicates inter-study comparison. Four main types appear in the literature: optical power meters (mW) (Arcolezi et al., 2026), luxmeters (lux) (Delnavaz, Najari, Hashemian, & Amiri, 2026; Henriques et al., 2020; Mbabazi, Luo, Du, Wang, & Lyu, 2026; Momin et al., 2014), LDR-based resistance circuits (Ω or mA) (Dadavali & Reddy, 2025; Huong & Kassim, 2019; Mahto & Kujure, 2017; Palanisamy et al., 2022; Tahwia et al., 2021; Tuaum et al., 2018), and spectral or imaging detectors such as spectrometers and CCD cameras (Yue Li, Li, & Guo, 2015; Nam et al., 2025). Because these produce outputs in incompatible units, raw transmitted signals cannot be directly compared across studies. To address this, Chiew, Ibrahim, Mohd Ariffin, et al., (2020) recommend expressing light transmission as an efficiency in percentage, based on the ratio between transmitted and incident signals measured under the same conditions. This formulation reduces the influence of source intensity and measurement setup, and has been adopted or discussed by several authors (Arcolezi et al., 2026; Yue Li, Li, & Guo, 2015; Mainini, Poli, Zinzi, & Cangiano, 2012; Mei Chiew et al., 2022; Spiesz et al., 2016; Tuaum et al., 2018). However, even when normalized metrics are used, the influence of measurement configuration is not fully removed, as detector positioning, alignment, and capture geometry continue to affect the recorded signal. A significant portion of the literature still reports only absolute transmitted signals, which remain strongly dependent on the specific experimental configuration and limit cross-study comparison.

Adopting transmittance as a percentage addresses part of this variability but does not remove the physical limits imposed by the specimen. The cementitious matrix is opaque and does not contribute to light transmission, so the maximum transmittance is controlled by the fiber array.

The fiber transmission, defined as the fraction of light that propagates through a fiber over a given length, can be estimated from the attenuation coefficient (Kasap, 2018). For typical PMMA fibers, attenuation at visible wavelengths is low, and transmission remains close to unity. Under these conditions, losses within the fiber are small compared to those at the entrance and exit faces. Based on this, Arcolezi et al., (2026) proposed estimating the theoretical maximum transmittance from the geometric fraction of fiber cores within the specimen cross-section. This value represents an upper bound defined by the available light-transmitting area, independent of measurement setup. In practical terms, this maximum value corresponds to the total area of all fiber cores, multiplied by their transmission efficiency, and divided by the total cross-sectional area of the specimen. This reference helps separate the transmittance of the LTCC sample from losses introduced by fabrication and measurement conditions. Measured values close to this upper bound indicate that most of the incident light is effectively coupled into the fibers and transmitted through the specimen. Measured values close to this limit indicate efficient coupling and transmission, while lower values reflect additional losses associated with surface condition, misalignment, or measurement configuration.

The influence of the main variables reported in the literature can be grouped into specimen intrinsic parameters and measurement set-up conditions. Figure 1.8 summarizes the qualitative trends most frequently observed for these variables based on data compiled from multiple reviewed studies rather than specific experimental datasets.

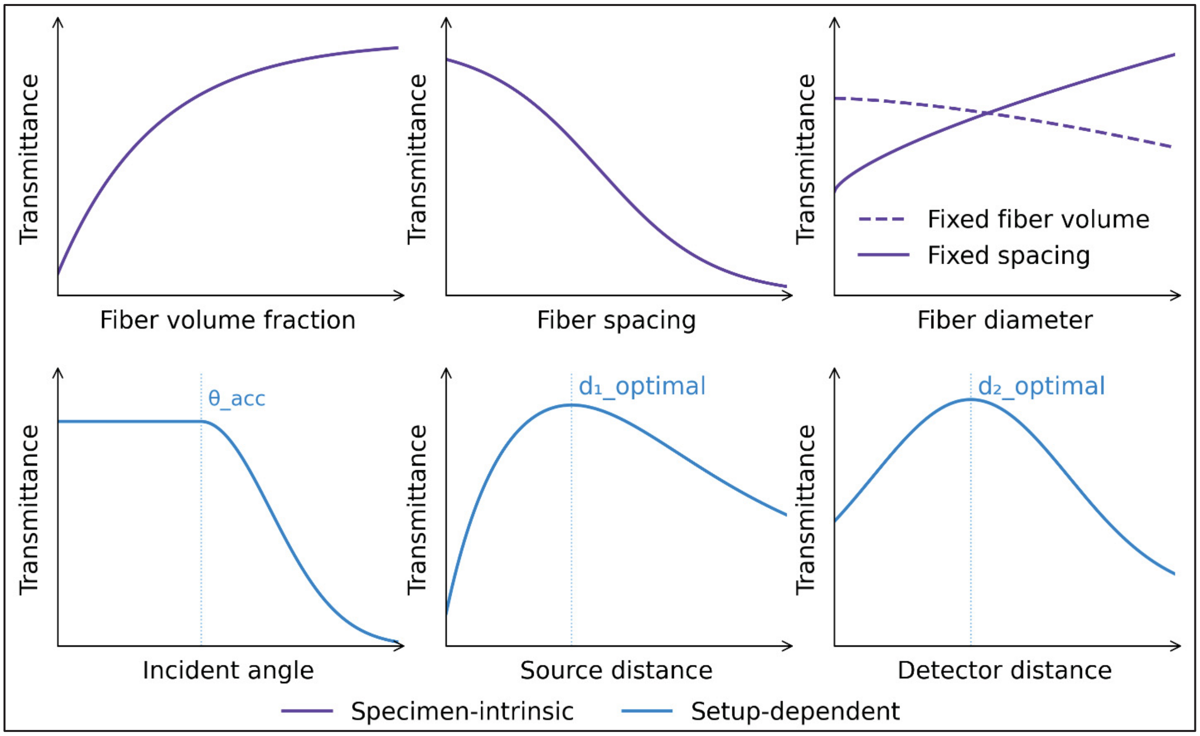

Figure 1.8 Qualitative trends of optical transmittance in fiber optic light transmitting cementitious composites as a function of specimen intrinsic parameters and measurement setup conditions

Among the specimen-intrinsic parameters (Figure 1.7), fiber volume fraction is consistently associated with higher transmittance because a larger proportion of the cross-section becomes available for light conduction. In contrast, increasing fiber spacing reduces the number of light transmission paths per unit area and therefore lowers the transmitted signal. The influence of fiber diameter is more complex because its effect depends on the geometric constraint imposed during specimen design. Under constant fiber spacing, larger diameters increase the transmissive area and tend to increase transmittance, whereas under constant fiber volume fraction, the same increase reduces the number of fibers and may lower the measured signal (Al-Sodani, 2025; Bai et al., 2024).

Among the setup-dependent variables (Figure 1.7), the angle of incidence affects the efficiency of light coupling into the fibers. Transmittance remains relatively stable while the incident angle remains within the fiber acceptance cone, followed by a rapid decrease once the acceptance limit is exceeded. The distance between the artificial point like light source and the specimen also influences the measured signal because insufficient beam expansion at very short distances and irradiance losses at larger distances can both reduce coupling efficiency, leading to an intermediate optimum source position. Similarly, the distance between the specimen and the single photodetector determines how much of the emerging light cone is captured by the sensor, producing a characteristic optimum detector position beyond which the measured transmittance decreases (Arcolezi et al., 2026; Huynh Phuong Nam et al., 2022; Yue Li, Li, & Guo, 2015; Mei Chiew et al., 2022; Rong et al., 2023; Tahwia et al., 2021; Tuaum et al., 2018).

Available experimental results are consistent with this geometric behavior. Studies with larger specimens tend to report peak transmittance values at greater detector distances, while smaller specimens reach maximum readings closer to the output surface. In some instances, measurements are conducted at distances beyond the expected optimum, which leads to systematic underestimation of transmittance. At very short distances, detector saturation or non-uniform light distribution may also affect the measurements. In addition, the use of single-point sensors can introduce local bias, depending on fiber distribution across the specimen surface (Arcolezi et al., 2026).

Taken together, these observations indicate that a significant part of the variability in reported transmittance values is associated with measurement configuration, particularly detector positioning, rather than intrinsic specimen properties. As a result, reported transmittance values reflect a combined effect of material design and experimental conditions, which should be considered when comparing results across studies. More generally, although transmittance is widely investigated in LTCC, the associated methodologies are not consistent. The lack of a standardized procedure results in data that combine material response and measurement conditions, which limits direct comparison between studies.

To improve consistency, future work should report key experimental parameters, including fiber numerical aperture, specimen dimensions, source and detector distances, angle of incidence, surface condition of fiber ends, and the method used to calculate transmittance. More consistent reporting and controlled measurement configurations would support clearer identification of material-related trends, particularly with respect to fiber volume fraction and geometric parameters.

1.6 Mechanical performance

Optical fiber incorporation modifies the internal structure of cementitious composites by introducing discrete inclusions within a continuous matrix. Unlike conventional fiber reinforcement, where the primary objective is mechanical enhancement via fillers, optical fibers are primarily introduced to enable light transmission, and their contribution to load-bearing capacity is secondary. As a result, mechanical performance reflects the combined influence of fiber geometry, distribution, volume fraction, and fiber-matrix interaction, rather than fiber addition alone.

1.6.1 Compressive strength

Given the variability in reported test conditions and material compositions across studies, direct comparison of compressive strength results is not straightforward. Compressive strength is the most frequently reported mechanical property in LTCCs, yet the available results span a wide range of behaviors and configurations, which makes finding any single trend difficult.

To enable comparison, the results can be reported in normalized form (Al-Sodani, 2025; Bai et al., 2024; Chiew, Ibrahim, Mohd Ariffin, et al., 2020). In this approach, the strength of a fiber-reinforced specimen is divided by the strength of a corresponding fiber-free control mixture from the same study, such that the reported value represents a relative change induced by fiber incorporation. This approach reduces part of the variability associated with mix design and testing conditions, but does not fully isolate the effect of fiber incorporation. This procedure is intended to reduce the influence of differences in mix design and testing conditions and to improve comparability between studies. However, the reference mixture itself varies across studies, which limits direct comparison between normalized values.

This normalization relies on the implicit assumption that the cementitious matrix is a fixed and well-defined baseline, as typically assumed in conventional fiber-reinforced concrete. In LTCCs, this assumption does not hold, since both matrix composition and testing procedures vary substantially across the literature. As a result, normalized values reflect differences between two systems within the same study, but do not necessarily provide a consistent basis for comparison across studies. Differences in mix design, curing conditions, and testing procedures remain embedded in the reported ratios, which contribute to the dispersion observed in the literature.

It highlights that compressive strength does not depend only on fiber content, but also on the fiber-matrix system, in which the matrix contributes to the overall mechanical response. The magnitude of this effect depends on the baseline porosity and stiffness of the matrix. In this context, the effect of fiber incorporation better understood as a perturbation of the matrix system, whose magnitude depends on the sensitivity of the matrix to interfacial defects (Mbabazi, Luo, et al., 2026). In more porous mortars, fibers introduce pronounced local defects, whereas in denser systems such as ultra-high-performance concrete, the relative porosity is small, but the material becomes more sensitive to localized damage (Henriques et al., 2018; Navabi et al., 2021). In self-compacting matrices, improved rheology may enhance fiber encapsulation and reduce void formation (Tahwia et al., 2021). Consequently, different matrix systems can produce different normalized compressive strengths for the same fiber content. This is consistent with the broad dispersion observed in normalized datasets, as illustrated in Figure 1.9.

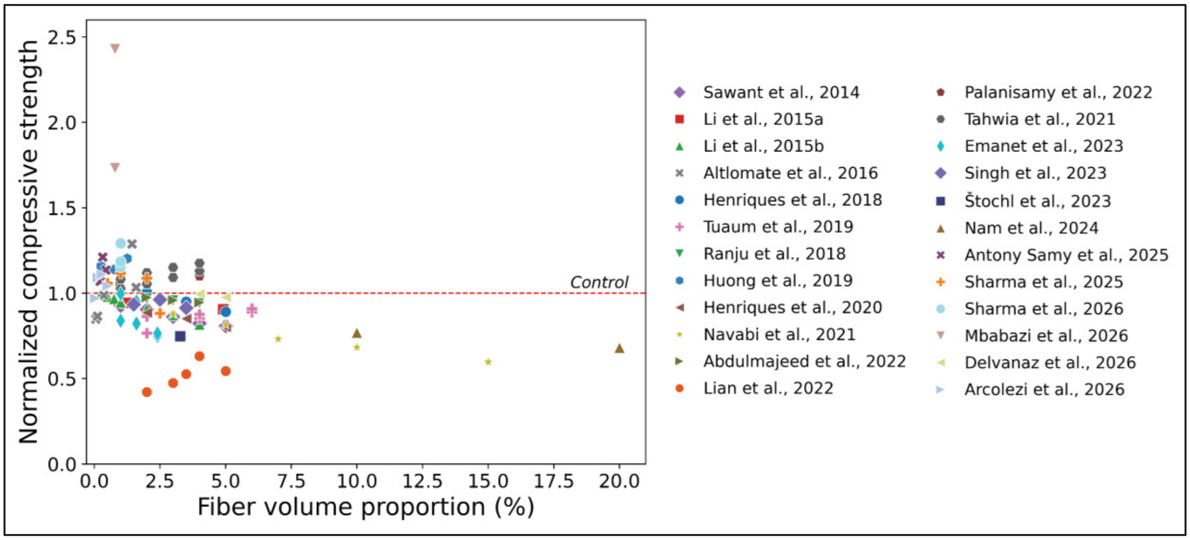

Figure 1.9 Normalized compressive strength of LTCCs according to the increase in fiber volume fraction

Among the studies examined, matrix compositions range from conventional M30 Portland cement concrete at w/c = 0.42 (Sawant, Jugdar, & Sawant, 2014) to ultra-high-performance systems with w/c = 0.28, silica fume, quartz powder, and superplasticizer (Navabi et al., 2021). Intermediate cases include sulfoaluminate cement mortars with blast furnace slag (Yue Li, Li, & Guo, 2015), high-strength white cement systems with limited mix details (Štochl, Vychytil, & Hájek, 2023), and self-compacting concretes incorporating supplementary cementitious materials at w/b = 0.27 (Nam et al., 2024; Tahwia et al., 2021). In several studies, the mix design information is not reported. These differences correspond to fundamentally distinct material systems with varying pore structures, hydration products, and interfacial properties. Additional variability arises from curing conditions, which can influence matrix development and ITZ formation (Yue Li, Li, & Guo, 2015). As a result, the normalized compressive strength ratio should be interpreted with some caveats, as differences in matrix composition and testing conditions between studies may influence the normalized values.

The predominant trend in literature is a reduction in normalized compressive strength with increasing fiber content, reported across multiple studies (Sawant et al., 2014; Henriques et al., 2018; Yue Li, Li, & Guo, 2015; Yue Li, Li, Wan, et al., 2015; Navabi et al., 2021; Tuaum et al., 2019). This behavior is generally attributed to the smooth, hydrophobic surface of PMMA fibers, which weakens interfacial bonding, promotes microcrack initiation, and reduces effective load-bearing area. At 5% fiber content, normalized values of 0.80-0.89 are typical in mortar systems, decreasing to around 0.60 in UHPC (Navabi et al., 2021) and 0.42 in lightweight concretes (Lian & Yin, 2022), where additional matrix porosity intensifies interfacial damage.

However, several studies report neutral or positive trends. In self-compacting matrices, (Tahwia et al., 2021) observe increases in normalized compressive strength from 1.03 to 1.18 with fiber content, while (Huong & Kassim, 2019) reports values up to 1.20 at low fiber fractions. Sharma, Devi, & Saini, (2025) and Antony Samy et al., (2025) report gains up to 12% and 21%, and Altlomate et al., (2016) reports a value of 1.29 at low content. These deviations are often interpreted through mechanisms such as fiber spacing effects or matrix densification, although their evaluation is limited by insufficient matrix characterization in most studies. These variations indicate that the direction and magnitude of strength change depend on the interaction between fiber content and matrix properties, rather than on fiber content alone.

A more cautious interpretation is that the effect of fiber content cannot be separated from the sensitivity of the surrounding matrix to interfacial defects. In low water/cement, SCM-rich systems, the denser matrix and narrower interfacial transition zone may partially mitigate fiber-induced porosity through crack arrest and microstructural refinement at moderate fiber contents. In contrast, higher w/c matrices exhibit weaker interfaces and higher inherent porosity, leading to a more pronounced degradation in mechanical performance even at relatively low fiber fractions. In high-strength systems such as UHPC, the reduced ability to redistribute localized stress concentrations may further amplify the impact of interfacial defects, resulting in a stronger decline with increasing fiber content (Al-Sodani, 2025; Bai et al., 2024; Chiew, Ibrahim, Mohd Ariffin, et al., 2020). They may explain why decreasing, neutral, and increasing trends can all appear in the current literature.

The influence of fiber diameter is similarly inconsistent. Some studies (Al-Sodani, 2025; Bashbash, Alqedra, Hajrus, & Wafi, 2013; Sangeetha et al., 2022) report strength increases with larger diameters, attributing this to higher stiffness under confinement. Others (Nam et al., 2024) report reductions due to an increased interfacial weak zone per unit volume. Both mechanisms are plausible, and their relative importance likely depends on matrix stiffness and porosity, which are not consistently characterized or controlled across studies. These results indicate that the variability in reported trends is strongly influenced by differences in matrix properties and experimental conditions across studies. As a result, isolating the effect of fiber parameters such as content or diameter remains challenging. More detailed reporting of matrix characteristics may help clarify these trends, but current comparisons remain largely context dependent.

1.6.2 Flexural strength

Flexural strength data for LTCCs show greater dispersion than compressive strength, with normalized values ranging from 0.68 to 1.55 at 28 days across the compiled studies (Figure 1.10). This wider range reflects the combined influence of matrix composition, fiber arrangement, and testing configuration. In contrast to compressive strength, flexural response is more sensitive to fiber orientation and local stress distribution, which increases variability between studies. In this context, fibers may contribute differently depending on their interaction with the surrounding matrix and their orientation with respect to the stress field, although these aspects are not consistently quantified in LTCC studies.

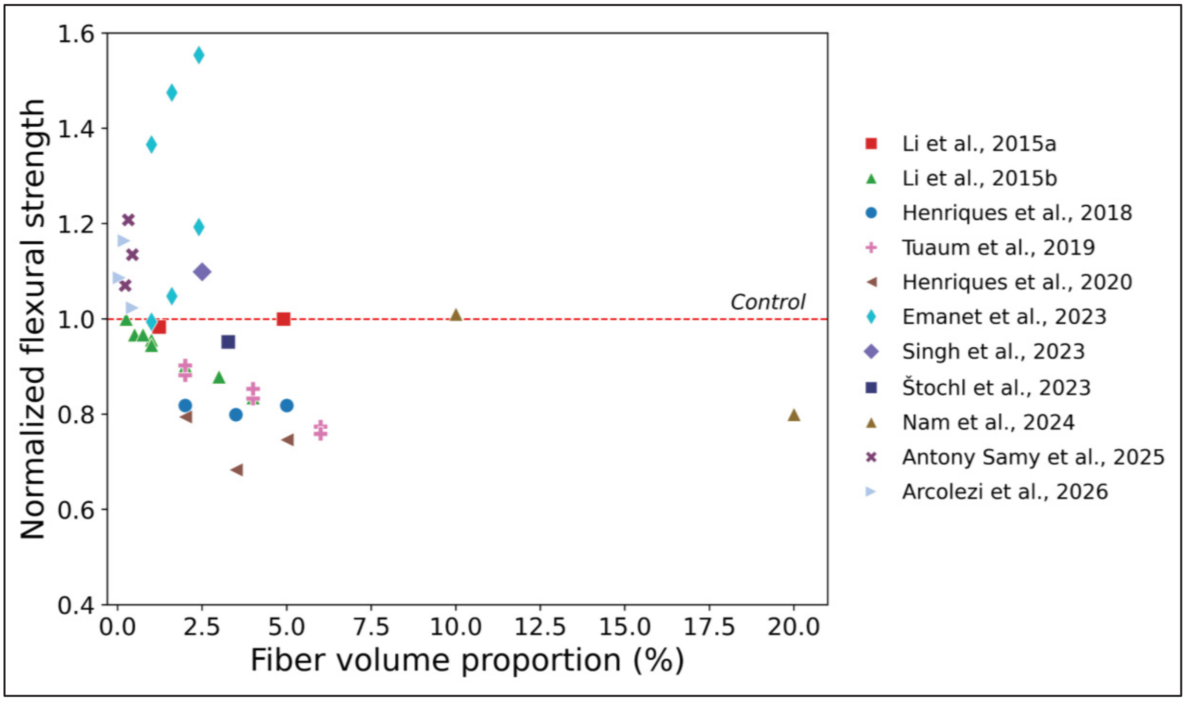

Figure 1.10 Normalized flexural strength of LTCCs according to the increasing in fiber volume fraction

The dominant trend is a reduction in normalized flexural strength with increasing fiber content, consistent with the compressive behavior and commonly associated with interfacial transition zone discontinuities. This pattern is reported across studies with different matrix systems and fiber proportions (Henriques et al., 2018, 2020; Yue Li, Li, & Guo, 2015; Yue Li, Li, Wan, et al., 2015; Nam et al., 2024; Tuaum et al., 2019). The reduction is generally progressive with fiber content, although deviations from monotonic behavior are observed. In (Henriques et al., 2020), for example, values of 0.79, 0.68, and 0.75 are reported at 2, 3.5, and 5 percent fiber content, respectively, suggesting that additional effects may influence the response at higher fiber proportions. Such behavior is not observed in (Henriques et al., 2018), indicating that differences in fiber distribution and local arrangement may contribute to variability in flexural response under otherwise comparable matrix conditions.

Some studies report increases in normalized flexural strength. Emanet & Arda Buyuktaskin, (2023) observe normalized flexural strengths of 1.37, 1.48, and 1.55 at 1, 1.6, and 2.4 percent fiber content, respectively, which are among the highest reported in the dataset. This behavior is often interpreted as a matrix-dependent response, particularly lower fracture resistance, which can alter the balance between matrix cracking and load transfer mechanisms at relatively low fiber contents. Antony Samy et al., (2025) and Singh, Bhatnagar, & Singh, (2023) also report moderate increases in flexural strength at low fiber contents, while small reductions in compressive strength are observed in the same mixtures, indicating that compressive and flexural responses may not vary in the same direction under identical material conditions.

Fiber orientation is an additional variable that may influence flexural performance in LTCCs, although it has not been systematically investigated in the context of this material. In fiber-reinforced cementitious composites more broadly, fibers oriented longitudinally along the beam span tend to produce better flexural results than transversally oriented fibers, as they are more favorably positioned relative to the tensile stress field developed during bending (Huynh Phuong Nam et al., 2022; Liu, Feng, Liu, Li, & Tang, 2023; Lyu et al., 2024). Whether this relationship holds consistently in LTCCs, where fiber arrangement is also constrained by light transmission requirements, remains an open question that requires further investigation.

Flexural performance in LTCCs therefore vary with the interaction between matrix properties, fiber arrangement, and testing methodology, rather than on fiber content alone. The variability observed across studies is therefore associated with differences in matrix composition, fiber configuration, and testing conditions, which are not consistently standardized in the current literature. As in optical characterization, part of the variability in reported mechanical properties is associated with differences in experimental procedures, which should be considered when comparing results across studies.

The compiled data supports the examination of general trends in normalized strength, but they do not provide a consistent basis for isolating the independent contributions of fiber diameter, spacing, matrix composition, and fabrication conditions. These parameters are not reported uniformly across the reviewed studies. Therefore, the figures are interpreted as an exploratory cross-study synthesis rather than as a formal meta-analysis.

A combined optical-mechanical synthesis is further limited by a difference between the two domains. Mechanical results can be normalized against a fiber-free control of the same study, comparing strength in MPa to strength in MPa. Optical results have no equivalent reference, as a fiber-free matrix transmits no light, and reported values span different physical quantities (lux, mW, Ω or mA, and %). The two domains therefore cannot be reliably paired study-by-study.

1.7 Durability and sustainability considerations

The durability of LTCC remains insufficiently documented, particularly in long-term environmental exposure. Although the degradation mechanisms affecting the cementitious matrix are similar to those observed in conventional materials, the presence of embedded optical fibers introduces microstructural features that may influence transport properties and long-term performance (Al-Sodani, 2025; Bai et al., 2024). Current knowledge is largely based on short-term mechanical and physical characterization, while long-term durability data remain limited. Experimental studies have focused primarily on mechanical characterization, while durability aspects such as freeze-thaw resistance, carbonation, and long-term environmental aging remain less explored (Emanet & Arda Buyuktaskin, 2023).

The durability response also depends on fiber type. PMMA fibers are generally stable in alkaline environments but may be sensitive to ultraviolet radiation and thermal exposure at exposed surfaces, which can affect optical performance over extended periods (Chiew, Ibrahim, Rus, Fadzir, & Abd Rabbi, 2025). In contrast, glass fibers are more susceptible to alkaline attack from the cementitious matrix, which may result in progressive degradation (Chen, Wang, Pan, Lawi, & Zhu, 2021). These differences indicate that durability in LTCC systems depends on the interaction between fiber properties and the surrounding matrix environment. The use of supplementary cementitious materials, such as fly ash or slag, has been discussed as a strategy to reduce matrix alkalinity and mitigate these effects, in line with observations reported by Spiesz et al., (2016), Chen et al., (2021) and Pagliolico et al., (2015).

From a thermal standpoint, the incorporation of optical fibers modifies heat transfer within the composite. Polymer optical fibers exhibit lower thermal conductivity (approximately 0.15-0.2 W/m·K) compared to typical cementitious materials, which can result in a reduction in overall thermal conductivity (Al-Sodani, 2025). The magnitude of this effect depends on fiber content, distribution, and matrix composition, and remains insufficiently quantified in the current literature.

In terms of energy performance, LTCC is frequently associated with passive daylighting applications. By transmitting natural light through building elements, the material can reduce the demand for artificial lighting. Reported energy savings vary depending on configuration, with some studies indicating significant reductions under favorable conditions (Ahuja & Mosalam, 2017; Delnavaz et al., 2026; Huang & Lu, 2020; Su et al., 2023). However, these estimates are often based on specific configurations and may not be directly transferable across different systems. At the same time, the transmission of solar radiation may influence thermal loads, indicating that performance should be evaluated at the building scale rather than at the material level alone.

Environmental and economic aspects remain relatively underexplored. The environmental impact of LTCC is largely governed by the cementitious matrix, with additional contributions from optical fibers, whose production is comparatively energy-intensive (Al-Sodani, 2025; Bai et al., 2024). Fiber content therefore directly influences both environmental footprint and cost and remains one of the main constraints for broader application. At present, life-cycle assessments specific to LTCC systems remain limited, which limits quantitative comparison with conventional cementitious materials.

Taken together, available studies indicate that durability in LTCC systems is influenced by the presence of fiber-induced discontinuities, the properties of the fiber material, and the surrounding matrix composition. However, the absence of long-term and standardized durability data limits the ability to assess how these factors interact under service conditions. As a result, current understanding remains largely qualitative, and further work is needed to establish consistent evaluation methods and to clarify the long-term performance of these materials.

1.8 Fiber-optic cementitious composite applications

Applications of fiber-optic LTCCs can be grouped into two main categories: architectural applications, which use the visual effect of light transmission through an opaque cementitious material, and functional applications, in which the embedded fiber network is used for sensing, energy harvesting, or environmental control. In some cases, both functions are combined within the same composite element. The feasibility of these applications depends on the balance between optical performance, mechanical requirements, and fabrication constraints discussed in previous sections.

Translucent cladding panels represent the most widely reported use of these materials. In this configuration, LTCC panels are installed as non-structural or semi-structural façade elements that transmit daylight from the exterior to interior spaces while maintaining an opaque appearance from the outside. The visual effect, in which the silhouettes of external objects or changes in daylight intensity remain visible through the panel surface, has been used for both daylighting and architectural design (Al-Sodani, 2025; Bai et al., 2024; Chiew, Ibrahim, Mohd Ariffin, et al., 2020). Commercial systems, including LiTraCon in Hungary (LitraCon®*, 2026*) and Lucem Luccon in Germany (LUCEM Luccon®, 2026), have been installed in office buildings, public spaces, and exhibition environments across Europe and Asia, demonstrating the technical viability of this application at full scale. These applications are typically non-load-bearing, which reduces the impact of the mechanical limitations associated with fiber incorporation.

Interior partitioning is a related use, where LTCC panels are applied as dividing walls, countertops, or decorative surfaces. Their ability to transmit artificial light from one side of the element to the other creates lighting effects without transparent glazing (Al-Sodani, 2025; Bai et al., 2024; Chiew, Ibrahim, Mohd Ariffin, et al., 2020). In these applications, optical performance and visual output are prioritized, while mechanical demands remain moderate. In this context, structural demands are limited, and the main design parameter becomes the optical output, including the uniformity of light distribution and the transmitted pattern produced by different fiber arrangements.

Street furniture, decorative paving elements, and public art installations form another group of architectural uses in which LTCC is used mainly for its visual properties (Al-Sodani, 2025; Bai et al., 2024; Luhar et al., 2021). These applications impose lower structural demands, but require attention to surface durability, UV stability of exposed fiber ends, and resistance to mechanical wear. Surface condition and environmental exposure become relevant in these cases, as they influence the long-term preservation of optical performance.

Functional applications extend the use of the fiber network beyond passive light transmission. The integration of LTCC with photovoltaic systems has been investigated as a way to combine structural function, daylight transmission, and energy generation within a single facade element (Yan Li, Zhang, Cao, Hu, & Guo, 2021). In this approach, optical fibers guide solar radiation from the exposed face of the panel to photovoltaic cells positioned at the opposite face or inside the element. The efficiency of this approach depends on light coupling conditions, fiber arrangement, and transmission losses, which are not yet consistently quantified in the literature.

Structural health monitoring through fiber-optic sensing is one of the most studied functional directions (Makul, 2020). In this configuration, the embedded fiber network serves as both a light-transmitting medium and a sensor. Variations in the optical signal caused by strain, microcracking, or fiber damage can be measured at the fiber ends and correlated with the structural condition of the element. Laboratory studies have shown the possibility of detecting crack initiation, crack propagation, and load variation in beams and panels (Merzbacher et al., 1996). The reliability of this approach depends on the stability of the optical signal and the durability of the fiber-matrix system under service conditions. Representative examples of these application directions are presented in Figure 1.11.

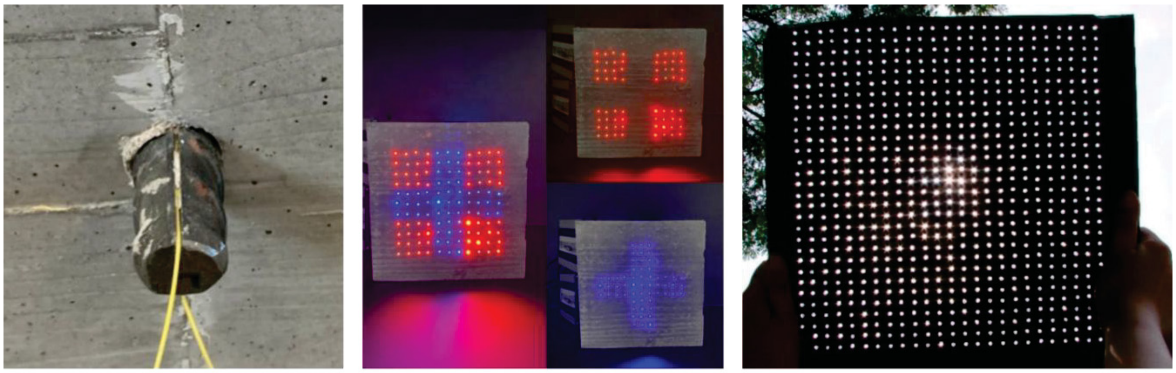

Figure 1.11 Applications of light-transmitting concrete (LTC): (a) optical fiber sensing embedded in reinforced concrete, (b) decorative furniture panels, (c) translucent facade panel demonstrating natural light transmission potential for reduced artificial lighting Reproduced and adapted with the permission of CC BY 4.0 license (Lemcherreq et al., 2022; Štochl et al., 2023; Huang & Lu, 2020)

Across these application areas, the transition from laboratory studies to practical installations has been more consistent in architectural uses, where performance can be assessed visually and structural requirements are less restrictive. Functional uses involving sensing, energy conversion, or communication remain at earlier stages of development and still require improved integration methods, durability assessment, and more consistent performance evaluation before broader implementation. These differences reflect the current limitations of LTCC systems, in which optical performance can be achieved under controlled conditions, while mechanical reliability, reproducibility and cost-effectiveness require more research and development to further expand practical applications.

1.9 Current challenges and future prospects

After approximately two decades of research, fiber-optic LTCCs continue to face a set of interconnected challenges that limit their broader implementation. These challenges can be broadly grouped into four aspects: standardization, mechanical-optical balance, durability, and practical implementation.

- The lack of standardized procedures remains a central limitation. Variations in optical measurement methods, including differences in instrumentation, environmental conditions, and reporting formats, make comparison between studies difficult (Al-Sodani, 2025; Bai et al., 2024; Chiew, Ibrahim, Mohd Ariffin, et al., 2020). Similar variability is observed in mechanical characterization and fabrication procedures, where differences in matrix composition, fiber arrangement, and testing configuration influence reported performance. This issue is particularly evident in transmittance measurements, where inconsistent methodologies obscure the relationship between material parameters and reported results. More consistent reporting and controlled experimental conditions are required to improve comparability and to support clearer identification of material-related trends.
- The balance between optical and mechanical performance also represents an important design constraint. Increasing fiber volume fraction generally improves light transmission but is often associated with reductions in compressive and flexural strength due to increased porosity and interfacial effects (Al-Sodani, 2025; Chiadighikaobi et al., 2023). This trade-off reflects the coupled nature of LTCC systems, in which design parameters simultaneously influence optical and mechanical behavior. While this relationship is well documented, predictive models that can describe this balance across different matrix systems are still limited.
- Fabrication methods present additional challenges. Current approaches frequently rely on manual fiber placement, which is time-consuming and limits scalability (Bai et al., 2024; Shen, Li, Zheng, Liu, & Wang, 2026). In addition to scalability, manufacturing influences fiber distribution, alignment, and defect formation, which contributes to variability in both optical and mechanical performance. Advances in automated fabrication techniques may help address these limitations.
- Durability considerations further contribute to uncertainty regarding long-term performance. As discussed in Section 1.7, the influence of fiber-matrix interaction on transport properties and environmental resistance remains insufficiently characterized, particularly under combined exposure conditions. The lack of long-term and standardized durability data limits the ability to assess performance under service conditions.

Although there are many challenges, there are several directions that offer potential for future development. Alternative translucent systems, including resin-based materials and glass-based inclusions, have been explored as cost-effective options, although their behavior differs from fiber-based LTCC and requires further evaluation (Al-Sodani, 2025). In addition, improved experimental methodologies and more consistent reporting practices would support a more reliable comparison of results across studies.

From a broader perspective, LTCC continues to present potential as a material combining structural and optical sensing and light-transmitting functions. In particular, its integration with structural health monitoring systems, through light transmission or embedded sensing strategies, represents a promising application for real-time condition assessment in infrastructure. In addition, emerging uses in architectural lighting and visual communication further expand its functional scope. Future progress is expected to depend on improved reproducibility, clearer interpretation of experimental results, and better understanding of long-term performance. Further developments in standardization, fabrication methods, durability assessment, and system-level design may support a more reliable evaluation of performance and clarify where this material can be realistically applied in construction.

CHAPTER 2

EXPERIMENTAL AND THEORETICAL INVESTIGATION OF OPTICAL TRANSMITTANCE IN LIGHT-TRANSMITTING CONCRETE

Karina Hwang Arcolezi [a, b], Camila Aparecida Zimmermann [b], Bora Ung [b], Claudiane Ouellet-Plamondon [a]

[a] Department of Construction Engineering, École de technologie supérieure,
1100 Notre-Dame Ouest, Montréal, Québec, Canada H3C1K3
[b] Department of Electrical Engineering, École de technologie supérieure,
1100 Notre-Dame Ouest, Montréal, Québec, Canada H3C1K3

Article published in *Measurement Science and Technology*, Vol. 37, April 2026, available at https://doi.org/10.1088/1361-6501/ae6521

Abstract

Light-transmitting concrete (LTC) is a cement-based composite that incorporates optical fibers to allow light transmission through cementitious composites elements, enabling architectural lighting. Despite growing interest in its optical performance, LTC lacks standardized procedures for measuring light transmittance, particularly concerning the distance between the specimen and the photodetector. This study addresses this gap by introducing a physical model based on a super-Gaussian intensity distribution to describe the light behavior emitted from embedded optical fibers. The model is validated through experimental tests using 5 cm cubic LTC specimens with up to 16 fibers and detector distances ranging from 1 to 20 cm. The results reveal a nonlinear relationship between detector distance and measured transmittance, with an optimal detection distance observed around 5 cm for the investigated configurations. Specifically, for the 16-fiber configuration, the peak transmittance reached 0.33% at the optimal distance, which is higher than the 0.23% recorded at 1 cm or the 0.17% at 20 cm. Based on these findings, a practical predictive rule is proposed, linking this optimum to the fiber's numerical aperture and the specimen's dimensions. By providing a physically grounded framework for reliable optical transmittance measurements, the proposed approach highlights the potential of LTC for use in functional and smart concrete systems. Moreover, it contributes

to the standardization of measurement procedures, enabling more consistent and reproducible evaluations of LTC performance in both research and industrial contexts.

2.1 Introduction

Light-transmitting concrete (LTC) and other cement-based composites are gaining recognition as materials that incorporate translucent or light-guiding components capable of transmitting light through the cementitious matrix (Chiew, Ibrahim, Mohd Ariffin, Lee, & Singh, 2023; Luhar et al., 2021; Said, 2020; Shen & Zhou, 2013). These properties support applications in architectural design, integrated lighting systems, and sustainability-focused construction (Chiew et al., 2023; Chiew, Ibrahim, Sarbini, et al., 2020). Beyond its aesthetic appeal, LTC's ability to harness natural light can help reduce energy consumption from artificial lighting, thereby reinforcing interest in its optical behavior (Ahuja & Mosalam, 2017; Navabi, Amini, Rahmati, & Tahbaz, 2023; Shen & Zhou, 2021; Su, Zhang, Luo, & Liu, 2022). More broadly, cement-based composites incorporating optical fibers have been described in the literature as systems with passive or active optical behavior (Inaudi et al., 2005). In passive configurations, such as conventional light-transmitting concrete, optical fibers guide light through the cementitious matrix, and optical transmittance is used to characterize the material's optical response. In active configurations, optical fibers are integrated into systems that enable interaction with external stimuli, supporting functionalities such as sensing, signal transmission, or image-related applications (Arcolezi et al., 2025).

The efficacy of light transmission in LTC depends on parameters such as the diameter and content ratio of optical fibers (Henriques, Dal Molin, & Masuero, 2018; Yue Li, Li, & Guo, 2015; Mei Chiew, Syahrizal Ibrahim, Azreen Mohd Ariffin, Lee, & Kumar Singh, 2022; Nam et al., 2022), the spatial distribution of fibers and their density within the composite (Altlomate, Alatshan, Mashiri, & Jadan, 2016; Mei Chiew et al., 2022; Pourkazemi, Vahdati, Mirvalad, & Mahdikhani, 2024; Shenoy, Nayak, Tantri, & Shetty, 2022), characteristics of the light source, such as wavelength and power (Yue Li, Li, Wan, & Xu, 2015; Nam et al., 2022; Navabi et al., 2023; Sharifi, Navabi, & Mosavi, 2023), the numerical aperture (NA) of the optical fibers

(Huang, 2020; Su et al., 2020; Su, Zhang, Luo, et al., 2022), and the distance between the sample and the detector (Yue Li, Li, Wan, et al., 2015; Sharifi et al., 2023; Tahwia, Abdelaziz, Samy, & Amin, 2022). Owing to the large number of variables involved in the light transmittance measurements of LTC, there is considerable variation in the methodologies used in the scientific literature. This variability limits the comparability of reported results and affects the assessment of cement-based composites with optical fibers in both passive and active configurations. In this work, we theoretically and experimentally study the main parameters that influence light transmittance measurements of LTC with optical fibers and identify conditions that support more consistent and reproducible measurement procedures.

Light transmission in optical fiber-based LTC is enabled by the inclusion of optical fibers within a cementitious matrix (Chiew et al., 2023). Studies have consistently shown that increasing the optical fiber content and diameter tends to enhance light transmittance (Yue Li, Li, & Guo, 2015b; Mei Chiew et al., 2022), while an increase in the distance between the sample and the photodetector leads to a reduction in transmission due to light dispersion (Henriques et al., 2018; Yue Li, Li, & Guo, 2015; Mei Chiew et al., 2022; Rong et al., 2023; Štochl, Vychytil, & Hájek, 2023). Despite these well-established trends, light transmittance measurement in optical fiber LTC lacks standardization, leading researchers to adopt diverse testing methods across studies (Bai et al., 2024; Henriques, Dal Molin, & Masuero, 2020). The absence of standardized methods for measuring detector-sample distance constitutes a significant gap in the field that the present study aims to address.

Experimental studies have highlighted the influence of detector distance on transmittance measurement results. Rong et al., (2023), in their investigation of LTC wall panels, observed that light intensity decreased from a measured peak of 46 lux to 11.8 lux as the distance from the sample and the light meter increased from 10 cm to 50 cm, regardless of the fiber configurations tested. Similarly, Robles et al., (2020) reported a gradual decrease in optical power, with increasing detector distance, with a more pronounced effect at distances between 0 and 100 mm. They found that at distances greater than 10 cm, the optical power ratios for

LTC samples with different fiber diameters converged, suggesting that the impact of fiber diameter on transmittance diminishes at larger distances.

Consistent trends have also been reported for different fiber diameters and sample geometries. Nam et al., (2022) reported a significant decrease in light intensity, as the detector distance increased from 10 cm to 30 cm when analyzing samples with fiber diameters ranging from 0.75 mm to 1.5 mm. The authors found that while larger fibers allowed higher initial power, they were also more susceptible to light dispersion over longer distances. Notably, fibers with a large diameter of 1.5 mm exhibited the highest power at any given distance, but experienced the highest drop as the detector moved farther from the sample, with an average light power reduction from approximately 100 μW at 10 cm to 10 μW at 30 cm. Tuaum et al., (2018) investigated the effect of detector distance on light transmittance in LTC by measuring light intensity through samples with 2 mm and 3 mm diameter optical fibers at distances ranging from 10 to 50 cm. They found that transmittance decreased by increasing the detector distance. For 2 mm fibers with a 6% volume fraction, transmittance decreased from approximately 22% at 10 cm to approximately 12% at 50 cm. For 3 mm fibers, under similar conditions, transmittance decreased from approximately 19% at 10 cm to approximately 10% at 50 cm. These studies collectively reinforce the sensitivity of the measured optical output to detector-sample distance, highlighting the need for a clearer understanding of how this parameter affects reported values.

Despite the recognized effect of detector-sample distance on transmittance measurements, this parameter is still treated empirically, often lacking explicit physical justification or a standardized criterion for detector placement. As a result, measurement distances are frequently selected based on experimental convenience rather than on optical propagation considerations. The present work addresses this gap by introducing a predictive framework for detector placement based on super-Gaussian beam propagation. This approach correlates the optimal detection distance with sample geometry and fiber numerical aperture, providing a physically grounded basis for optical measurements in light-transmitting concrete.

Building on the identified gap in light-transmission measurements, this study aims to address the following research question: How does the distance between the light detector and the light-transmitting specimen influence the detected light power, and what is the optimal distance for reliable transmission measurements?

By integrating a theoretical model of light distribution from embedded fibers (Rativa & Vohnsen, 2011; Shealy & Hoffnagle, 2005) with experimental evaluations of LTC samples across varying fiber volume fractions, this work aims to quantify the relationship between detector positioning and measured optical power. The objective is to identify a stable distance range that ensures representative and reproducible transmittance measurements. Ultimately, this research establishes a physically grounded methodology for the optical characterization of light-transmitting concrete, providing a consistent basis for evaluating both passive and optically active configurations in smart concrete research.

2.2 Materials and methods

2.2.1 LTC samples preparation

Samples of LTC with different quantities of optical fibers were fabricated and analyzed. The cementitious matrix was inspired on limestone-calcined clay cement (LC^3). Ordinary Portland cement (type GU, conforming to CSA A3000 standards (CSA A3000, 2018)) served as a primary binder, supplemented with calcined clay and limestone filler, and natural river sand as fine aggregate, and a polycarboxylate-based superplasticizer. The mortar cube production method followed the approach described by Arcolezi, Ung, & Ouellet-Plamondon, (2024) Jin, Caron, & Ouellet-Plamondon, (2025). The optical fibers used in this study are made of polymethyl-methacrylate (PMMA) with a core diameter of 1 mm, featuring high transparency in the visible spectrum suitable for light guiding (Alonso Romero et al., 2023; Navabi, Javidruzi, Hafezi, & Mosavi, 2021). Table 2.1 summarizes the properties of the PMMA fiber used (Eska™).

Table 2.1 Composition and properties of the partially translucent material

Core material	Polymethyl-methacrylate resin
Core diameter	0.92 – 1.04 mm
Core refractive index	1.49
Cladding material	Fluorinated polymer
Cladding diameter	0.94 – 1.06 mm
Cladding refractive index	1.40
Refractive index profile	Step-index
Numerical aperture	0.5
Attenuation at 650 nm	≤ 0.0002 dB/mm
Operation temperature	-55ºC to 70ºC
Tensile strength	83 MPa
Core material	Polymethyl-methacrylate resin

To minimize misalignment losses, fibers were threaded through rigid, precision-drilled formwork plates at both the input and output faces of the cubic molds. This ensured the fiber longitudinal axes remained perpendicular to the concrete surface and parallel to the incident light source, thereby reducing coupling losses associated with the fibers' acceptance cone (Chiew et al., 2023).

Cubic LTC samples of 5 cm side length were used to evaluate the influence of fiber quantity on light transmittance. Optical fibers were arranged in a square lattice pattern to provide a standardized, reproducible geometric baseline for validation against the theoretical model. While other distributions (e.g., random or hexagonal packing) are possible, the square arrangement simplifies the geometric variables required for the model. The number of fibers in a sample progressively increased, from a single fiber to 4, 9, and 16 fibers. Figure 2.1 illustrates the fiber distribution within the various samples and the corresponding photographs for each configuration.

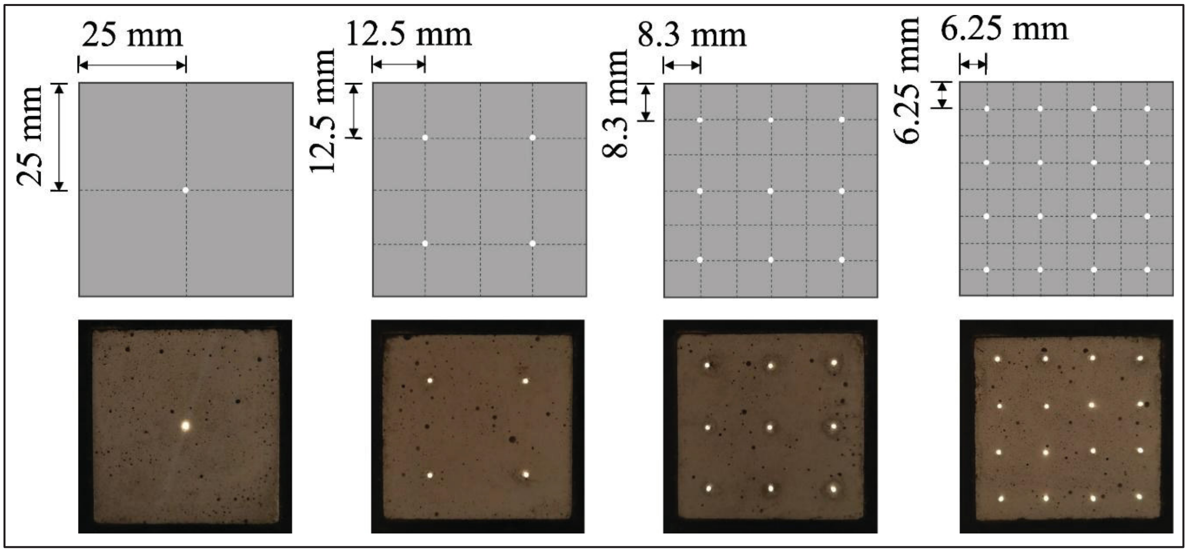

Figure 2.1 Distribution of optical fibers embedded in light-transmitting concrete samples. Fibers are shown for configurations with different numbers of fibers (N = 1, 4, 9, 16)

2.2.2 Light transmission analysis

Light transmittance tests were conducted within a matte black cardboard enclosure to minimize reflections of light on the inner walls that would otherwise contaminate the measurements (Huang, 2020). To ensure that only light passing through the fibers was measured while effectively blocking ambient light, two walls were constructed around the specimen to prevent light leakage (Figure 2.2). A 6 W LED light bulb with a peak wavelength of 600 nm and a high-power RGB LED with peak wavelengths of 630 nm, 528 nm, and 465 nm were employed as light sources. Each color channel of the RGB LED was calibrated to a constant output intensity (3 W per channel) to ensure consistency across wavelengths, enabling accurate comparison of light transmittance. All experiments were conducted in a standard room temperature and humidity (around 21ºC and 40% relative humidity) in a laboratory environment to prevent variability from external environmental factors. These conditions are comfortably within the operating range specified for PMMA fibers in Table 2.1, ensuring that their optical behavior remains unchanged during testing. The cementitious matrix is also not expected to undergo any measurable variation in optical response under such mild and stable environmental conditions.

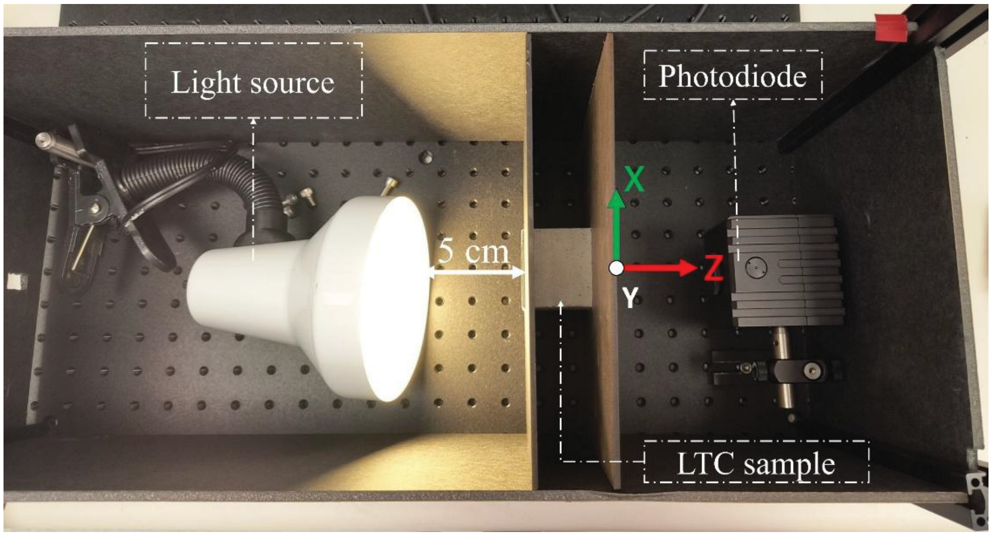

Figure 2.2 Experimental setup for light transmission measurements, showing the sample, light source, and detector (top cover removed for clarity)

To characterize the spectral distribution of the transmitted light, the spectrum of each light source was measured using an optical spectrometer (HR4000CG, Ocean Optics Inc.), while optical power measurements were performed using an integrating sphere photodiode (S142C, Thorlabs Inc.) connected to a power meter interface (PM100USB, Thorlabs Inc.). The distance between the light source and the sample was fixed at 5 cm to ensure uniform illumination conditions across the entire 50 × 50 mm^2 sample face throughout the experiment. The photodetector was centered both vertically and horizontally with respect to the sample, and the distance between them (Figure 2.2, z-axis) was systematically varied to assess its impact on the transmittance measurements and determine the optimal distance.

The photodiode features a 12 mm input diameter aperture, which is substantially smaller than the specimen's output surface. Since the detector samples are only a portion of the emerging light beam, the measured signal depends not only on the total transmitted power but also on how the light is distributed across the sample's exit face. Optimization of the sample-detector distance is required to identify the location where this specific aperture size captures a stable and representative fraction of the non-homogeneous light distribution from the fiber array, improving the consistency of the transmittance measurements.

The initial light power (P_0) was recorded each time the specimen or the distance between the specimen and the photodiode was modified, to ensure a consistent reference P_0 value. Additionally, a control specimen (without optical fiber) was tested to confirm that the photodiode reading was 0 µW (perfectly opaque), thereby verifying that the walls effectively blocked external light and that no light leaked around the sample's edges. For each testing configuration, two samples were evaluated for light transmittance, and each measurement was performed twice to verify the stability of the signal. The average value was calculated to ensure consistency and repeatability of the measurements.

The light transmittance (T), in units of %, was calculated, using Equation (2.1), by comparing the reference power from the light source (P_0) with the light power transmitted after passing through the sample (P_1) in µW units:

$$T = \frac{P_1}{P_0} \times 100 \tag{2.1}$$

The theoretical model of transmittance of the LTC needs to consider the specific properties of both the cementitious sample and the optical fibers that it contains. The optical fibers used in this study have a specified attenuation of 0.002 dB/cm at 650 nm. This loss can be converted to a transmission percentage using the expression $k = 100 \times 10^{\left(-\frac{\alpha L}{10}\right)}$, where k is the attenuation factor, α is the transmission loss coefficient in dB/cm, and L is the optical fiber length in cm (Su et al., 2020). For an optical fiber length of 5 cm, this attenuation yields a theoretical fiber transmission of $T_{Fiber} = 99.8\%$ of the light incident on the fiber core at the entrance facet. The maximum theoretical transmittance of the sample can be estimated by summing up the transmission efficiency of the optical fibers with their contribution to the total surface area of the specimen. Specifically, the max theoretical transmittance (T_{max}) is defined as the total cross-sectional area of the fibers, multiplied per the number of fibers ($S_{Fiber} \times N$), times the fiber transmission, over the total surface area of the sample (S_{Sample}), as described in Equation (2.2).

$$T_{max}(\%) = \frac{(S_{Fiber} \times N) \times T_{Fiber}}{S_{Sample}} \tag{2.2}$$

2.2.3 Determination of the optimal distance between the sample and the detector for power detection optimization

To determine the optimal testing distance between the LTC sample and the photodetector, a theoretical model of light transmittance was developed that incorporates parameters such as the light source characteristics, the numerical aperture (*NA*) of the optical fibers, and the sample dimensions. The *NA* defines the light acceptance angle of the fiber and depends on the refractive indices of the core and cladding (Su, Zhang, Luo, et al., 2022). This model assumes the use of multimode optical fiber with a step-index refractive profile, which is commonly employed in light-transmitting applications owing to their large surface area and power handling (Rativa & Vohnsen, 2011). These fibers typically emit a light beam whose profile is nearly Gaussian in shape. The super-Gaussian profile is chosen for the model because it better accounts for the more complex light distribution seen in multimode fibers (Gillen-Christandl, Gillen, Piotrowicz, & Saffman, 2016; Rativa & Vohnsen, 2011). In fact, the super-Gaussian distribution captures the effects of both beam divergence and intensity decay over the distance from multimode fibers more accurately, compared to single-mode fibers where a standard Gaussian beam profile model would be more suitable (Gillen-Christandl et al., 2016; Shealy & Hoffnagle, 2005).

The general form of the super-Gaussian intensity profile as a function of radial distance *r* (m) from the beam center is given by Equation (2.3) (Shealy & Hoffnagle, 2005).

$$I(r,z) = I_0 \cdot \exp\left(-2\left(\frac{r}{w(z)}\right)^n\right) \tag{2.3}$$

Where *I(r)* is the intensity at radius *r* (W/m²), I_0 is the peak intensity in W/m^2, and *w* is the beam radius (m) which grows with propagation distance as $w(z) = z \cdot \tan\theta + w_0$. In the last expression, we note that the radius of the initial beam width (w_0) is taken as the core radius of the optical fiber (0.5 mm) and the divergence angle θ of light output from an optical fiber is given by $\theta = \sin^{-1}(NA)$. For n = 1, the profile corresponds to a conventional Gaussian distribution, while the expression with $n > 1$ describes a flatter and sharper beam profile (Gillen-Christandl et al., 2016). The beam shape is an important element that determines the light distribution and intensity received by the detector (Rativa & Vohnsen, 2011). The input power P (in μW) from the light source is distributed over the cross-sectional area of the beam, leading to the peak intensity I_0 at the center of the beam (in μW/cm²). This peak intensity is calculated assuming a uniform power distribution over a circular cross-section with radius w (cm²), and given by $I_0 = \frac{P}{\pi w^2}$.

The beam divergence from a single optical fiber generates a conical beam profile where the light spreads symmetrically around the propagation axis (Figure 2.3). As the beam radius increases with distance, the intensity of the light decreases due to the distribution of optical power over a larger area. The incorporation of N fibers thus yields N conical beams of light that overlap, resulting in regions of higher light intensity, as well as darker regions in areas between adjacent fibers (Figure 2.3). This highlights the importance of properly choosing the location of the photodetector to maximize light detection. Assuming that the N fibers are evenly distributed on the surface of a given LTC sample, the optimal location of the photodetector that best approximates the overall LTC transmittance will be aligned with the center of the sample and located at a distance z that maximizes the amount of transmitted light measured at the detector. Such optimal detector position should enhance the accuracy and reliability of power detection and transmittance measurements in the evaluation of fiber-based LTC samples.

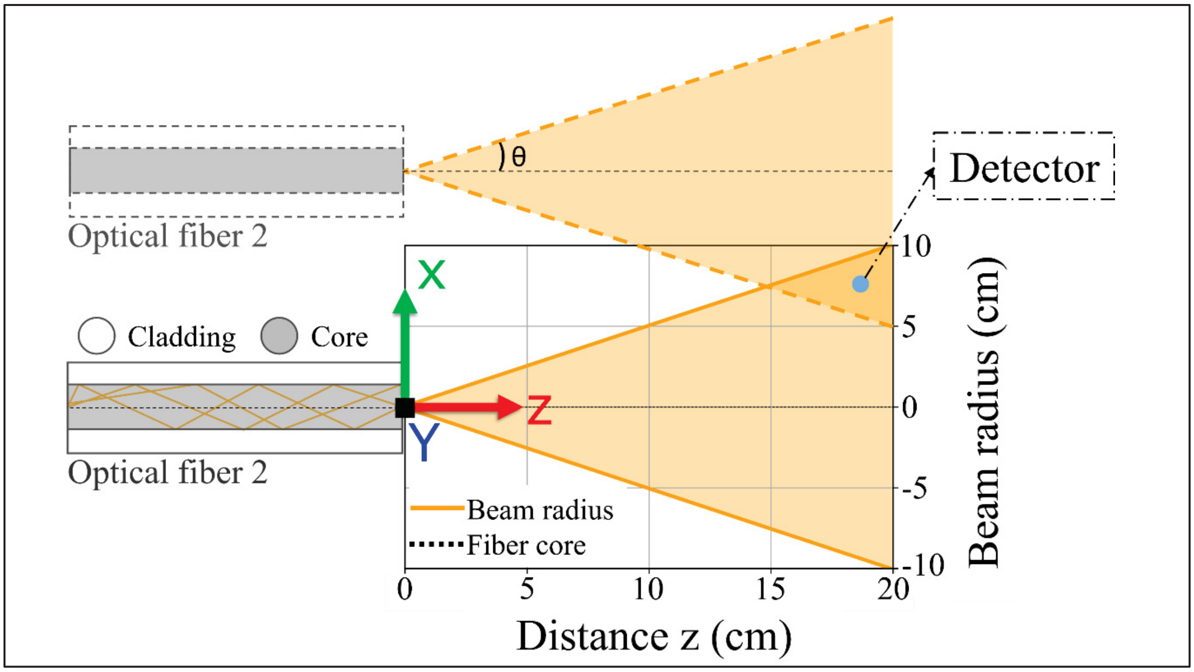

Figure 2.3 Conical beam profiles from optical fibers and their overlap, illustrating the region of intensified light intensity for optimized power detection

The model simulates the power detection efficiency of the beam as it exits the optical fiber and propagates through free space. The objective is to quantify the percentage of light power detected by a circular detector positioned at varying distances from the fiber while accounting for attenuation over a specific fiber length. The model integrates the power detected by the circular photodetector (diameter of 12 mm) at a given distance *z* from the center of the sample's output surface. The optical power measured by the circular detector ($P_{detector}$) is computed by integrating the total light intensity produced by the *N* super-Gaussian beams (output from the *N* fibers) over the detector's area ($A_{detector}$) via the double integral in Equation (2.4), where the integration bounds along the *x* and *y* coordinates are defined by the detector's dimensions in the *x*-*y* directions (Figure 2.3). The theoretical model focuses on square lattice fiber configurations to simplify the initial complexity of the multi-fiber system and establish the fundamental geometric criteria for light distribution analysis.

$$P_{detector}(z) = \iint_{A_{detector}} \left[\sum_{i=1}^{N} I_i(r,z) \right] dx\, dy \qquad (2.4)$$

The modeling approach incorporates a geometric criterion to define the optimal measurement position. This criterion is based on the hypothesis that the ideal distance corresponds to the point where the expanding light cones, originating from the outermost fibers, begin to overlap at the detector plane. At this specific distance, the detector is expected to record a portion of the emerging field that best represents the total transmitted power. This geometric principle, which considers the beam divergence characteristics and the dimensions of the optical arrangement, provides the physical basis for the predictive rule developed in this study.

Subsequently, the fraction of power detected in watts at each distance z (cm) is evaluated. By simulating the beam profile at different distances, considering factors such as beam divergence, detector offset, and fiber attenuation, this theoretical model (Equations (2.3-2.4)) provides a physically accurate description and enables a systematic investigation of an optimal detection distance for light transmittance studies in LTC samples.

2.3 Results and discussions

2.3.1 Beam profile and transmittance analysis

Parameter n for the super-Gaussian model was determined by comparing the experimental beam profile, captured using a visible camera (EO-0413M CMOS monochrome, Edmund Optics), to theoretical profiles simulated for various values of n. The output beam profile from an optical fiber was experimentally measured at a distance z = 30 cm (from the fiber output), shown in Figure 2.4(a). The measured beam profiled was analyzed by extracting its intensity distribution along a cross-sectional line (dashed red line in Figure 2.4a) through the optical beam's center and presented in Figure 2.4(b) as the solid red curve. Several theoretical profiles (n = 1, 2, 3, and 5) of super-Gaussian beams (see Equation (2.3)) were compared. The Gaussian profile (n = 1) is narrower than the measured beam, underestimating the width of the emission. The profile with n = 2 better represents the peak intensity but remains slightly narrower than the actual distribution. The curve with n = 3 provided the best overall agreement, capturing both the peak and the broader intensity tails of the measured beam. Higher values of n, such as 5, produced profiles with very sharp edges resembling a top-hat distribution (Belay et al., 2022;

Gillen-Christandl et al., 2016; Yoshizaki & Nakao, 2023) that could be suited for other types of multimode fibers, such as with larger core diameters for example.

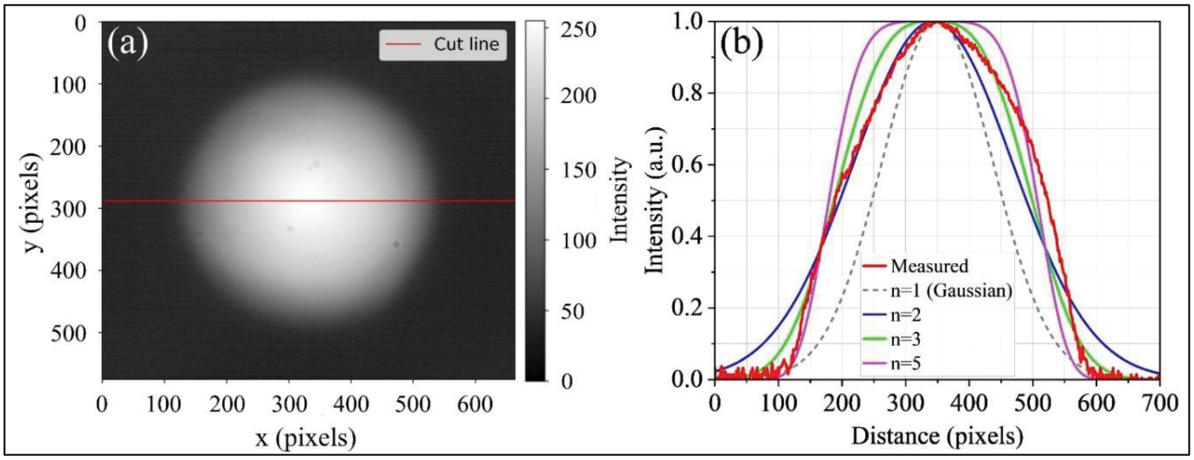

Figure 2.4 Comparison of (a) measured beam profile and (b) intensity distribution compared with super-Gaussian models for different n values

The arrangements of optical fibers for each LTC sample are detailed in Figure 2.1. Figure 2.5 displays the modeled beam profile for a single fiber centrally positioned, and as a function of distance z, where the blue circle at the center represents the detector. In this special configuration ($N = 1$), there is no obvious optimal distance since the detected light power is maximum at $z = 0$ and simply decays with the distance $z > 0$. Still, the modeled beam profiles in Figure 2.5 highlight the beam divergence phenomenon (and expanding beam profiles) with increasing distance from the fiber output (Gillen-Christandl et al., 2016).

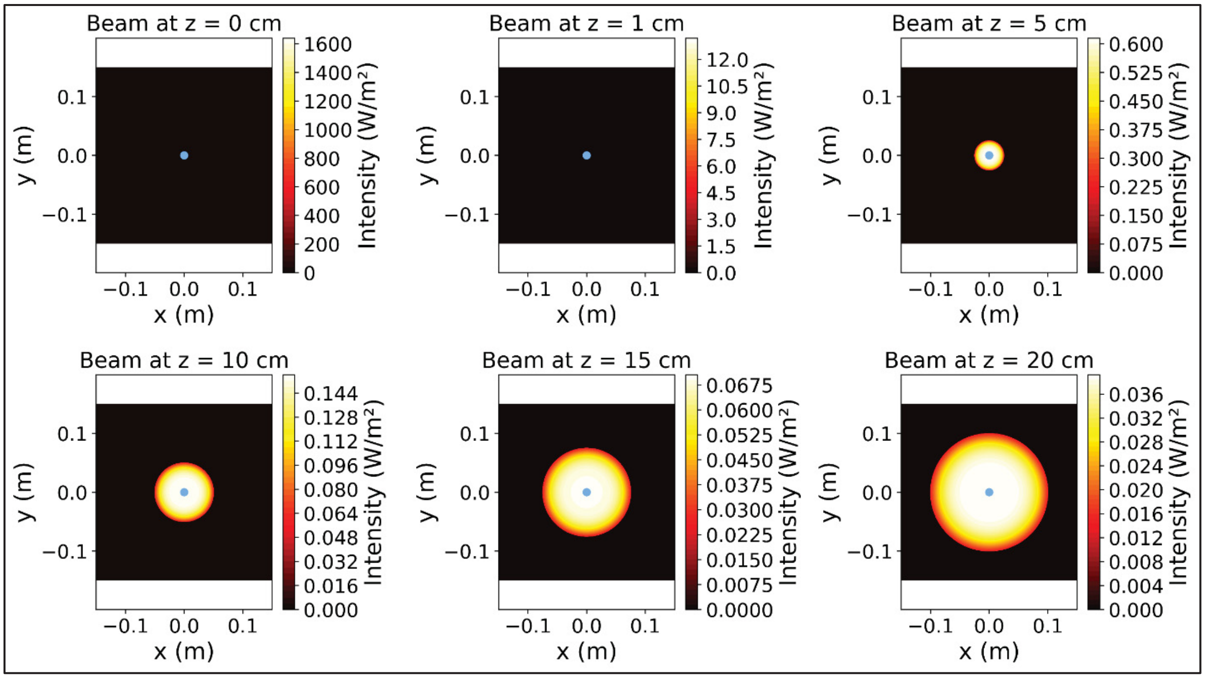

Figure 2.5 Light intensity distribution at various distances z from the N=1 optical fiber sample (detector area: blue circle)

For samples with multiple optical fibers ($N > 1$), there is an optimal distance for the detector where the measured optical power is maximum. For the four-fiber sample, the analysis also considers optical fiber offsets relative to the center of the specimen. In this setup, positioning the detector too close to the specimen (i.e., at $z = 0$ or 1 cm in Figure 2.6) may result in failure to detect any light power emitted from the light cones, since the center of the sample does not contain any fiber. As the distance increases, the light cones expand, allowing the center-aligned detector to capture more power (Figure 2.6). There is thus potentially an optimal distance z at which to position the detector so as to maximize light collection, as we will see in the next section.

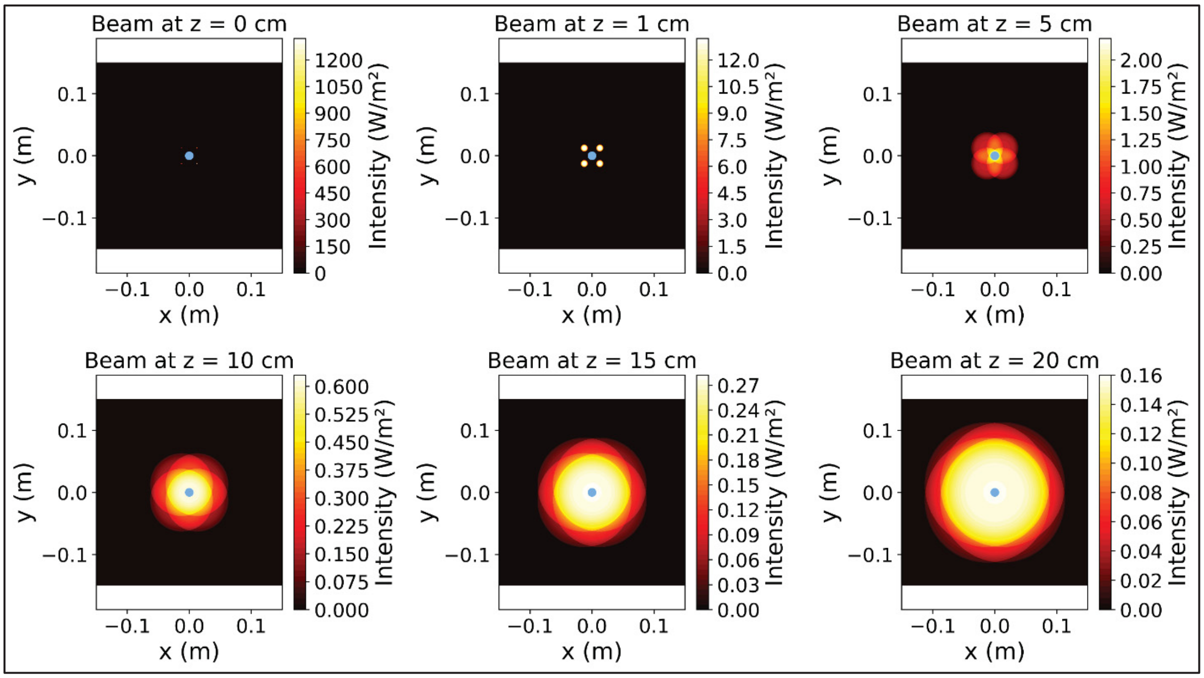

Figure 2.6 Light intensity distribution at various distances z from the N=4 optical fiber samples (detector area: blue circle)

In the nine-fiber configuration ($N = 9$), a central fiber aligns with the detector. If considering only this central fiber, the optimal detection distance would place the detector as close as possible to capture its light output (i.e., $z = 0$). However, the additional eight fibers complicate this arrangement. For effective detection of the maximum overlap intensity from all nine fibers, the detector must be positioned farther away. As seen in Figure 2.7, increasing the distance from the sample allows the light cones from all 9 fibers to expand, resulting in greater overlap of their profiles. Thus, determining the optimal distance requires balancing light capture across the entire fiber array, accounting for both the central and surrounding fibers.

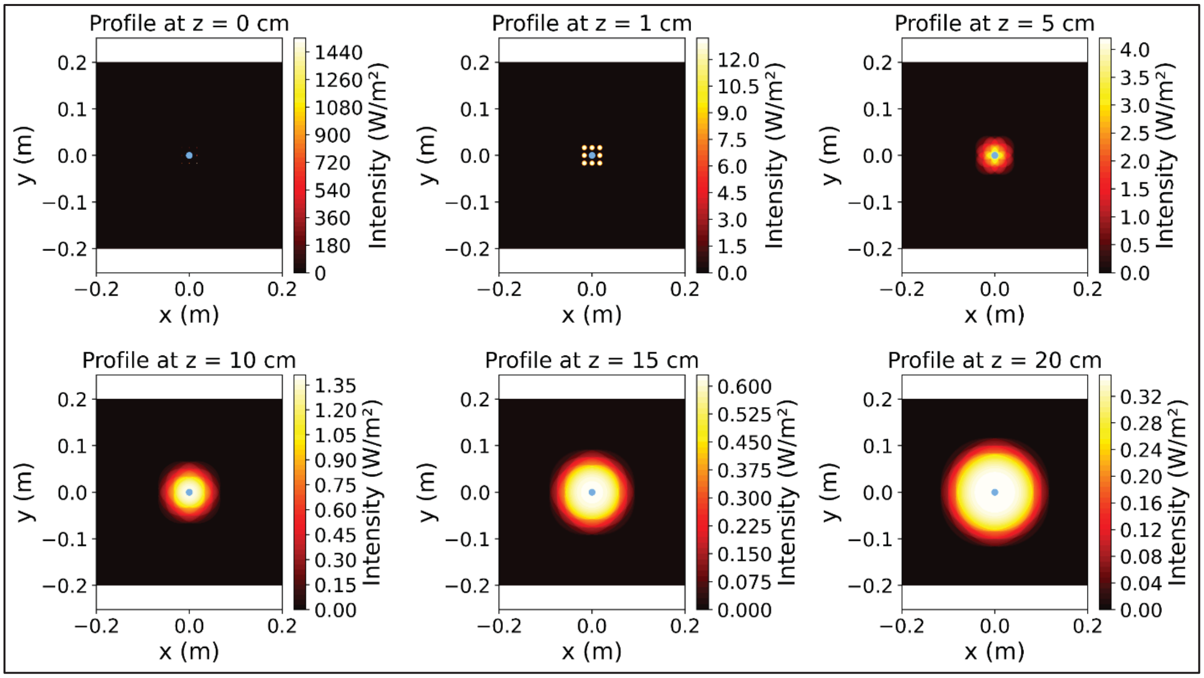

Figure 2.7 Light intensity distribution at various distances z from the N=9 optical fiber samples (detector area: blue circle)

For the $N = 16$ fibers configuration, the center-aligned detector can capture light cones from the four innermost fibers at shorter distances ($z < 5$ cm), most effectively. However, to maximize light capture from all 16 fibers, including the twelve fibers positioned along the sample's periphery, the detector needs to be placed at a greater distance. As the detector is moved further away from the sample, the light cones from each fiber expand, again enhancing the overlap among their profiles as well as a more uniform intensity distribution (Figure 2.8).

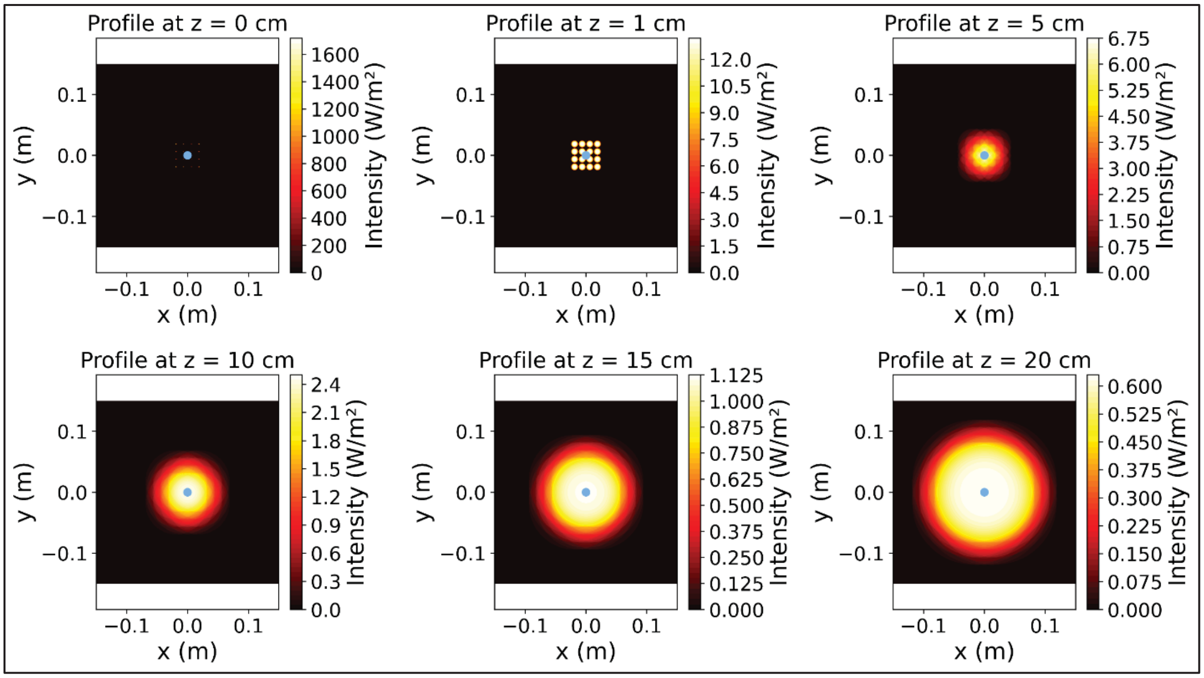

Figure 2.8 Light intensity distribution at various distances z from the 16 optical fiber samples (detector area: blue circle)

The beam profile analysis across varying distances and fiber configurations demonstrates the influence of fiber arrangement on light distribution and detection efficiency. For single-fiber setups, closer detector positioning maximizes light capture. Conversely, in multi-fiber configurations, the detection distance must be optimized to account for the overlap of light cones with the detector area, ensuring efficient capture of light from all fibers while maintaining sufficient intensity.

The experimental results, presented in Figure 2.9, provide a quantitative analysis of transmittance as a function of detection distance, fiber quantity, and light source. Each plot depicts transmittance (%) for different fiber quantities (N = 1, 4, 9, 16 fibers) across detection distances of z = 1, 2, 5, 10, 15, and 20 cm. The analysis is performed with two types of visible light sources (LED white light bulbs and RGB LEDs), which represent commonly used types of ambient illumination sources. Additionally, the dashed lines in Figure 2.9, indicate the highest theoretical transmittance that the samples could achieve based on the model described in the previous section. These theoretical curves (i.e., dashed lines in Figure 2.9) were calculated using Equation (2.2) and serve as a reference for evaluating the experimental results, providing a benchmark for understanding the efficiency of light transmission across the different fiber configurations.

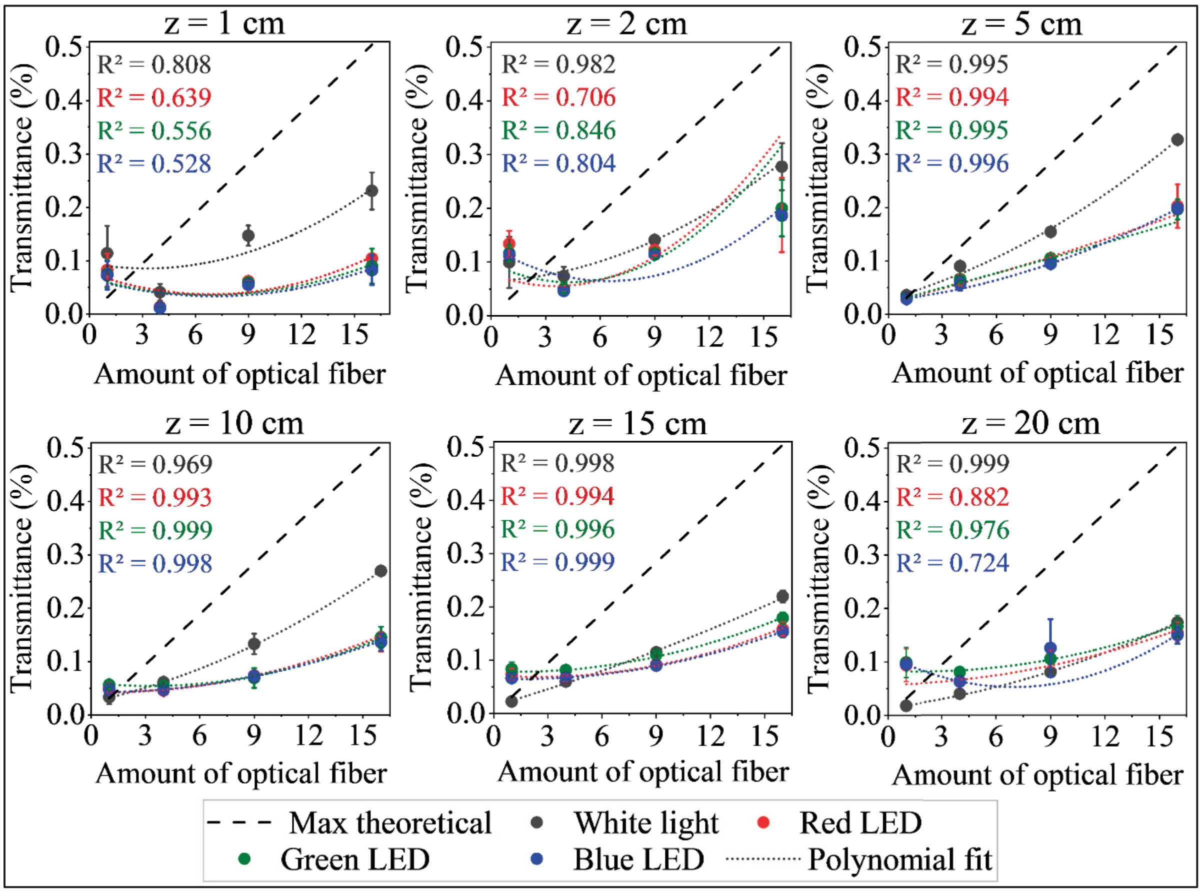

Figure 2.9 Measured light transmittance (%) in LTC samples as a function of fiber quantity and detector-distance (z) for each light source

The discrepancy between the experimental transmittance values and the theoretical maximum predicted by the model can be attributed to several factors. First, imperfections in fiber cleaving can reduce light coupling efficiency (Henriques et al., 2018). Second, the model assumes ideal conditions, such as a defect-free fiber and a perfectly stable light source, which do not fully reflect experimental conditions. Additionally, the model does not account for the acceptance angle of the fibers, which limits the amount of light that can be effectively guided (Chiew et al., 2022). The variability across measurements remained low, with standard deviations ranging from 0.000% to 0.013%, which indicates consistent behavior between the two specimens tested for each configuration.

Furthermore, the model assumes ideal fiber alignment. While the fibers are threaded through precision-drilled plates to minimize misalignment, any minor deviation from the longitudinal axis can result in an asymmetric output beam. Additionally, while the matrix is largely opaque, internal reflections at the fiber-matrix interface or scattering from minor surface imperfections near the fiber exit could introduce small deviations (Mbabazi, Luo, et al., 2026).

The increase in the number of fibers generally leads to higher transmittance across all detection distances, and also show that additional fibers enhance the overall transparency of LTC samples as expected (Henriques et al., 2018; Yue Li, Li, & Guo, 2015; Chiew et al., 2022; Nam et al., 2022; Sawant, Jugdar, & Sawant, 2014). For instance, at a detection distance of 1 cm with the white light source, transmittance rises from 0.11% with 1 fiber to 0.23% with 16 fibers – an approximate 102% increase. This trend of rising transmittance with more fibers persists at 20 cm, where transmittance reaches 0.17% for 16 fibers compared to 0.02% with 1 fiber, representing a 9-fold improvement. These results confirm that adding fibers consistently improves light transmission regardless of distance, though the absolute effect is more pronounced at shorter distances where light remains more concentrated (Robles et al., 2020). Interestingly, in certain configurations, such as the 1-fiber setup, experimental results occasionally exceed the maximum theoretical transmittance at specific detection distances. This unexpected result could arise from experimental factors such as light scattering and leakage, or temporal fluctuations in light source power.

The 4-fiber configuration presents a distinct trend, with lower transmittance than the 1-fiber setup at shorter detection distances, particularly at 1 cm and 2 cm (0.04% and 0.07% respectively, for the white light source). This behavior is due to the fiber distribution, with the center of the sample lacking fibers. When the detector is positioned very close to the sample, it captures less light from the light cones of the peripheral fibers, resulting in reduced transmittance, as previously discussed in the beam profile analysis. However, from 5 cm onward, the detector is positioned far enough to capture more light from the peripheral fibers, leading to higher transmittance for the 4-fiber configuration (0.09% at 5 cm). These findings suggest that while increasing fiber count generally benefits transmittance, fiber distribution and spacing, is important in optimizing illumination from LTC (Chiew et al., 2022; Sharifi et al., 2023; Shenoy et al., 2022; Shenoy, Nayak, Tantri, Shetty, & Mahesha, 2025).

For the 9-fiber configuration, transmittance values varied from 0.08% to 0.15% across the detection distances tested. At a short distance of 1 cm, transmittance reached 0.14%, reflecting effective light capture due to the proximity between the detector and the central fiber in the specimen. A slight decrease to 0.13% was observed at 10 cm, followed by a more pronounced reduction to 0.08% at 20 cm. This behavior can be attributed to the diminishing light intensity with increasing distance, as the emitted light becomes more dispersed over a larger area (Yue Li, Li, Wan, et al., 2015; Nam et al., 2022; Rong et al., 2023). The peak transmittance of 0.15% at 5 cm suggests that this intermediate distance allows for an optimal balance of light detected from the distributed fibers.

For the 16-fiber configuration, transmittance varied from 0.17% to 0.33%, with the highest value recorded at 5 cm. The increased fiber quantity enhanced light transmission across all distances. This is consistent with the denser fiber arrangement (6.25 mm spacing), which promotes higher light overlap, as illustrated in Figure 2.8. Interestingly, the results for the 16-fiber setup concur with findings by Chiew et al., (2022), who reported a transmittance of approximately 0.2% for 10 × 10 × 10 cm samples containing the same amount and diameter of fibers spaced 2.5 cm apart, at a detection distance of 10 cm. Despite the larger sample size in their study, the comparable transmittance values highlight the effectiveness of the compact fiber arrangement used here.

As has been well established, distance detection significantly influences transmittance behavior. At shorter detector distances, such as $z = 1$ cm and 2 cm, results in Figure 2.9 indicate an irregular behavior for configurations with low number of fibers (e.g., $N < 9$) because the detector is too close to the LTC sample, resulting in a sporadic overlap of the detector with the non-homogeneous light distribution. In contrast, at an intermediate detection distance of $z = 5$ cm, the light cones from each fiber expand sufficiently to allow a somewhat homogeneous light distribution to overlap with the detector, irrespective of the number of fibers in the sample. The distance aligns with the hypothesis, where the spatial arrangement provides the most balanced and representative power measurements. This results in a balanced transmittance distribution and optimal values for most configurations. As shown by the theoretical maximum transmittance line (Figure 2.9), the transmittance at this distance ($z = 5$ cm) approaches the calculated upper theoretical limits more closely than at other distances across different fiber quantities for the LTC samples used in this study, validating the methodological importance of the geometric overlap effect.

As the detection distance extends beyond 10 cm, a marked decline in transmittance occurs across all configurations, primarily due to increased light attenuation over longer distances. At these greater distances, light disperses further, diminishing the direct capture potential of the detector and spreading the light beyond the detector's effective area (Chiew et al., 2022; Rong et al., 2023). Although the rate of transmittance reduction is most pronounced between 1 cm and 10 cm, it begins to stabilize beyond 10 cm, indicating that the dispersion effect has a diminishing impact as the distance further increases, as was also reported by Rong et al., (2023). For instance, the transmittance drop between 5 cm and 20 cm is notably smaller than the initial decline, showing that while detected light decreases with distance, the dispersion effect attenuates more gradually over extended ranges.

The type of light source can also influence the transmittance behavior (Yue Li, Li, Wan, et al., 2015). In Figure 2.9, the white light source generally demonstrates slightly higher transmittance across all configurations. For instance, at 1 cm, the white light source achieves a transmittance of 0.11% with a single fiber, whereas the red LED reaches 0.08%. Similarly, with 16 fibers, the white light source attains 0.23%, while the maximum transmittance for the LED sources is limited to around 0.1%. This small difference in the measured transmittances between the LED white light bulb and RGB LED sources can be attributed to the light source directionality, which is different. In fact, the LED sources include a small collimating lens that helps create a more directional incident light source, compared to the LED bulb. Moreover, the higher optical power of the white LED (6W vs. 3W) likely improves the signal-to-noise ratio, while its broad spectral distribution ensures better overlap with the spectral responsivity of the S142C integrating sphere detector. Hence, the choice of the types of light sources used in LTC transmission assessments is another way to better model artificial and natural lighting conditions.

A quantitative analysis of the light sources confirms that wavelength-dependent effects are negligible at the scale of the specimens used in this study. Using the fiber attenuation data (200 dB/km at 650 nm), the calculated intrinsic loss through a 5 cm specimen is less than 0.2 %, ensuring that spectral filtering by the fiber does not significantly affect the measured transmittance (Hai, Quang, & Nam, 2025; Lian & Yin, 2022). Additionally, since the numerical aperture of PMMA fibers varies minimally across the visible spectrum, the beam divergence angle (θ) remains effectively constant. Consequently, the practical estimation model, parameterized using white light, remains applicable to the LED RGB sources, since the geometric propagation of light is the dominant factor that determines the power detected as a function of distances.

2.3.2 Optimal detection distance and model validation

The experimental validation was performed by directly comparing the normalized experimental data with the theoretical predictions (Figure 2.10). Specifically, the model integrates the optical intensity of the overlapping super-Gaussian beams over the 12 mm circular area of the photodetector, as defined in Equations (2.3-2.4). By explicitly matching the detector aperture in the mathematical formulation, the model enables a direct spatial correspondence between the simulated and measured detected power at each discrete detector-sample distance z. The simulations assumed an input optical power of 1 mW (at 550 nm wavelength) injected into each N optical fibers. The selected wavelength of 550 nm, located in the green region, serves as an average value within the visible spectrum (roughly between 400-700 nm), and was chosen to align the theoretical predictions with the broad-spectrum measurements performed using the experimental light sources. The model also incorporates parameters such as the *NA* of the optical fiber and super-Gaussian parameter $n = 3$, both of which inform light propagation through the fiber network (Su et al., 2020; Su, Zhang, Liu, et al., 2022; Su, Zhang, Luo, et al., 2022).

The detected light power at distances from $z = 0$ to 20 cm (relative to the sample's center) was thus simulated for the different sample configurations with $N = 1, 4, 9$ and 16 fibers. Figure 2.10 presents the detected power in the model simulations (solid curves) with the experimentally measured power (red markers). To facilitate comparison, both results were unit-normalized to ensure they are presented on the same scale.

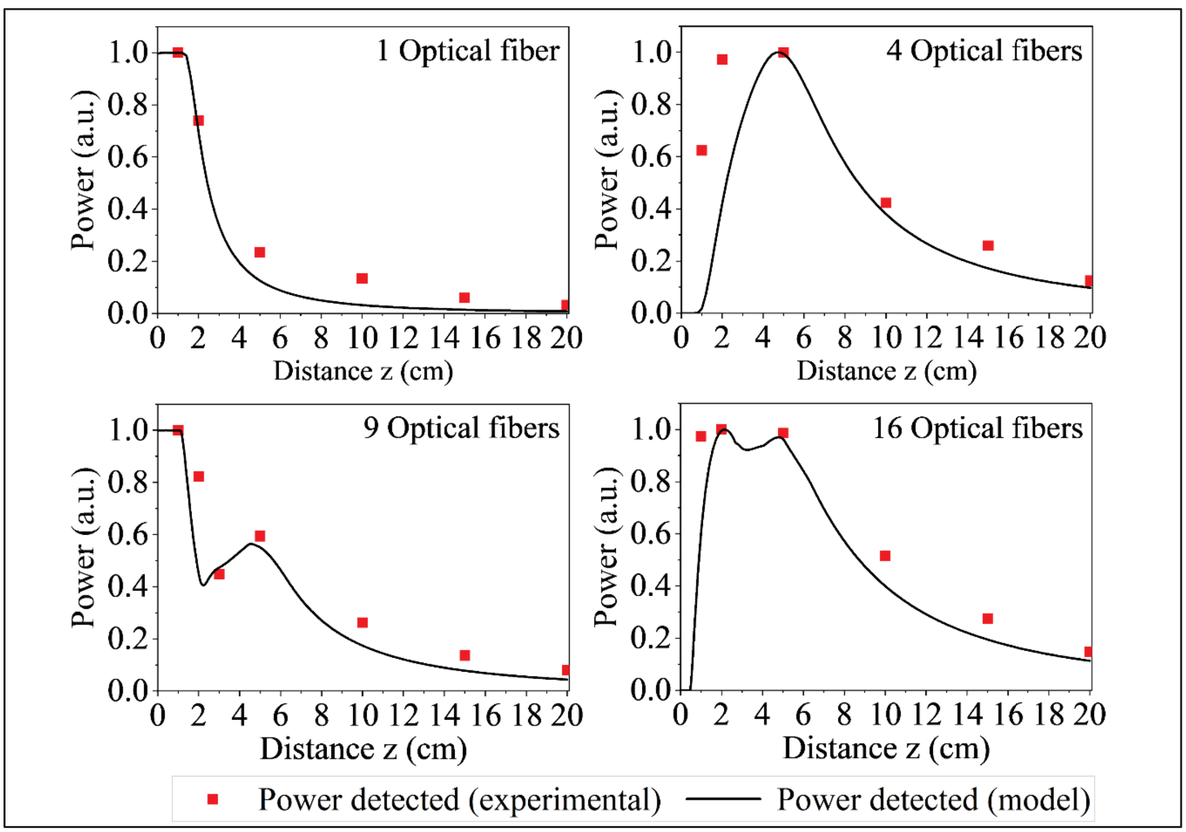

Figure 2.10 Comparison of detected power versus detector distance z between experimental measurements and theoretical model predictions for all fiber configurations (N = 1, 4, 9, 16)

As shown in Figure 2.10, both experimental and theoretical model curves of power detection exhibit similar behaviors, indicating the model's effectiveness in accurately describing the experimental conditions of light transmission in fiber-based LTC samples. As suggested earlier, for the 1-fiber configuration there is no obvious optimal detection distance. Because there is only one fiber that is centrally positioned and aligned with the detector, the detected power simply falls off with the distance. Here, a practical issue would be not to place the detector too close to the sample so as to not saturate the photodetection signal.

For the 4-fiber configuration, the detection profile shows a different behavior. At very short distances ($z = 0$), the model predicts no detectable power, as expected, since there is no fiber in the center of the sample in this configuration. Yet, experimental data indicated a small detectable power at a short $z = 1$ cm distance, which is likely due to factors such as noise, calibration errors or potential light leakage in the setup. Notably, the model's prediction of peak power detection occurring around 5 cm is validated by the experimental data.

For the 9-fiber configuration, the detected power exhibits a more complex profile due to the geometric distribution of the fibers. At short distances ($0 \leq z \leq 1\ cm$), the detected signal is dominated by the central fiber, while at larger distances the contribution from the surrounding fibers becomes increasingly significant. This transition results in a non-monotonic detection profile, with an initial high detected power, followed by a decrease and a subsequent secondary increase at larger z values. Due to this more complex behavior associated with fiber geometry, an additional experimental measurement point at $z = 3$ cm was included in the analysis, allowing a more accurate characterization of the transition region between central-fiber dominance and collective multi-fiber detection. Despite the increased complexity, both the model and experimental data indicate a consistent optimal detection distance close to $z \approx 5$ cm.

For the 16-fiber configuration, the model predicts two distinct peaks in the power detection profile. The first peak, around 2 cm, is ascribed to the power contribution of the 4 innermost fibers (see the $z = 1$ cm sub-figure in Figure 2.8). This is followed by a small "valley" in detected power in the $2 \leq z \leq 4\ cm$ region as the detector moves away from the innermost fibers. A second detection peak appears at z = 5 cm owing to the additional intensity contribution of the 12 outermost fibers to the total detected power (see the z = 5 cm sub-figure in Figure 2.8). Hence the detector location at z = 5 cm enables to "sample" the light cones emitted by all 16 fibers of this configuration. This presence of the secondary peak is validated by the experimental data.

Furthermore, both experimental data and the model show stabilization in optical power detection at larger distances (z >14 cm) as well as the exponential decay. This stability indicates that the system reaches a limit in its detection capacity beyond this point, as further increases in distance do not result in significant detected power (Robles et al., 2020; Rong et al., 2023; Tuaum et al., 2018).

2.3.3 Practical estimation of optimal sample-detector distance

The comparison between experimental results and the model's predictions (Figure 2.10) provides valuable insights. While existing studies have empirically analyzed the influence of fiber arrangement and detector distance for various configurations of fibers and LTC samples (Yue Li, Li, & Guo, 2015; Robles et al., 2020; Rong et al., 2023; Tuaum et al., 2018), as far as we know, there is no general rule available to researchers on the optimal location of a small photodetector with respect to the LTC sample in order to obtain a reliable assessment of light transmittance via optical power measurements. In this regard, we propose a simple estimation method to determine such an optimal sample-detector distance.

This estimation provides a practical tool for experimental planning, allowing researchers to determine the most effective setup for power detection, which takes into account the dimensions of the LTC sample under study and the NA of the optical fibers embedded in the sample. The NA is related to how wide light spreads as it exits the fiber, $NA = \sin(\theta)$, where θ is the half-angle of the emitted light cone (Su, Zhang, Liu, et al., 2022).

The optimal detection distance, z_{opt}, can be practically estimated based on the characteristic dimension of the sample, D_s, which represents the largest dimension of the LTC sample. For square samples, as in the current work, D_s corresponds to the side length. For non-square samples, D_s should be taken as the longest side facing the detector, as this dimension most significantly influences light transmission from the *N* fibers that are assumed to be uniformly distributed throughout the entire output surface of the sample. Figure 2.3 illustrates the light cones emitted by two optical fibers and their overlapping intensity distributions. Considering the extreme situation where two such light-emitting fibers, located at the opposite ends on the outer periphery of the sample (i.e., therefore spaced apart by approximately D_s), the optimal detection distance should correspond to the $z = z_{opt}$ value at which their intensity distributions begin to overlap at the detector's location. This geometric criterion is met when the radius of the expanding cone R, defined by $r = z \times \tan(\theta)$, is equal to half of the characteristic sample dimension ($D_s/2$). Based on the considerations shown in Figure 2.3, a simple estimation of z_{opt} can thus be derived as Equation (2.5), where the small-angle approximation was used for the definition of the fiber's $NA = \sin\theta \propto \tan\theta$.

$$z_{opt} \propto \frac{D_S/2}{\tan\theta} \approx \frac{D_S}{2 \cdot NA} \tag{2.5}$$

The estimation in Equation (2.5) reflects a geometric overlap criterion. Changes in fiber diameter affect signal amplitude, whereas the optimal distance occurs from the *NA* and the sample geometry. For the experimental setup of this study, the sample size is D_s = 5 cm and the fiber *NA* = 0.5, such that the estimated optimal distance (using Equation (2.5)) to place the detector away from the center of the sample is z_{opt} = 5 cm. This estimation value, obtained for the specific LTC sample dimensions and PMMA fibers used in this experiment agrees with the trends presented in Figs. 9 & 10, and aligns well with empirical findings reported in the broader literature, where detector placement has historically been determined experimentally rather than analytically.

For instance, Rong et al., (2023) investigated light transmittance in LTC panels (30 × 40 × 7.5 cm^3) using 2 mm diameter PMMA optical fibers arranged in 5 × 5 and 6 × 6 grid configurations

(300 and 432 fibers, respectively). In their experimental configuration, the optimal light intensity occurred with the light source at 20 cm, and the detector was placed between 30-40 cm from the sample. Given the use of PMMA optical fibers, the *NA* can be reasonably assumed to be close to 0.5. Consequently, the reported optimal detection distance range aligns with the trend predicted by the practical estimation model (Equation (2.5)) proposed in this work. Using a comparable setup, Nam et al., (2022) studied light transmittance in $10 \times 10 \times 5$ cm³ rectangular LTC samples, using polymer optical fibers with diameters of 0.75, 1.0, and 1.5 mm at various spacings. The highest light transmittance was measured at 10 cm, with intensity decreasing as the distance increased (20-30 cm). While the *NA* of the fibers was not provided, the use of PMMA fibers suggests a numerical aperture similar to that adopted in the present study. Under this condition, the optimal detection distance of 10 cm, would be in agreement with the definition of the estimated optimal distance proposed in this study.

Additionally, Li, Li, & Guo, (2015) investigated light transmittance through LTC samples with dimensions of $4 \times 8 \times 1$ cm³, containing PMMA optical fibers of 0.5 and 1 mm in diameter. Their results showed a decrease in detected power as the distance between the detector and the sample increased, from 10 cm to 40 cm. Assuming a comparable *NA* of 0.5 associated with PMMA fibers, our model predicts an optimal detection distance of 8 cm for their sample dimensions. Although their measurements began at 10 cm, the observed trend of decreasing transmittance with increasing distance aligns with the general behavior predicted by the model presented in this study. A similar pattern is evident in the work of Tuaum et al., (2018), who studied 10 cm cubic specimens. They measured intensity using a light-dependent resistor (LDR) at distances ranging from 10 to 50 cm and noted a progressive decrease in intensity following the general distance-dependent trend predicted by our model. Our model suggests an optimal distance closer to 5 cm for this configuration. Thus, the monotonic decrease observed from 10 cm onwards is consistent with a peak intensity located at a shorter distance than their starting measurement point.

Additionally, Chiew et al., (2022) investigated light transmittance in cubic specimens of 10 cm, using optical fibers with a diameter of 1 mm and an *NA* of 0.51, arranged with 25 mm spacing. Light transmittance was measured at a detection distance of 10 cm. Despite not focusing on testing different detection distances, the 10 cm measurement aligns closely with the optimal distance predicted by the proposed practical estimation model presented in this study for similar sized samples. Finally, Tahwia et al., (2021) evaluated translucent self-compacting concrete specimens (10 × 10 × 10 cm^3) with 1 and 2 mm PMMA fibers, measuring at distances from 0 to 40 cm. Although transmittance decreased with distance, values at 10 cm were very close to those at zero distance and significantly higher than at larger distances. This observation further validates the present simplified model, which identifies the 5–10 cm range as the optimal region for stable transmission measurements in samples of this geometry.

Figure 2.11 summarizes detector-sample distances reported in the literature alongside the optimal distance estimated and experimentally validated in this study. A linear relationship is observed between sample size, ranging from 4 × 8 cm^2 to 30 × 40 cm^2, and the optimal detector distance across fiber diameters from 0.5 to 3 mm. This behavior is expected since most commercial PMMA fibers exhibit similar numerical apertures (~0.5), leading to comparable beam divergence independently of core diameter. These studies did not aim to determine an optimal detector-sample distance, and measurements were generally performed at fixed or limited distances based on their experimental setups. For instance, the value plotted for Rong et al., (2023) represents the midpoint of their reported 30-40 cm optimal distance range. The reported values are therefore presented here for comparative trend analysis rather than as claimed optima. Despite variations in sample dimensions, fiber diameters, and experimental setups, the reported distances fall within or close to the range predicted by the proposed estimation model.

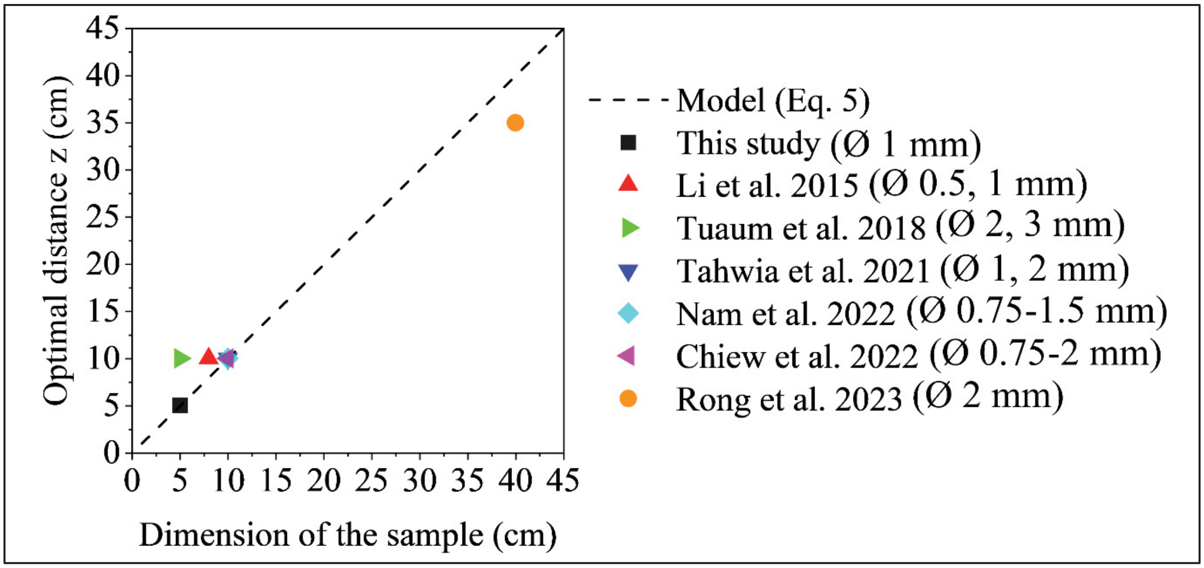

Figure 2.11 Comparison between the optimal detector-sample distance predicted by the practical estimation model (dashed line) and literature-reported detector-sample distances for PMMA-based light-transmitting concrete (symbols), for specimen dimensions from 4 × 8 cm² to 30 × 40 cm² and fiber diameters between 0.5 and 3 mm

Despite the range of fiber diameters considered in the literature, the scaling of the optimal detector distance with sample size remains consistent, indicating that the optimal distance is controlled by angular spreading rather than by the emitting core size. While this estimation offers a simplified and practical guideline, the theoretical model (Equations (2.3-2.4)) developed in this study provides a physically grounded framework for performing a detailed analysis and optimization of light transmission measurements in fiber-based LTC samples, incorporating the specific influence of sample geometry and fiber characteristics.

2.4 Conclusions

This study examined light transmission in light-transmitting concrete using an experimental framework combined with a super-Gaussian description of the emitted light field. The work evaluated the influence of fiber quantity, detector-sample distance, and light source type on measured transmittance. A simplified estimation model based on sample dimensions and fiber numerical aperture was also proposed and validated. The model reliably predicted the detected power trends observed experimentally. The key findings are:

- Fiber quantity: Higher numbers of embedded fibers improved light transmittance by broadening and homogenizing the intensity distribution. Configurations with 16 fibers consistently showed the highest transmittance.
- When expressed relative to the characteristic sample dimension Ds, the detector-sample distance z defines distinct transmittance regimes. Short distances, between 0.2 Ds and 0.4 Ds, favor the detection of centrally aligned fibers. Intermediate distances, on the order of Ds, promote overlap of the emitted light cones and result in maximum transmittance across all configurations. At larger distances, greater than approximately 1.5 Ds, attenuation and beam dispersion dominate, with a stabilization trend observed for distances exceeding 2 Ds.
- Light source: For this experiment, the white light produced slightly higher transmittance at short distances compared to RGB LEDs, while differences diminished at longer distances.
- Model validation: Both the super-Gaussian framework and the practical (simplified) estimation model accurately predicted experimental trends and optimal detector placement.

The proposed estimation approach and theoretical model, while developed for 1 mm PMMA fibers, apply to other fiber diameters and materials, as they primarily depend on the fiber numerical aperture. This study establishes a standardized measurement protocol for LTC optical characterization, enabling reproducible evaluation of fiber-based cementitious composites. Future work may extend the framework to larger experimental datasets, alternative fiber materials, and optically active or smart cement-based applications.

CHAPTER 3

MECHANICAL STRENGTHENING OF CEMENTITIOUS COMPOSITES BY OPTICAL FIBERS THROUGH ADHESION AND GEOMETRIC DISRUPTION?

Karina Hwang Arcolezi [a, b], Victor Brial [a], Bora Ung [b], Claudiane Ouellet-Plamondon [a]

[a] Department of Construction Engineering, École de technologie supérieure,
1100 Notre-Dame Ouest, Montréal, Québec, Canada H3C1K3
[b] Department of Electrical Engineering, École de technologie supérieure,
1100 Notre-Dame Ouest, Montréal, Québec, Canada H3C1K3

Article submitted for publication, April 2026

Abstract

This study experimentally isolates the mechanical effects of embedded plastic optical fibers in cementitious composites, separating fiber-matrix interaction from geometric disruption by comparing fibers directly with equivalent-geometry holes. Optical fiber samples were tested alongside preformed holes of equivalent geometry in two mortar formulations, a reference mixture (CSA A3000 Class N) and a low-cement LC^3-inspired eco mixture. In compression, fibers outperformed equivalent holes at moderate inclusion counts, with a 5.5 MPa gap at nine inclusions in the reference mixture, confirming that fiber-matrix adhesion contributes independently of geometry. In the eco mixture, fibers still yielded consistent gains at 4-9 inclusions while higher hole counts reduced strength below the control, showing that geometric disruption dominates when bonding is weak. In flexure, orientation dominated over inclusion type, as longitudinal inclusions improved strength by up to 17% while transversal ones reduced it at higher counts, regardless of inclusion nature. Scanning electron microscopy linked the weaker response of the eco mixture to differential shrinkage and reduced C-S-H density, yet functional inclusions still provided consistent compressive strength gains of up to 12% over the control, supporting the viability of reduced-cement matrices for multifunctional applications. These results demonstrate that the relative contribution of material versus geometry is loading-mode dependent, and that matrix quality determines which mechanism dominates.

3.1 Introduction

Cement-based composites such as mortar and concrete are widely employed in modern construction, combining high mechanical performance with durability and versatility in both structural and architectural applications (Gagg, 2014). In recent years, the growing demand for multifunctional building materials has led to research efforts toward integrating non-conventional properties into cementitious systems, including light transmission, self-sensing, and structural health monitoring capabilities (Dutta, Reeti, & Mandal, 2018; Makul, 2020; Mukherjee, Deepmala, Srivastava, & Sandhu, 2023; Qiao et al., 2023; Urmila, Abhijeet, & Ranveer, 2015; Zhang, Long, Broere, & Bao, 2025). Within this context, the incorporation of optical fibers into cementitious composites has emerged as a promising strategy to introduce additional functionalities (Bado & Casas, 2021; Bai et al., 2024; Bremer et al., 2016; Zhou, Ou, Hang, Chen, & Ou, 2009). Light-transmitting cementitious materials, for instance, utilize embedded optical fibers to enable partial transmission of natural or artificial light through otherwise opaque elements, supporting both aesthetic and energy-efficient design goals (Bai et al., 2024; Shenoy et al., 2023; Su et al., 2023, 2020; Su, Zhang, Luo, & Liu, 2022; Sahana et al., 2023). Separately, optical fibers have also been investigated as sensors capable of detecting strain, temperature, or cracking, contributing to the development of smart infrastructure (Leung et al., 2015; Merzbacher et al., 1996; Qiao et al., 2023; Taheri, 2019). Both applications rely on different fiber types, configurations, and embedding strategies.

Beyond their functional purpose, optical fibers embedded in mortar or concrete can also influence mechanical performance (Huynh Phuong Nam et al., 2022; Yue Li, Li, Wan, et al., 2015; Q. Lyu et al., 2024; Nam et al., 2024; Tahwia et al., 2022). Although they are not intended to act as structural reinforcements, their presence may locally disturb the matrix, altering stress distribution or triggering microcracking. Previous studies have reported changes in compressive and flexural strength associated with factors such as fiber content (Henriques et al., 2018, 2020; Yue Li, Li, Wan, et al., 2015; Nam et al., 2024), orientation (Huynh Phuong Nam et al., 2022), diameter (Bai et al., 2024; Emanet & Arda Buyuktaskin, 2023; Yue Li, Li, Wan, et al., 2015; Nam et al., 2024; Robles, Arenas, & Stefani, 2020), and material type (Edris, Odah, Abu-Qasmieh, & Hendy, 2021; Subathra & Sangeetha, 2020). These effects are often linked to local discontinuities, poor fiber-matrix bonding, or increased hole formation, especially in cases with high fiber content or limited workability (Henriques et al., 2018).

Despite these observations, several questions remain unresolved. Most existing studies focus either on maximizing light transmission or on exploring sensing capabilities, with relatively limited emphasis on systematically evaluating mechanical implications. In particular, it remains unclear whether strength variations arise predominantly from the physical material of the embedded fibers or from the geometric disruption they introduce. Direct experimental comparisons with non-functional holes of equivalent geometry are scarce, which limits the ability to decouple the material and geometric contributions to strength changes (Štochl et al., 2023). Holes of controlled geometry can be used to reduce density and material consumption, enabling lighter or more sustainable cement-based elements while maintaining adequate performance.

To address these gaps, this study investigates the mechanical performance of mortar samples containing embedded translucent optical fibers, compared directly to samples with preformed holes of identical diameter and spatial distribution. This experimental design was chosen to distinguish two competing sources of mechanical influence: the material interaction between the fiber and the surrounding matrix, and the purely geometric effect of introducing a cylindrical discontinuity into the cementitious composite. If fibers and holes of equivalent geometry produce identical mechanical outcomes, then geometry alone controls the response. If fibers consistently outperform holes, then fiber-matrix bonding and stress transfer across the interface contribute independently to strength.

The experimental investigation explores different inclusion quantities and orientations embedded in two mortar compositions. The reference formulation is classified as Class N in CSA A3000 (CSA, 2018), with Portland cement accounting for 60% of the binder. The eco mixture follows the LC^3 binder-inspired concept, replacing a portion of Portland cement with metakaolin and limestone filler to reduce clinker content by approximately 50% while maintaining comparable workability and binder proportion. This contrast was chosen to assess whether sustainable, reduced-cement matrices remain mechanically compatible with embedded functional elements. Compressive and flexural strength tests were conducted following standardized ASTM procedures. Complementary finite element simulations were carried out to compare the elastic stress distributions generated around the investigated inclusions, and scanning electron microscopy (SEM) was used to characterize microstructural features such as fiber-matrix contact and hole boundaries. The research questions guiding this study are:

(i) How do embedded optical fibers and similarly sized holes affect compressive and flexural strength, depending on inclusion quantity and orientation?
(ii) Are mechanical effects primarily governed by the material nature of the inclusions or by their geometrical distribution, and does this hierarchy depend on the loading mode?
(iii) How does the matrix composition influence mechanical sensitivity to such embedded elements?

The main objectives are to quantify the mechanical effects of optical fibers and holes across different inclusion configurations, to determine whether observed strength changes are predominantly material- or geometry-driven, and to examine whether matrix formulation alters the interaction between inclusions and the surrounding composite. Together, these investigations examine how embedded functional elements interact with the cementitious matrix in different loading modes and matrix compositions, an increasingly relevant issue as the construction industry develops multifunctional, low-carbon materials that combine light transmission, sensing, or aesthetic features with adequate structural performance.

3.2 Materials and methods

3.2.1 Materials

The mortars were produced using general-use Portland cement (compressive strength of 37.8 MPa at 28 days), compliant with CSA A3000-18, metakaolin, and limestone filler. Metakaolin was classified as a Class N natural pozzolan under CSA A3000 and ASTM C618 (ASTM C618-25, 2025). Natural sand with a maximum particle size of 2.5 mm was employed as an aggregate, and a polycarboxylate-based superplasticizer was added to improve workability.

Two mixtures proportions were prepared to assess the influence of binder composition on mechanical performance (Table 3.1). The reference mixture followed CSA A3000-18 standards, with Portland cement accounting for 60% of the binder. The eco mixture, inspired by the Limestone Calcined Clay Cement (LC^3) mixture, incorporated a higher fraction of limestone filler and metakaolin, reducing Portland cement content while keeping the overall binder proportion constant (Arcolezi, et al, 2024; Jin et al, 2025). This approach enabled a direct comparison between conventional and reduced-cement formulations in order to evaluate their mechanical response under different inclusion conditions, such as mortars with embedded optical fibers, preformed holes, or without any inclusion (control sample). The composition of the binder materials is summarized in Table 3.2.

Table 3.1 Composition and properties of mortar mixtures

Material	**ID**	**Reference mixture (kg/m³)**	**Eco mixture (kg/m³)**
Ordinary Portland cement	OPC	390	200
Metakaolin	MK	162.5	150
Limestone filler	LF	97.5	300
Sand	Sa	1310	1310
Water	W	255	255
Superplasticizer	SP	7	7
Density (g/cm³)	-	2.23	2.22
Flow (%)	-	144	146

Table 3.2 Chemical composition of the binder materials (m%)

	SiO_2	**Al_2O_3**	**Fe_2O_3**	**CaO**	**MgO**	**SO_3**	**TiO_2**	**Na_2O**	**K_2O**	**LOI***
OPC	19.1	4.8	3.6	60.2	2.6	3.8	0	0.92	0	1.9
MK	62.5	31	1.1	0.4	0.3	0	0.6	0.16	1.8	0.9
LF	2.2	0.4	0.1	53.6	0.5	0.1	0.01	0.02	0.1	42.9

* Loss of ignition

The selection of these two mixtures proportion were motivated by three complementary objectives. First, the LC^3-inspired binder concept underlying the eco mixture represents a well-documented and industrially scalable strategy for reducing cement-related carbon emissions, achieved by replacing a portion of Portland cement with calcined clay and limestone filler at a constant water-to-binder ratio (Arcolezi et al., 2024; Jin et al., 2025). Second, the metakaolin used in this study, classified as a Class N pozzolan (ASTM C618) with a combined SiO_2 + Al_2O_3 content of 93.5% and a fine particle size distribution (40.1% below 2 μm, 99.98% passing 45 μm), is expected to provide pozzolanic reactivity that partially compensates for the reduced clinker content, enabling meaningful strength development despite the lower cement proportion (Scrivener, John, & Gartner, 2018; Scrivener, Martirena, Bishnoi, & Maity, 2018). Third, maintaining identical aggregate content, water-to-binder ratio (0.39), and superplasticizer dosage across both mixtures ensure that any differences in mechanical response to embedded inclusions are attributable to binder composition rather than mixture proportioning (Benezet & Benhassaine, 1999; Scrivener et al., 2018). This controlled comparison evaluates whether reduced-cement matrices remain mechanically compatible with embedded functional elements such as optical fibers.

Limestone filler (LF) content differs substantially between the two mixtures, increasing from 97.5 kg/m³ in the reference mixture to 300 kg/m³ in the eco mixture. It is predominantly inert, as indicated by its high CaO content (53.6%) and loss of ignition (42.9%, Table 3.2). LF contributes to improved particle packing, workability, and early strength by providing nucleation sites for cement hydration, while reducing compaction energy requirements and lowering both cost and environmental impact (John, Matschei, & Stephan, 2018; Scrivener et al., 2018; Scrivener et al., 2018a). The comparable flow values of both mixes (144% and 146%) reflect this contribution, demonstrating that a higher LF dosage can compensate for reduced clinker content without compromising fresh state performance.

Polymethyl methacrylate (PMMA) optical fibers (Mitsubishi Chemical Eska™) with 1 mm diameter and tensile strength of 83 MPa were embedded in the mortar to evaluate their effect on mechanical performance. To separate geometry-dependent effects from material interactions, preformed holes of identical diameter and geometrical distribution were created using stainless steel bend-and-stay wires of 1 mm diameter (that were removed at the demolding step). Control samples without inclusions (i.e., no holes or fibers) were also produced for reference.

3.2.2 Mortar mixtures and sample preparation

Mortar samples were cast in steel molds pre-drilled to accommodate either optical fibers or the wires used to generate preformed holes. Mixing was carried out in a mechanical mixer following ASTM C305 (ASTM C305-14, 2014), with a water-to-binder ratio of 0.39. For compressive strength tests, cubic samples measuring 50 × 50 × 50 mm were molded in two layers, each compacted 32 times with a rubber rod, in accordance with ASTM C109 (ASTM, 2021). For flexural strength tests, prismatic samples of 40 × 40 × 160 mm were prepared following ASTM C348 (ASTM, 2016).

For fiber-embedded samples, the optical fibers were positioned in the mold openings prior to casting and remained fixed throughout the process. For the hole samples, stainless steel bend-and-stay wires coated with a release agent were placed in the molds before casting and carefully removed during demolding, 24 h after casting, thereby leaving cylindrical holes similar in geometry to the fibers. After demolding, all samples were cured in a controlled chamber at 23 ± 2 °C and relative humidity above 95% for 28 days. Three samples were produced and tested for each condition.

The workability of the fresh mortar was evaluated by a flow table test, performed 2 minutes after mixing in accordance with ASTM C1437 (ASTM, 2020). The mortar was placed into a truncated cone mold in two layers, each compacted 20 times with a rubber rod. After lifting the mold, the flow table dropped 25 times within 15 s at a steady pace. The spread diameter was measured along four predefined perpendicular axes using a caliper, and the four values were averaged to obtain a mean spread diameter. A flow value of 0% indicates that the mortar did not spread beyond the cone base after lifting and dropping the table, while the upper bound of 152% observed in the present study corresponds to a mean spread diameter of approximately 252 mm, reflecting a highly fluid mortar facilitated by the polycarboxylate-based superplasticizer. Both mixtures achieved flow values within this range (144% and 146%), confirming adequate and comparable workability across formulations.

In total, 132 samples were produced, covering the two mortar formulations (reference and eco mixture), the three inclusion conditions (optical fibers, preformed holes, and controls), and the two mechanical tests (compressive and flexural strength). For flexural testing, inclusions were oriented either longitudinally, along the 160 mm axis of the prism, or transversely, along the 40 mm side. Compression tests, however, were performed only on cubic samples, without orientation distinction.

A consistent labeling scheme was adopted for identification. “Control” designates samples without inclusions. Samples containing fibers or holes were labeled “XY,” where “X” denotes the number of inclusions and “Y” the type: “F” for optical fiber and “V” for hole. For example, “4F” refers to four optical fibers, while “9V” refers to nine holes. The inclusions were distributed according to a checkerboard pattern, ensuring uniform spacing and systematic alignment in both horizontal and vertical directions. This layout facilitated controlled comparisons of how the number and orientation of inclusions affected the mechanical response of the mortar.

3.2.3 Mechanical properties analysis

3.2.3.1 Compressive strength

Compressive strength tests were carried out on mortar samples prepared in three configurations: (i) control samples without inclusions; (ii) samples containing embedded optical fibers in varying quantities; and (iii) samples with preformed holes. To investigate the effect of the inclusion quantity, samples were produced with 1, 4, 9, and 16 fibers or holes. The inclusions were arranged according to a uniform grid across the cross-section of the cubic samples, ensuring an even spatial distribution within the matrix.

Figure 3.1 illustrates the sample configurations used in the compressive strength tests. Panel (a) shows the grid distribution of inclusions, while panels (b) and (c) present representative samples containing optical fibers and preformed holes, respectively. The photograph was taken immediately after the samples were surface-dried in accordance with ASTM C109. Residual moisture retention is visible around the preformed hole regions, likely caused by water being locally trapped in these areas.

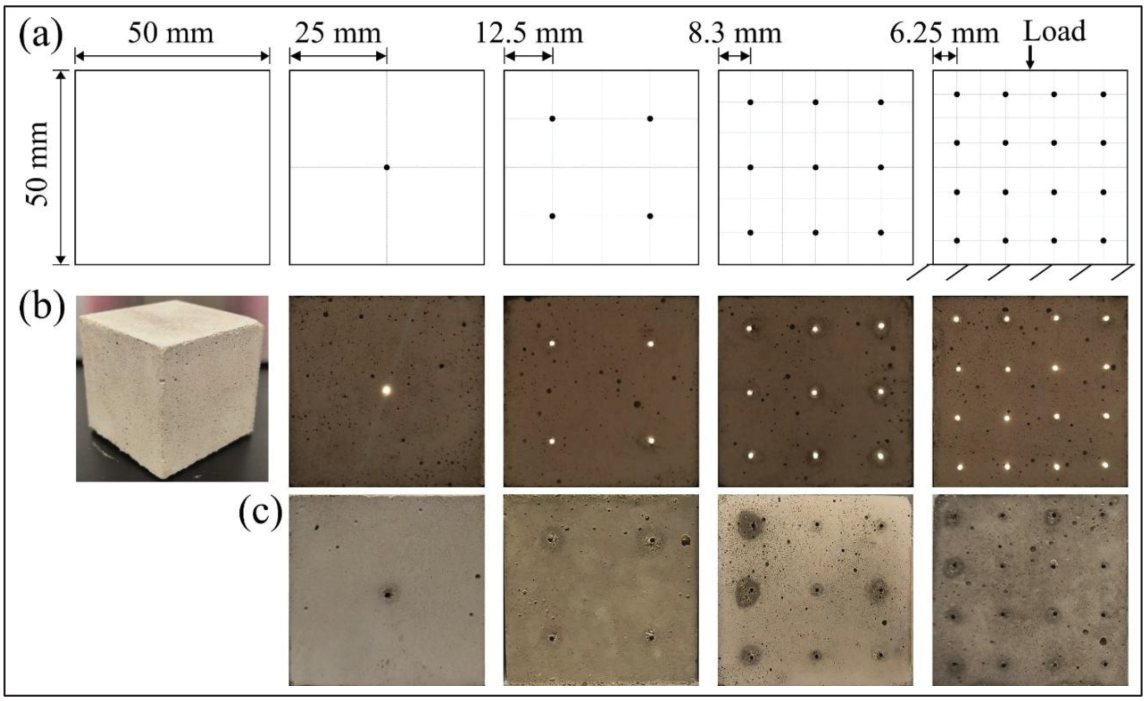

Figure 3.1 Configuration of mortar samples used in compression tests: (a) distribution of inclusions, (b) control and samples with embedded optical fibers, and (c) samples with preformed holes

3.2.3.2 Flexural strength

Flexural strength tests were carried out on mortar prisms (40 × 40 × 160 mm) using the same three sample groups as in compression (control, optical fibers, and preformed holes). In this case, however, two distinct orientations of the inclusions were considered: longitudinal and transverse. In the longitudinal arrangement (Figure 3.2a), fibers or holes were aligned with the 160 mm axis of the sample, while in the transverse arrangement (Figure 3.2b), inclusions were oriented perpendicular to this axis. For easier comparison between the two configurations, the transverse layout was designed by dividing the 160 × 40 mm face of the prism into four quadrants of 40 mm each, thus mirroring the spacing adopted in the longitudinal arrangement. The number of inclusions was then distributed per quadrant, meaning that one, four, or nine inclusions corresponded to one, four, or nine per conceptual quadrant, respectively, ensuring geometric consistency between orientations.

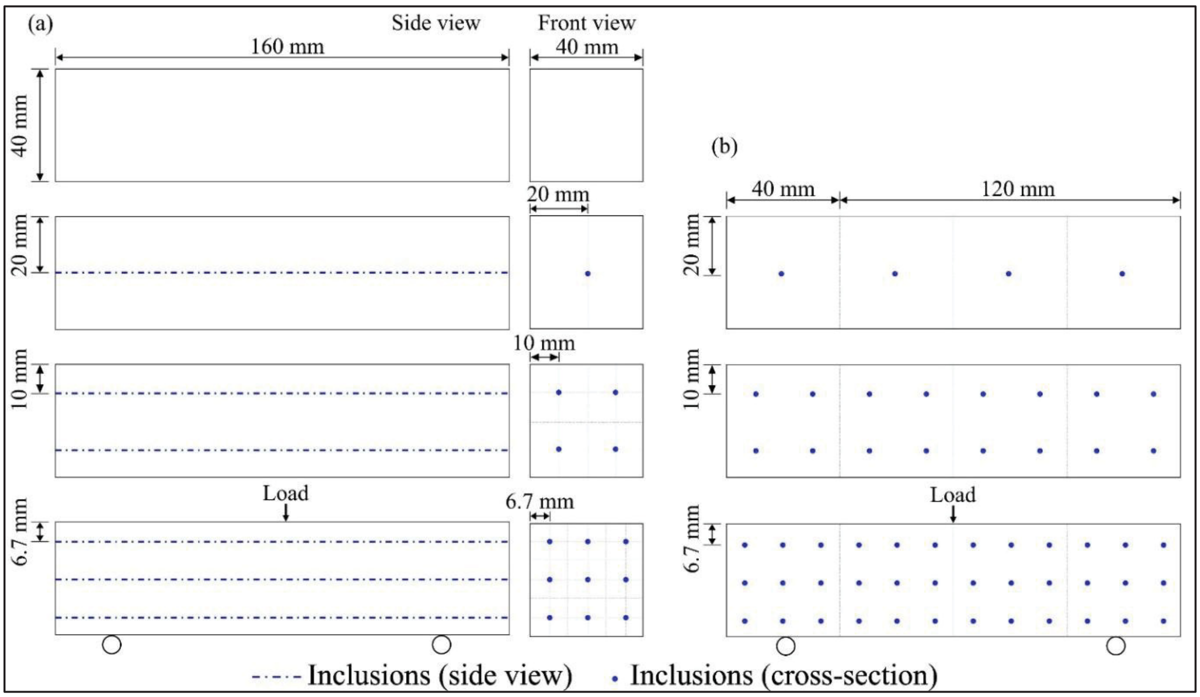

Figure 3.2 Optical fiber/holes distribution in flexural strength test samples: (a) longitudinal and (b) transversal directions. The side view and cross-sections of the inclusions are identified in blue

3.2.4 Scanning electron microscopy

To evaluate the microstructural characteristics of inclusions, scanning electron microscopy (SEM) was performed on selected mortar samples. Four representative prisms were chosen: 9V and 9F from the reference mixture, 4V, and 9F from the eco mixture. After one year of curing, small sections were cut from the central part of the prisms to limit surface carbonation and drying effects. Specimens were first sawn to approximately 5 mm thickness using a precision diamond saw under continuous lubrication to minimize microcracking. The slices were immediately rinsed with isopropanol to halt hydration and then immersed in fresh isopropanol for 72 h, following the solvent-exchange protocol recommended for cementitious materials. After solvent treatment, the samples were vacuum dried and impregnated with a low-viscosity epoxy resin to preserve pore structure and stabilize the interfaces around inclusions. The impregnated sections were successively ground with 600-grit SiC paper and polished with diamond pastes of 9 µm, 3 µm, 1 µm, and 0.5 µm particle sizes, using lapping oil as a lubricant. After each polishing step, the specimens were cleaned in an ultrasonic bath with isopropanol for 15 min to remove residues and cross-contamination between polishing stages.

For SEM observation, samples were carbon-coated to ensure conductivity. Imaging was conducted using a Hitachi TM3030 tabletop microscope equipped with a backscattered electron (BSE) detector. An accelerating voltage of 15 kV and magnifications between ×30 and ×400 was used to examine the geometry of holes, the morphology of fiber–matrix interfaces, and possible microcracking or porosity in the interfacial transition zones. This procedure enabled direct comparison between the morphology of holes and optical fibers embedded in the mortar matrix, with emphasis on the long-term stability of the interfaces and potential differences in microstructural damage or densification.

3.2.5 Numerical analysis

Finite element simulations were conducted in ANSYS Workbench to complement the experimental program by providing qualitative insight into the stress distribution around inclusions under both compressive and flexural loading. The numerical models reproduced the sample geometries and boundary conditions of the laboratory tests. Mortar was modeled as a linear elastic material with an elastic modulus of 22 GPa (Marques et al., 2020), Poisson’s ratio of 0.19 (Baranikumar, Torrence, & Grasley, 2021), and density of 2200 kg/m³ as per testing (Jin et al., 2025). PMMA optical fibers were assigned an elastic modulus of 3.2 GPa, Poisson's ratio of 0.35, and a density of 1118 kg/m³ as per the manufacturer's specifications. A linear elastic constitutive law was adopted for both phases.

This modelling choice defines the scope and purpose of the simulations explicitly. A linear elastic formulation reproduces the elastic stress state before any damage or cracking and is appropriate for identifying stress localization patterns and qualitative differences between inclusion types. It does not capture crack initiation, crack propagation, progressive matrix damage, or fiber-matrix debonding. Consequently, the simulations are not used to predict failure loads or ultimate strength, and their results are interpreted solely as qualitative indicators of stress redistribution mechanisms operating in the pre-failure regime.

For the compression models, a uniaxial load of 100 kN was applied in the vertical direction, while the bottom face was fully constrained (Figure 3.1a). Normal stress was analyzed to examine how inclusions modify the compressive stress field. A uniform mesh size of 2 mm was employed throughout the volume, with local refinement around each inclusion to improve the resolution of the stress gradient near fiber- and hole-matrix interfaces.

For the flexural models, three-point bending was simulated with two fixed supports positioned 25.4 mm from each end of the prism, producing a clear span of 109.2 mm. A vertical load of 1 kN was applied at midspan. The equivalent von Mises stress was computed to assess how inclusions modify stress concentrations and stress redistribution under bending. Configurations modelled in flexure included longitudinal and transversal orientations at 1, 4, and 9 inclusions, for both fibers and holes, in addition to the control.

3.2.6 Statistical analysis

Statistical analyses were conducted separately for reference and eco mixtures. Compressive strength was analyzed using one-way analysis of variance (ANOVA), since specimen configuration was the only experimental factor. This factor included the control and the fiber and hole configurations at each inclusion level. When the overall ANOVA indicated significant differences, Tukey's honestly significant difference test was applied for pairwise comparisons. The discussion focused on comparisons between fibers and geometrically equivalent holes, as well as comparisons between relevant inclusion configurations and the control, since these contrasts directly addressed the effects of the inclusion material and the departure from the control condition.

Flexural strength was analyzed using two-way ANOVA with replication. The factors were inclusion orientation, transverse or longitudinal, and inclusion configuration, comprising 1F, 4F, 9F, 1H, 4H, and 9H. The interaction between orientation and inclusion configuration was also evaluated. This model was selected because each fiber and hole configuration was tested in both orientations. Control specimens were not included in the two-way analysis because orientation was not applicable to specimens without inclusions. Statistical significance was established at $\alpha = 0.05$.

3.3 Results and discussions

3.3.1 Compressive strength

Figure 3.3 shows the compressive strength results for mortars with embedded optical fibers and preformed holes for both mortar formulations, with percentage changes relative to each respective control annotated to facilitate comparison. For the reference mixture, the control reached an average of 63 MPa. The addition of a single fiber or a single hole did not change the results significantly and remained close to that of the control samples. With four and nine fibers, compressive strength increased to 68.8 MPa and 70 MPa, respectively, representing an improvement compared to the control (both significant versus the control by one-way ANOVA with Tukey's HSD, $p < 0.05$; the difference between the four- and nine-fiber configurations was not significant). However, at sixteen fibers the average strength returned to a value statistically indistinguishable from the control (65.7 MPa; $p > 0.05$), indicating that the benefit observed at intermediate fiber levels was no longer present. This behavior aligns with a percolation-like behavior, where increasing inclusion density leads to overlapping stress transfer zones around individual fibers, and the resulting cumulative disruption of the matrix ultimately surpasses the reinforcing contribution of each added fiber. Similar reductions at higher fiber dosages have been reported in the literature, including the works of Henriques et al., (2018, 2020), Li et al., (2015), Navabi et al., (2021), Lian & Yin, (2022), and Sawant et al., (2014).

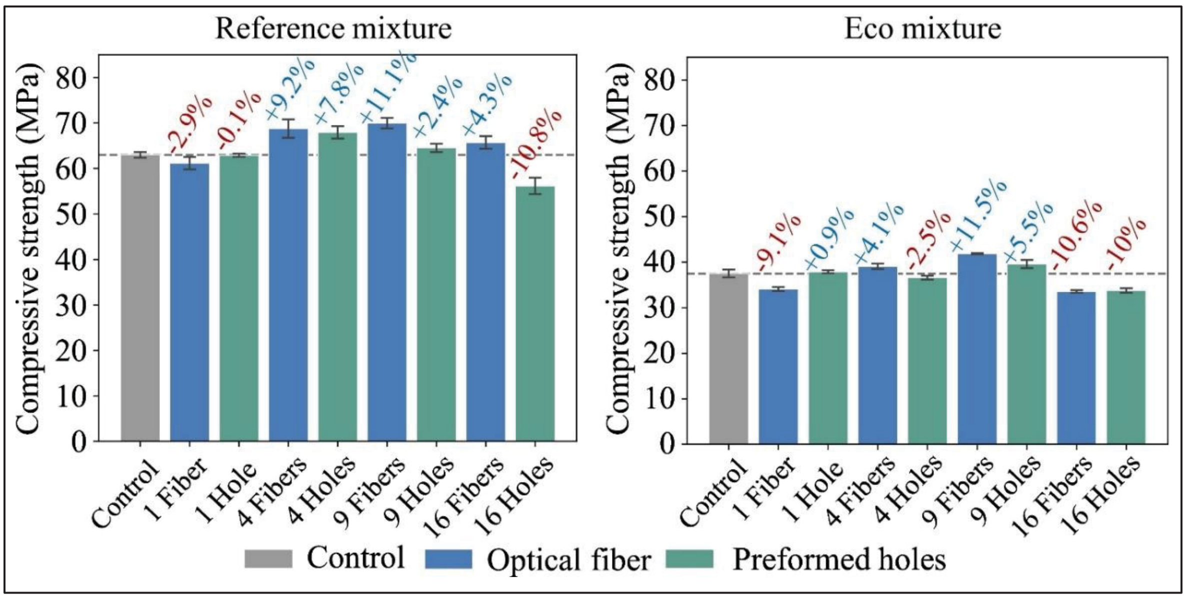

Figure 3.3 28-day compressive strength of mortars containing optical fibers and preformed holes of equivalent geometry, for (a) the reference mixture and (b) the eco mixture. Percentages indicate the change relative to each respective control (dashed line)

For hole samples in the reference mixture, the same tendency was observed up to four holes, with strength reaching 68 MPa. At higher quantities, however, strength dropped to 64.5 MPa for nine holes and 56.2 MPa for sixteen holes. At this density, holes collectively weaken a significant fraction of the load-bearing cross-section, and the matrix can no longer redistribute stress effectively around the growing network of discontinuities. This indicates that the mechanical effects of embedded fibers cannot be explained solely by their occupied space, but that their interaction with the surrounding matrix contributes positively, especially at moderate inclusion levels (Štochl et al., 2023).

The direct comparison between fiber and hole responses at equivalent geometry provides clear evidence that the material nature of the inclusion contributes independently to compressive strength, beyond the geometric disruption of the matrix. At nine inclusions in the reference mixture, fibers reached a mean compressive strength of 70 MPa, whereas holes with the same diameter and spatial distribution yielded 64.5 MPa, corresponding to a statistically significant difference of 5.5 MPa under equivalent geometric conditions ($p < 0.05$). At one inclusion, this difference was not observed (1F: 61.2 MPa; 1H: 62.9 MPa), with the two being statistically equivalent, indicating that a single inclusion does not generate sufficient load redistribution to make material-matrix interaction mechanically relevant. As the number of inclusions increases to four and nine, however, fibers establish a distributed network of stress transfer sites within the matrix, and the combined effects of fiber-matrix adhesion and elastic mismatch become measurable (the fiber-hole difference reaching significance at nine inclusions, $p < 0.05$). This progressive divergence between fiber and hole responses addresses research question (ii), demonstrating that geometric disruption alone does not explain the observed strength changes at moderate inclusion levels, and that the material-matrix interface provides an additional strengthening mechanism that scales with inclusion density.

In the eco mixture, the control sample reached 37.5 MPa, reflecting the reduced cement content. The presence of fibers showed a non-monotonic response, a slight decrease with one inclusion, progressive gains at four and nine fibers, reaching a maximum of 41.9 MPa. As also observed with reference mixture, the strength decreased when sixteen fibers were added, dropping below the control. The hole samples in this mixture followed a similar trend, with nine holes resulting in a small increase (39.6 MPa), but sixteen holes reducing strength to 33.8 MPa. In this mixture, fiber and hole strengths differed significantly at one, four, and nine inclusions ($p < 0.05$) but converged at sixteen ($p > 0.05$), where both fell significantly below the control. The absolute values in this mixture were significantly lower compared to the reference mixture, which is expected owing to the reduced cement content (Damineli, Kemeid, Aguiar, & John, 2010; Jin et al., 2025).

This close contact likely facilitated stress transfer across the interface, explaining why fiber samples consistently outperformed hole samples at equivalent inclusion levels. In contrast, the eco mixture exhibited a larger interfacial gap between the fiber and the matrix (Figure 3.4b), thereby reducing the fibers' ability to engage effectively with the surrounding mortar under loading. This gap is attributed to differential shrinkage between the PMMA fiber and the cementitious matrix. During hydration and subsequent drying, the mortar undergoes autogenous and drying shrinkage, whereas the PMMA fiber, as a solid polymer with fixed geometry, does not contract volumetrically. As the matrix shrinks around the fiber, tensile stresses develop at the interface and, once they exceed the local bond strength, debonding and gap formation occur (Shafei et al., 2021).

The local interfacial morphology observed in the eco mixture is consistent with its distinct binder composition and the distribution of hydration products around the fiber. In the selected reference-mixture image, the solid phase appears more continuous around the fiber and the visible interfacial gap is smaller (Figure 3.4a). These features are consistent with a local morphology favorable to fiber-matrix contact and stress transfer. The SEM observations therefore complement the mechanical comparison between fiber and hole specimens by providing local morphological evidence of differences in interfacial contact between the two mixtures.

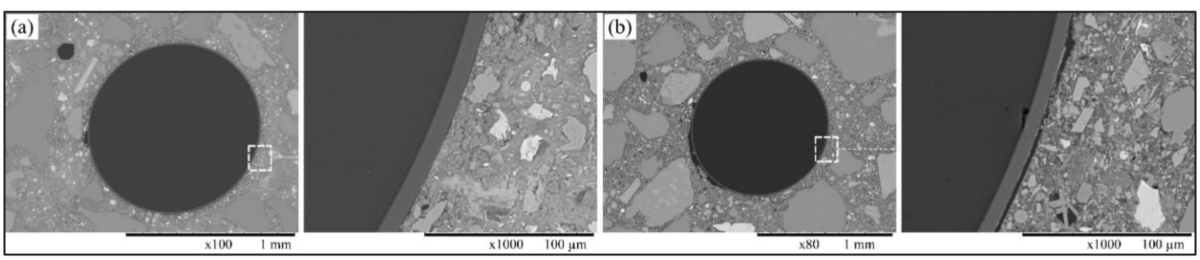

Figure 3.4 Selected backscattered-electron SEM images of the fiber-matrix interface in (a) the reference mixture and (b) the eco mixture, with corresponding higher-magnification views

The eco mixture maintained compressive strengths close to or above its control at moderate fiber contents. The 9F configuration reached 41.9 MPa, representing a statistically significant increase relative to the control. This result shows that embedded fibers can contribute positively to the mechanical response of the reduced-clinker matrix under the tested configuration. From a sustainability perspective, the result indicates compatibility between reduced Portland cement content and the incorporation of optical fibers while preserving meaningful compressive performance (Shafei et al., 2021).

Additional SEM observations were performed on hole samples (Figure 3.5). In both mixes, dark regions interpreted as pore space were observed near the hole perimeter in the selected fields of view. The binary images in Figure 3.5 c, d provide an approximate two-dimensional estimate of the dark-area fraction within the analyzed regions. The selected eco-mixture field showed a higher local dark-area fraction and a more irregular hole outline than the selected reference-mixture field. These features are consistent with greater local microstructural heterogeneity around the hole in the examined eco-mixture region. The morphology of the holes also differed between the mixtures: while they were expected to be approximately circular, reflecting the geometry of the fiber, the selected eco-mixture image showed a more irregular outline. This morphology may reflect local damage around the hole, with a possible contribution from sample preparation (Stutzman & Clifton, 1999). Together, these observations provide a localized morphological basis for interpreting the mechanical response of the hole-containing specimens.

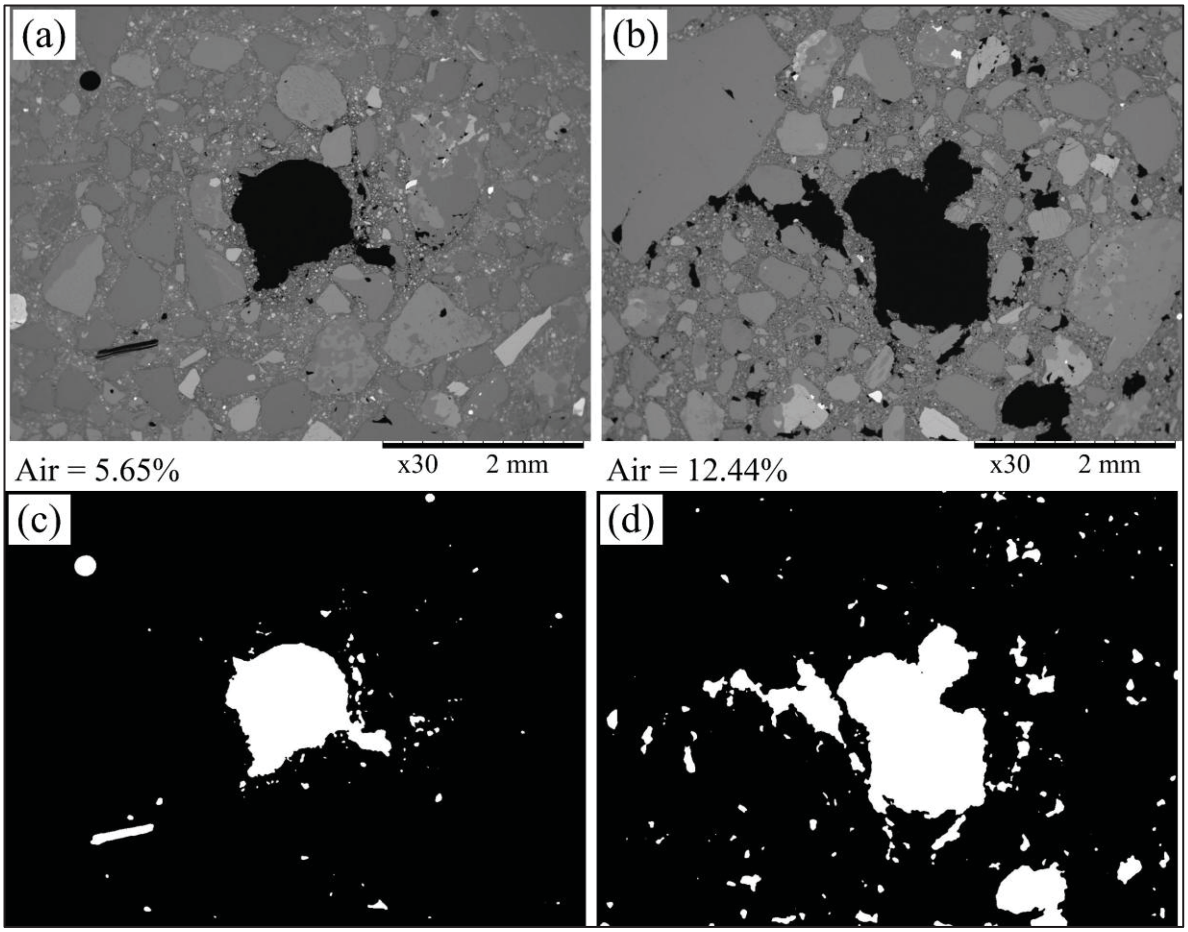

Figure 3.5 Selected backscattered-electron SEM images of the regions surrounding preformed holes in (a) the reference mixture and (b) the eco mixture, with (c,d) corresponding binary segmentations and approximate dark-area fractions for the analyzed fields of view

At nine holes, the eco mixture reached 39.6 MPa, corresponding to a +5.4% increase relative to its control (37.5 MPa), proportionally larger than the +2.4% increase observed in the reference mixture (64.5 vs 63 MPa). Since holes do not provide material-matrix interaction, this comparison shows that the response to an equivalent geometric discontinuity varied with matrix composition. The local differences in dark-area distribution and hole morphology observed in Figure 3.5 are consistent with this matrix-dependent response and provide microstructural context for the experimental results.

Taken together, the results indicate that the mechanical response of fiber-reinforced mortars is not only a function of the number of inclusions but also of the fiber-matrix interface quality, which depends on the mixture proportioning (Henriques et al., 2018; Li, Li, Wang, Tao, & Shi, 2025; Navabi et al., 2021). The mechanical comparisons show that fibers and geometrically equivalent holes produce distinct compressive responses at selected inclusion levels. The SEM images complement these results by revealing local differences in fiber-matrix contact and hole morphology between the two mixtures. These combined observations support a contribution from fiber-matrix interaction and matrix composition to the measured mechanical response, with the microstructural interpretation focused on the examined regions.

3.3.1.3 Numerical stress distribution analysis under compression

Numerical simulations of stress distribution (Figure 3.6) complement the experimental results by showing how fibers and holes modify the elastic stress field under compression. In specimens containing holes, localized compressive stress peaks occurred at the hole boundaries in all investigated configurations. The spatial distribution of these regions changed with the number of holes, providing a qualitative representation of how geometric discontinuities influence the pre-failure elastic stress field. These patterns provide mechanical context for the compressive strength results.

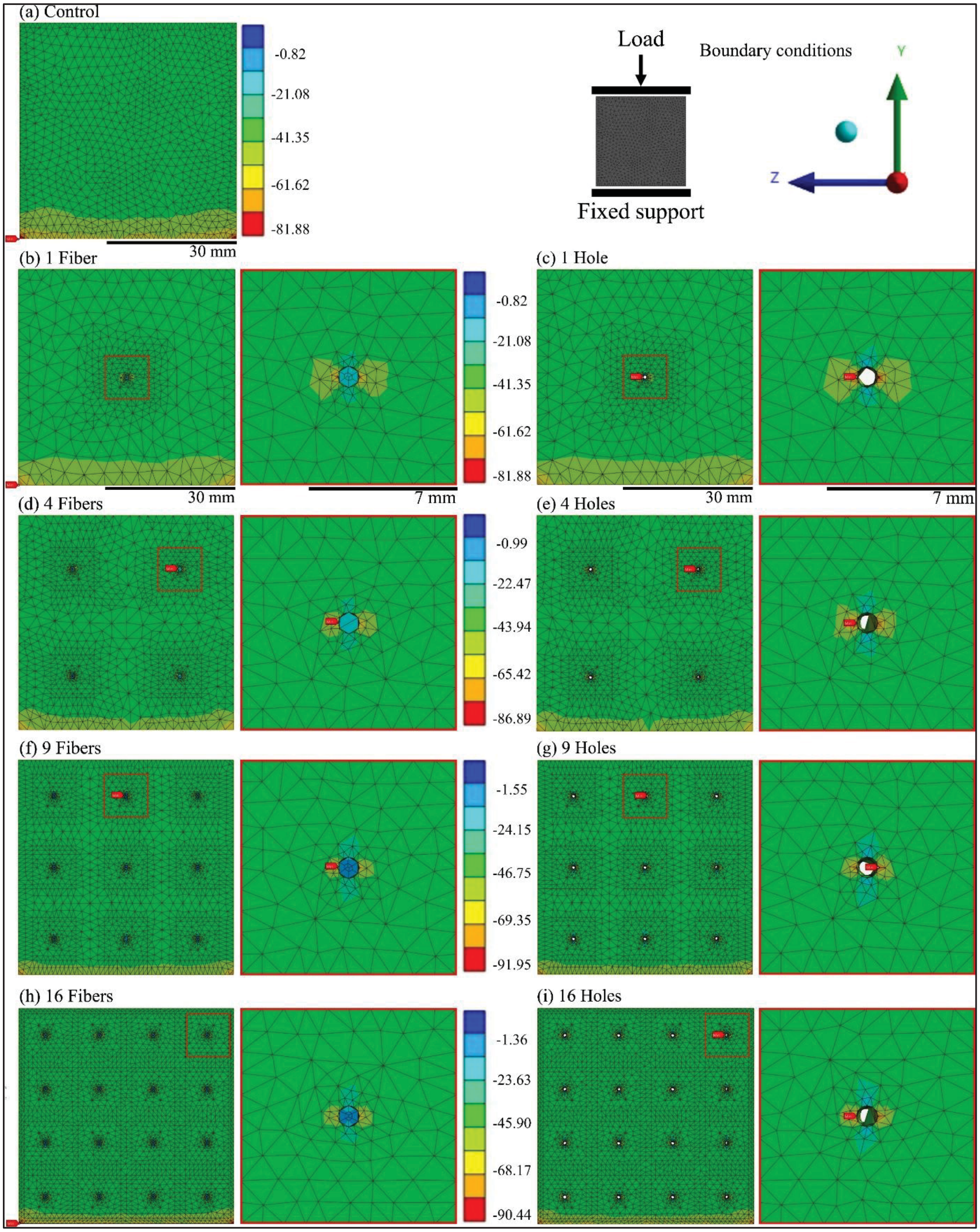

Figure 3.6 Normal stress under compression for mortar with 1, 4, 9, and 16 fibers and holes. Global and zoomed-in views are shown for each case. The red tag represents the highest localized compression applied on the sample

In contrast, samples with fibers showed a more complex behavior. Although fibers disturbed the stress field, the highest compressive stresses were not always concentrated at the fiber-matrix interface. Local regions of near-zero stress were observed around both fibers and holes perpendicular to the loading direction. Compared with holes, fibers produced a more spatially distributed elastic stress field, whereas the peak stresses around holes remained more localized at the inclusion boundaries. Within the modeled elastic regime, this difference shows that the material properties of the embedded fibers influence stress transfer through the surrounding matrix. As the number of fibers increased, the stress field became more broadly distributed, a pattern consistent with the experimental configurations in which compressive strength was maintained or increased.

Local stress concentration at a hole boundary describes the elastic response of a specific region, whereas compressive strength represents the specimen-scale load-bearing response. Tukey's HSD showed that the 4H configuration in the reference mixture was significantly stronger than the control, while 1H and 9H were statistically comparable to it. In the eco mixture, 9H was significantly stronger than the control, while 1H and 4H were statistically comparable. At 16 holes, both mixtures showed significantly lower strengths than their respective controls. These results show that localized elastic stress peaks can coexist with maintained or increased compressive strength at selected inclusion levels, whereas the highest investigated hole density produced an unfavorable specimen-scale response.

The simulations provide an elastic stress-distribution interpretation that complements the experimental compression results. Holes generated boundary-localized stress fields, and the spatial interaction among these regions became more pronounced as the number of holes increased. At 16 holes, this numerical pattern coincided with a significant reduction in compressive strength in both mixtures. Fibers, by contrast, produced a more distributed elastic stress field, consistent with the broader range of tested inclusion levels over which fiber-containing specimens maintained or increased their compressive strength.

3.3.2 Flexural strength

Figure 3.7 presents the flexural strength results at 28 days for mortar samples with varying quantities and orientations of embedded optical fibers and holes. Each point corresponds to the average of three samples, and the red line indicates the control samples tested without inclusions. For the reference mixture, the control samples reached an average flexural strength of 10.9 MPa. The introduction of a single fiber increased strength in both orientations, reaching 11.6 MPa in the transversal direction and 11.8 MPa in the longitudinal direction. A similar improvement was observed for a single hole, with a more pronounced effect in the longitudinal orientation (12.5 MPa). With four fibers, flexural strength remained above the control in both directions. At nine fibers, however, the behavior diverged depending on fiber orientation. In the transversal configuration, strength decreased to 9.5 MPa, while in the longitudinal direction, it was maintained at 11.1 MPa. For holes, the same tendency was observed, where nine inclusions reduced the strength in the transversal direction (9.5 MPa), but the longitudinal samples still reached 12.7 MPa.

These results indicate that, unlike compression, flexural strength did not follow a clear tendency with the number or type of inclusions in the reference mixture. Overall, the beneficial effect of fiber inclusions in flexure was less clear than in compression, with performance being influenced more by alignment than by inclusion quantity or type. While additional inclusions often weakened specimens in the transversal orientation, the longitudinal orientation consistently preserved or enhanced strength.

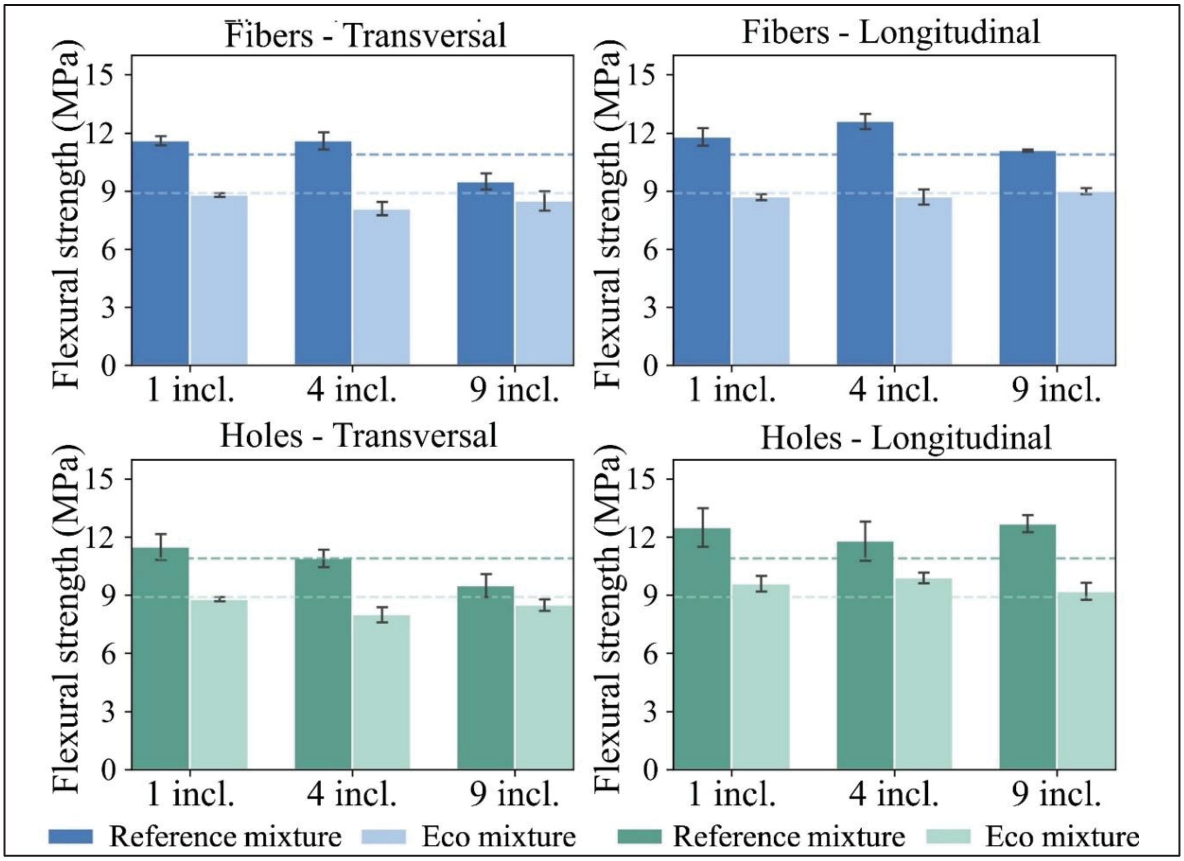

Figure 3.7 28-day flexural strength by inclusion type and orientation for the reference mixture (dark bars) and eco mixture (light bars). The 2×2 layout separates fibers from holes and longitudinal from transverse configurations. Dashed lines indicate the control level for each mixture

In the eco mixture, the control reached 8.9 MPa. The most notable observation is how closely fiber and hole responses tracked each other across all configurations (Figure 3.7), a pattern absent in the reference mixture. Where the reference mixture showed fibers outperforming holes in several conditions, the eco mixture showed a lower distinction between the two inclusion types, consistent with the SEM evidence of degraded fiber-matrix bonding. The orientation effect, however, remained just as strong: longitudinal inclusions preserved or improved strength, while transversal ones consistently reduced it, confirming that orientation governs flexural behavior regardless of matrix quality.

Taken together, these results highlight two key aspects. The first is the dominant effect of orientation over inclusion type. This hierarchy was confirmed by two-way ANOVA (inclusion type × orientation): orientation was a highly significant factor in both mixtures (reference: $F = 48.1$, $p < 10^{-6}$; eco: $F = 47.7$, $p < 10^{-6}$) and exerted a substantially stronger effect than inclusion type (reference: $F = 7.9$; eco: $F = 4.2$; both $p < 0.01$). A significant interaction ($p < 0.01$ in both mixtures) indicates that the influence of orientation varied with inclusion configuration. To substantiate this hierarchy, consider the following direct comparisons from the reference mixture data. At 9 inclusions in the longitudinal configuration, switching from fiber to hole changes strength from 11.1 MPa to 12.7 MPa, an absolute difference of 1.6 MPa, representing a ~15% variation relative to the control (10.9 MPa). By contrast, switching from longitudinal to transverse orientation within the fiber condition at 9 inclusions changes strength from 11.1 MPa to 9.5 MPa, an absolute reduction of 1.6 MPa, representing a ~14% decrease relative to the control. In the eco mixture, this contrast is even more pronounced: longitudinal hole samples at 9 inclusions reach 9.2 MPa, while transverse hole samples at the same count remain at or below the control of 8.9 MPa, yet the difference between fiber and hole at the same orientation rarely exceeds 0.5 MPa. These comparisons confirm that re-orienting inclusions from longitudinal to transverse consistently produces strength changes of comparable or greater magnitude than replacing fibers with equivalent-geometry holes across both mixture designs. This anisotropy is explained by how inclusions interact with crack initiation and propagation (Liu et al., 2023; Lyu et al., 2024). In the longitudinal direction, inclusions are aligned with the flexural span and may delay crack growth by promoting stress redistribution or deflection of the fracture path. In the transversal direction, inclusions cut across the narrow section and promote local stress concentration, so their accumulation at higher numbers reduces the ability of the matrix to sustain flexural loads (Huynh Phuong Nam et al., 2022; Lone, Zhao, Fan, & Zhou, 2025).

The second aspect is the effect of the mixture proportioning. At low to moderate levels (one and four inclusions), fibers and holes had a neutral or even positive effect on strength, particularly in the longitudinal direction. At higher levels (nine inclusions), the beneficial effect was lost in the transversal configuration, indicating that the matrix cannot accommodate a high density of discontinuities without compromising integrity. The numerical simulations in Figure 3.8 corroborate this conclusion: stress redistribution patterns differ markedly between longitudinal and transverse configurations (Lyu et al., 2024), while the fiber-versus-hole distinction produces only subtle differences in the simulated stress fields, consistent with the experimentally observed dominance of orientation over inclusion material type.

Finally, the distinction between fibers and holes was less evident in flexural strength than in compressive strength. In the reference mixture, fibers generally performed slightly better than holes, but in the eco-cement mixture their behavior was analogous. This trend is consistent with the SEM observations, where the weaker matrix of the low-cement mixture exhibited larger interfacial gaps and higher porosity, limiting the effectiveness of fiber-matrix bonding. In the eco mixture, fiber and hole flexural responses were similar across all transversal configurations and nearly converged at nine longitudinal inclusions, suggesting that fiber-matrix bonding contributes negligibly to flexural strength when matrix quality is reduced. The relative contribution of bonding quality versus matrix porosity to this behavior cannot be fully separated from the present experimental data alone and represents a direction for future investigation.

3.3.2.1 Numerical stress distribution analysis under flexion

Figure 3.8 shows the equivalent stress distribution under three-point bending for mortar beams with embedded fibers or preformed holes in different quantities and orientations. The control sample presented the expected distribution, with stresses concentrated beneath the loading point and spreading toward the supports, consistent with observations in other cementitious composites with different reinforcement materials (rubberized, nano silica fiber, carbon cloth waste fiber) (Anmeeganathan, Ravichandran, & Subramanian, 2018; Lone et al., 2025; Zhu et al., 2025) indicating that this stress pattern is a general feature of flexural loading rather than material specific.

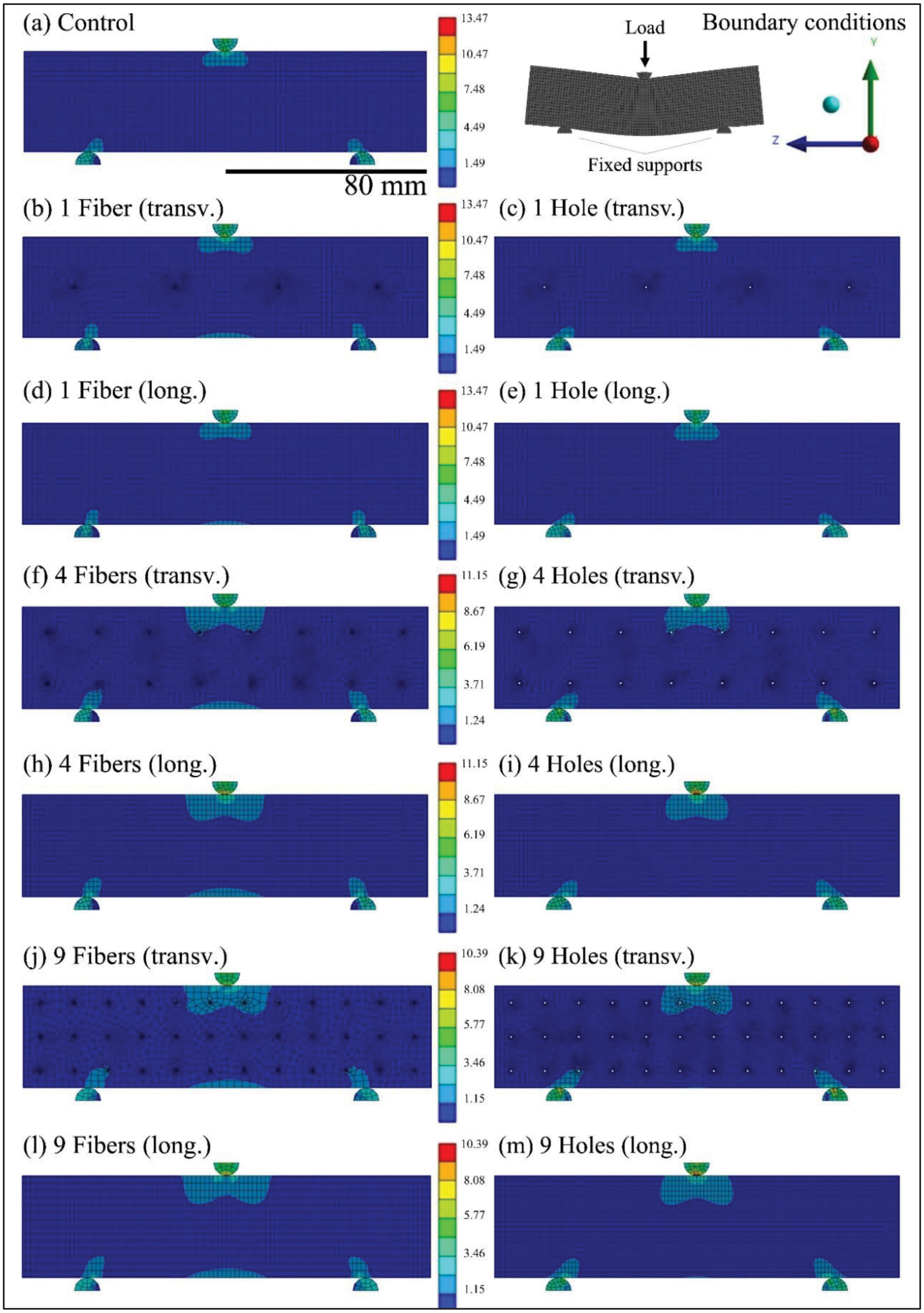

Figure 3.8 Equivalent stress fields from numerical simulations of mortar under flexural loading

The flexural simulations show that the dominant stress concentrations occur at the loading point and support regardless of inclusion type or count, consistent with classical three-point bending behavior. The fiber versus hole distinction produces subtle differences in the simulated stress fields across all configurations, supporting the experimental finding that inclusion type is secondary to orientation in governing flexural performance. Given the linear elastic formulation and the sensitivity of local stress patterns to mesh geometry around transversal inclusions, the flexural simulations are best interpreted as qualitative indicators rather than precise predictors of stress redistribution. When comparing fibers and holes, differences were relatively subtle, in agreement with Štochl et al., (2023). Both modified stress contours in similar ways, indicating that orientation was the dominant factor controlling stress localization. A slight distinction appeared where fibers allow to sustain stress transmission along the bottom span, while holes primarily interrupted the stress path, concentrating stresses at their periphery. This nuance is consistent with the experimental results of the reference mixture, where fibers occasionally outperformed holes.

Overall, the simulations confirm that orientation governs whether inclusions mitigate or intensify stress localization. The role of fibers versus holes was less obvious to discern, with differences only becoming evident in specific cases. Since the simulations did not account for different mixture proportions, the main insight is that anisotropy dominates flexural performance, while the beneficial role of fibers depends strongly on an effective bond with the surrounding matrix (Henriques et al., 2018; Huynh Phuong Nam et al., 2022).

3.4 Conclusions

This study provides direct experimental demonstration that the mechanical effect of embedded optical fibers in cementitious composites is not simply a function of the hole they occupy, the fiber material itself contributes independently to compressive strength, and this contribution scales with inclusion density and matrix quality. Under compression, both fibers and holes generally contributed to strength gains over the reference mixture. Fiber samples generally outperformed the control samples, even at higher inclusion numbers, suggesting a beneficial interaction with the matrix.

Holes also produced strength gains at selected intermediate inclusion levels. The 4H configuration in the reference mixture and the 9H configuration in the eco mixture were significantly stronger than their respective controls. These results identify tested configurations in which preformed holes remained compatible with maintained or improved compressive strength despite the reduction in solid cross-sectional area. At 16 holes, both mixtures showed significant strength reductions, indicating that the mechanical effect of geometric discontinuities depends on inclusion density and matrix composition within the investigated range. In the eco mixture, the 9F configuration also produced a significant strength gain relative to the control, showing that the reduced-clinker matrix remained mechanically compatible with embedded optical fibers under the tested configuration. The local differences in fiber-matrix contact observed by BSE provide morphological context for this mixture-dependent response.

In flexural loading, inclusions were beneficial when aligned longitudinally, enhancing resistance in both mortar mixes regardless of whether fibers or holes were used. Orientation was as influential as inclusion type, with switching from longitudinal to transversal consistently producing strength reductions of comparable or greater magnitude than replacing fibers with equivalent-geometry holes at the same inclusion count.

Numerical simulations complemented the experimental findings under compressive and flexural loading by comparing the elastic stress fields generated by the investigated inclusion configurations. Under compression, holes produced more boundary-localized stress patterns, while fibers produced more distributed elastic fields. Under flexure, the simulations highlighted the influence of inclusion orientation on the elastic stress distribution. The linear elastic formulation therefore provides a qualitative pre-failure comparison that connects inclusion geometry and orientation with the experimentally observed mechanical response.

Overall, the results demonstrate that optical fibers do not inherently compromise mechanical performance and, depending on inclusion density and orientation, may even enhance it. Geometric disruption was identified as the dominant factor, with fiber-matrix bonding providing an additional contribution to stronger mortars. The deliberate introduction of holes may appear detrimental, yet in some cases can result in surprisingly efficient load-bearing behavior relative to the reduced material volume. These findings support the development of materials capable of combining structural and optical functions, enabling applications such as daylight transmission, reduction of artificial lighting demand, and integration of sensing or signaling functions in building elements. This work represents another step towards the research and application of light-transmitting cementitious materials and smart, multifunctional building components.

CHAPTER 4

RANDOMLY DISTRIBUTED OPTICAL FIBERS IN TRANSLUCENT MORTAR FOR PRIVACY-PRESERVING LIGHT TRANSMISSION AND DIGITAL IMAGE RECONSTRUCTION

Karina Hwang Arcolezi [a, b], Vivien Marion [b, c], Bora Ung [b], Claudiane Ouellet-Plamondon [a]

[a] Department of Construction Engineering, École de technologie supérieure,
1100 Notre-Dame Ouest, Montréal, Québec, Canada H3C1K3
[b] Department of Electrical Engineering, École de technologie supérieure,
1100 Notre-Dame Ouest, Montréal, Québec, Canada H3C1K3
[c] Université de Bordeaux, INP Enseirb-matmeca, Talence, France

Article published in *Scientific Reports* vol. 16, December 2025, available at
https://doi.org/10.1038/s41598-025-32224-2

Abstract

Light-transmitting building materials often compromise visual privacy due to coherent light transmission. This study presents a novel composite utilizing randomly distributed optical fibers coupled with a computational image reconstruction system. A limestone-calcined clay cement (LC^3) inspired matrix was designed for sustainability and material performance. An algorithmic approach assigned a random traceable fiber distribution via a bijective input-output mapping. The random fiber configuration achieves effective light diffusion, preserving physical privacy. However, using digital imaging and homography-based calibration, the network was computationally reconstructed to reverse the diffusion, recovering hidden visual information accurately. This demonstrates a dual functionality: architectural privacy combined with selective digital transparency. Geometric robustness tests confirmed a stable operational envelope (estimated error of 2.9%) across viewing distances of 30-110 cm and camera rotation angles up to ± 35° (pitch and yaw), establishing these fiber-instrumented cementitious composites as hybrid physical-digital materials for smart infrastructure applications.

4.1 Introduction

The incorporation of light-transmitting elements in construction materials has been studied as a strategy to improve daylight utilization, reduce dependence on artificial lighting, and enhance the aesthetic performance of buildings (Ahuja & Mosalam, 2017; Huang, 2020; Shen & Zhou, 2021; Shenoy, Nayak, Tantri, Shetty, & Shendkar, 2023; Štochl et al., 2023; Su et al., 2020; Su, Zhang, Liu, et al., 2022). Various approaches have been explored to achieve this goal, including the use of glass blocks, translucent polymers, and cementitious composites with embedded inclusions designed to guide or diffuse light (Arias-Erazo, Villaquirán-Caicedo, & Goyes, 2021; Edris, Odah, Abu-Qasmieh, & Hendy, 2021; Pagliolico et al., 2015). Together, the development of the cementitious matrix itself is moving toward low-carbon alternatives, such as Limestone Calcined Clay Cement (LC^3), which offers a sustainable base for high-performance architectural materials (Jin et al., 2025). These solutions often seek to balance structural performance with visual effects, offering both functional and architectural benefits.

Among the different methods, the incorporation of optical fibers into cementitious matrices has attracted particular attention (Arcolezi, Brial, Ung, & Ouellet-Plamondon, 2026; Arcolezi, Zimmermann, Ung, & Ouellet-Plamondon, 2026). Optical fibers transmit light efficiently across relatively long distances while maintaining their flexibility and compatibility with casting processes (Nam et al., 2023; Su, Zhang, Liu, et al., 2022; Taheri, 2019). When embedded in mortars or concretes, they enable external light to penetrate through solid, opaque elements, creating composites that combine mechanical strength with the ability to channel illumination into interior spaces (Bai et al., 2024; Henriques et al., 2018; M. Li, Lu, & Yang, 2022; Yue Li, Li, Wan, & Xu, 2015; Štochl et al., 2023).

Most studies in this field have focused on configurations where fibers are placed in straight and parallel arrangements (Chiew, Ibrahim, & Mohd Ariffin, 2024; Chiew, Ibrahim, Mohd Ariffin, Lee, & Singh, 2021, 2023; Henriques et al., 2018; Li et al., 2022; Li, Li, Wan, et al., 2015; Luhar et al., 2021; Nam et al., 2023; Navabi et al., 2023; Navabi, Javidruzi, Hafezi, & Mosavi, 2021). This design ensures efficient light transfer and, in many cases, allows the perception of shapes or silhouettes from the opposite side of the material (Huang, 2020; Kim, 2017). While this property produces distinctive visual outcomes, it also introduces a limitation. In applications where privacy is required, the transmission of recognizable contours may restrict the use of these composites.

In recent years, the development of light-transmitting concretes has also intersected with broader research on smart and responsive materials, where optical components are used not only for illumination but also for information capture and visualization (Arcoleziet al., 2025; Marin, Philippe, & Blanchi, 2014; Said, 2020). Such materials open perspectives for real-time monitoring, imaging, and augmented-reality applications in construction, enabling interactive or perceptive building elements.

In this work, we propose a different approach. Instead of a parallel arrangement, fibers are introduced in a random distribution that modifies the way light propagates through the material. This strategy produces a composite that is partially translucent while reducing the possibility of visual recognition of shapes and objects behind it. This design is conceived as a functional material for architectural privacy, but also as a physical platform for optical data transmission and digital imaging experiments. Beyond the physical development of the composite, we also explore a digital perspective. By mapping the position of each fiber, it becomes possible to reconstruct them computationally into ordered virtual paths. This process, which we define as a type of digital reverse engineering, makes it feasible to reconstruct visual information hidden in the physical specimen. The main objectives of this study are therefore twofold:

i) To develop a mortar-based light-transmitting composite with randomly distributed optical fibers, capable of combining light transmission with privacy;
ii) To establish a digital methodology for the geometric reverse engineering of the randomized fiber network, demonstrating that the diffused light can be computationally reconstructed to recover hidden visual information.

By combining physical material design and digital reconstruction, this study proposes a new paradigm where the composite functions as an active physical-digital interface, transforming a passive architectural component into a functional optical processor. This dual functionality positions the composite both as a privacy-preserving material and as a platform for selective visual information retrieval, highlighting its potential as an active physical-digital component in architectural applications. This approach aims to expand the potential of translucent composites in architecture, where both light transmission and privacy represent key features.

4.1.1 Conceptual design of the semi-translucent composite with privacy

In conventional light-transmitting concretes, the optical performance is influenced primarily by the geometric configuration of the fibers, which are commonly embedded in straight and parallel distribution (Figure 4.1) (Huang, 2020; Li, Li, & Guo, 2015; Pourkazemi, Vahdati, Mirvalad, & Mahdikhani, 2024; Rong et al., 2023). This arrangement creates direct optical channels between the two faces of the element, allowing light to pass with limited deviation from its original direction. Several studies report that such parallel configurations can preserve a degree of spatial correspondence between the illuminated and receiving faces, making it possible in many cases to perceive general contours or shapes through the panel (Huang, 2020; Kim, 2017). Although the extent of this visual coherence depends on several parameters, such as fiber density, diameter, spacing, and lighting conditions, straight-line arrangements tend to maintain a recognizable structure in the transmitted light (Huang, 2020; Nam et al., 2025). From an architectural standpoint, this can be desirable to convey visual information or enhance transparency, but it may also limit the use of these systems in contexts where privacy is required.

To address these limitations, the design proposed in this study diverges from the conventional approach by introducing fibers with no predefined alignment, crossing the specimen along irregular paths. These trajectories interrupt direct optical channels and disperse the transmitted light, reducing coherence and preventing the formation of discernible shapes. The resulting composite combines two functions, allowing the passage of light while suppressing visual perception, which creates a pathway toward privacy-oriented translucent architectural elements.

Previous studies have also explored randomly distributed fibers, often referring to a non-uniform planar arrangement (Henriques et al., 2018), but with parallel, linear trajectories through the specimen, and almost exclusively to characterize their physical properties, such as fiber orientation (Nam et al., 2023), intersection density, or network connectivity for understanding material formation or mechanical performance. These efforts treated randomness as a structural descriptor rather than as an optical mechanism.

In addition to studies focused on optical, mechanical, or structural properties, other research has investigated the reconstruction and analysis of fiber network topology using image-based approaches. Tang et al., (2009) and D'Amore et al., (2010) demonstrated that imaging and reconstruction techniques can be used to characterize and modify complex fibrous networks through descriptors such as connectivity, orientation, and branching. Although these works are not related to optical transmission, they highlight the broader applicability of image analysis for extracting and reorganizing information from disordered fiber structures. Within this context, similarity metrics commonly used in image analysis, such as Normalized Cross-Correlation (NCC), provide a quantitative means to evaluate spatial correspondence between images or reconstructed patterns (Atmaja, Wibirama, Herliansyah, & Sudiarso, 2025; Han, Kim, & Kwon, 2012; Li, Su Win, Fan, Li, & Lin, 2025; L. Meng et al., 2025).

Other approaches, such as Li et al., (2025); Li, Yin, & He, (2025) and Zheng et al., (2024) have developed algorithms for 3D reconstruction of granular or fibrous networks and dense image segmentation using vision-based models. Although these methods focus on granular media or biological tissues rather than light transmission, they highlight the utility of computational reconstruction and topological analysis to recover structural information from complex, irregular networks. Such concepts support the broader relevance of digital mapping and reconstruction strategies for fiber-based materials.

Accordingly, while these studies incorporate a form of randomness, the random three-dimensional trajectories as a means to disrupt optical coherence or enable digital reconstruction intentionally are not employed, which constitutes the main conceptual contribution of the present work. In contrast, the proposed design treats the random network not as a property to be analyzed, but as a physical encryption layer: the random paths intentionally diffuse light in the physical domain while remaining traceable for digital reconstruction.

Figure 4.1 compares both configurations. In conventional design (Figure 4.1a), parallel fibers transmit light directly, preserving shapes. In the proposed configuration (Figure 4.1b), randomly oriented trajectories scatter the transmitted light, preventing image formation while maintaining brightness. The irregular fiber paths also generate a complex internal pattern that can later be captured, analyzed, and reconstructed digitally.

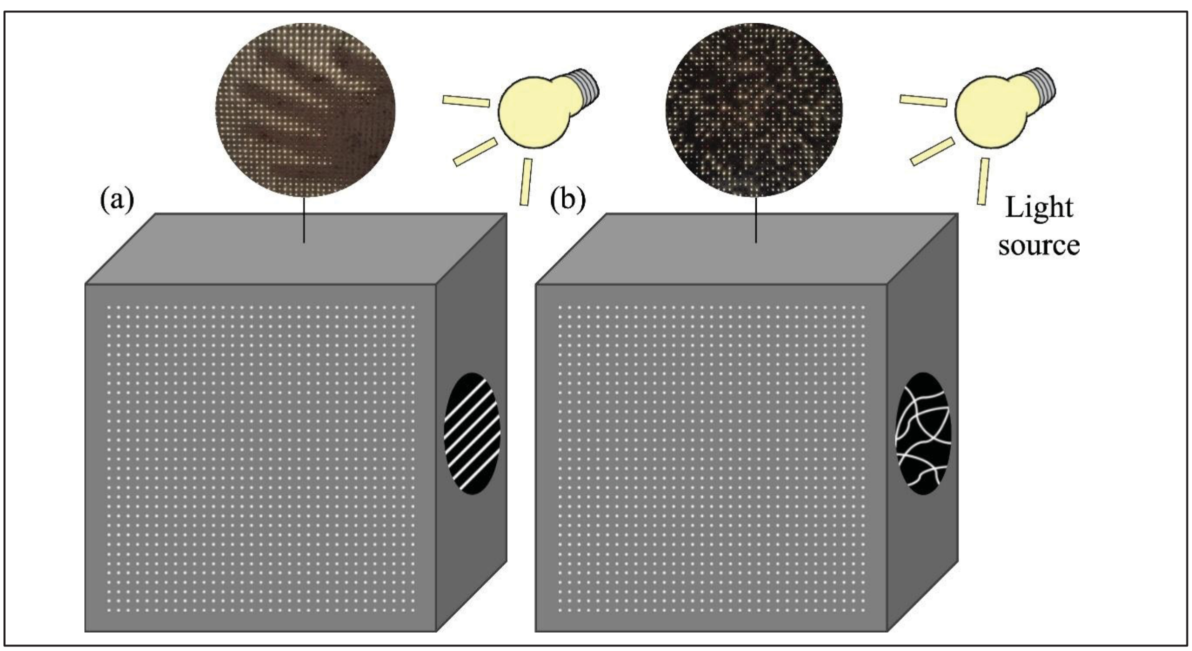

Figure 4.1 Comparison between (a) a conventional light-transmitting composite with parallel fibers, and (b) the proposed random fiber distribution, which diffuses light and maintains privacy

The random distribution was not produced arbitrarily but generated through a computational algorithm that assigns a unique correspondence between each entry and exit point of the fibers. This approach ensures that randomness is fully traceable and reproducible, allowing the physical arrangement to be digitally reconstructed afterward. Each fiber, therefore, carries both an optical and an informational role, acting as an individual data channel within a randomized network.

This property enables a second level of analysis. The internal network of fibers can be mapped not only as spatial geometry but also as a framework for light transfer. Once recorded, the random paths may be computationally reconstructed into virtual straight lines, creating a digital version of the specimen with ordered transmission channels. In this virtual configuration, light emerging from random exit points is reassigned to coherent paths, which makes it possible to reconstruct images hidden by the physical material. Figure 4.2 illustrates this principle. A background object, represented by the letters “ÉTS”, remains indiscernible in the physical sample, yet becomes visible when the recorded fiber network is reconstructed digitally.

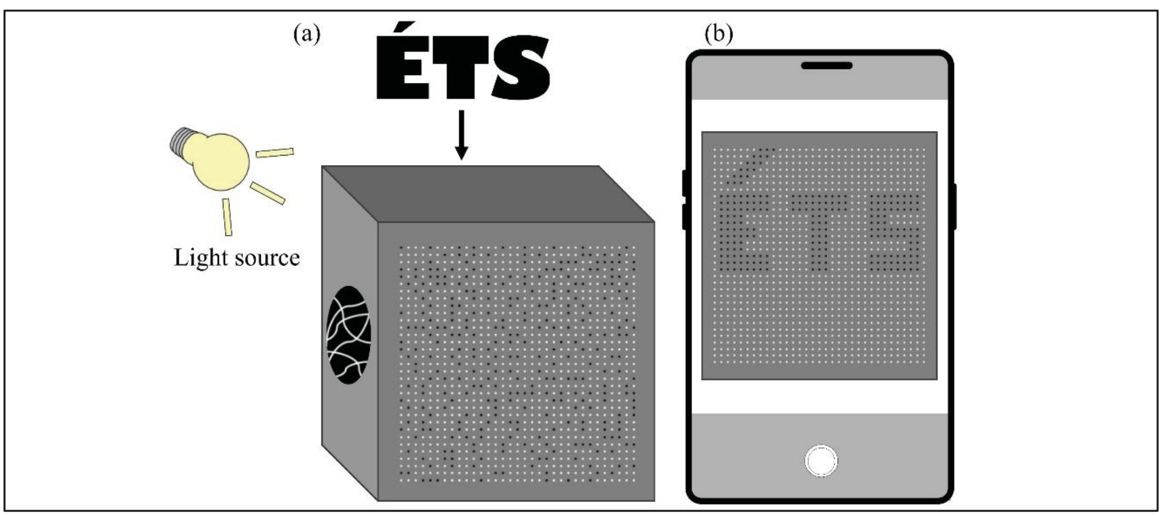

Figure 4.2 Digital reconstruction of fiber paths enables recognition of hidden letters “ÉTS” that remain indistinguishable in the physical specimen

In summary, the proposed design replaces parallel fiber arrangements with traceable random trajectories, enabling light transmission while suppressing visual recognition at the material level. At the same time, the preserved fiber mapping allows digital reconstruction, defining the composite as a physical-digital optical interface for privacy-oriented architectural applications.

4.2 Materials and methods

4.2.1 Fabrication of the semi-translucent composite with privacy

The cementitious matrix material used was a limestone calcined clay cement (LC^3)-inspired mortar (Jin et al., 2025) (Table 4.1). The selection of LC^3 was based on a dual requirement of sustainability and material performance. From a sustainability perspective, this system enables a clinker replacement exceeding 40% (Jin et al., 2025; Scrivener, Martirena, Bishnoi, & Maity, 2018), reducing the use of Portland cement, which is a contributor to global CO_2 emissions from the construction sector (Supriya, Chaudhury, Sharma, Thapliyal, & Singh, 2023). In addition, the chemistry of LC^3 provides better control over the rheology and microstructure of the fresh mortar. The reaction between the alumina in the calcined clay and the calcium carbonate in the limestone leads to the precipitation of additional hydrates, notably carboaluminates and ettringite (Marangu, 2020; Scrivener et al., 2018). These reactions contribute not only to the final mechanical performance but also to microstructural refinement, improving the balance between viscosity and flowability for effective infiltration of the dense fiber network.

Ordinary Portland cement (Type GU, CSA A3000) (CSA, 2018) was used as the primary binder. Supplementary cementitious materials included calcined clay (CC) and limestone filler (LF), following mix design principles established for LC^3 systems (Alghamdi, Shoukry, Abadel, & Khawaji, 2023; Hassan et al., 2023; Jin et al., 2025; Scrivener et al., 2018). Natural river sand (Sa), with a maximum particle size of 2.5 mm, was used as a fine aggregate. A polycarboxylate-based superplasticizer (SP) was incorporated to achieve the required workability. Mortar mixing was performed per ASTM C305 (ASTM, 2014), and specimens were cast and cured following ASTM C109-21 (ASTM, 2021) standard practices. The mix design aimed to produce a matrix compatible with optical fiber embedding, ensuring sufficient viscosity to prevent fiber displacement during casting while maintaining adequate flowability to penetrate the dense and entangled fiber network. Preliminary tests were performed to adjust the flow value for controlled casting without segregation, as proposed by Jin et al., (2025). Specimens were demolded after 24 h and cured in a humidity chamber (23 ± 2 °C, RH > 95%) for 28 days prior to mechanical and optical testing.

Table 4.1 Composition and properties of the partially translucent material

OPC	**CC**	**LF**	**Sa**	**Water**	**SP**	**Flow***	**Density**	**Compressive strength****
kg/m³						%	kg/m³	MPa
390	162.5	97.5	1310	255	15	152	2210	49.9 ± 0.2

*Measured as per ASTM C1437 (Astm, 2001)

**Average of three samples as per ASTM C109-21

The light-transmitting elements were polymethyl methacrylate (PMMA) optical fibers (Eska™, Mitsubishi Chemical). Each fiber had a core diameter of 1 mm, a core refractive index of 1.49, and a numerical aperture of 0.5.

4.2.2 Random fiber distribution and algorithmic traceability

To achieve a traceable random distribution of the optical fibers, a computational algorithm was implemented. The mold consisted of two parallel acrylic plates, face A (entry) and face B (exit), each containing a 33×33 grid of potential fiber positions, spaced at a centre-to-centre distance of 0.5 cm. Each position was indexed according to a coordinate system where the first two digits represented the row and the last two digits the column of a matrix.

For each fiber, the algorithm sequentially selected coordinates on faces A (A0101 to A3333) and assigned a random, non-repeating exit coordinate on face B. This procedure utilized all $33^2 = 1089$ entry points and ensured that the irregular path of each fiber remained fully traceable through a recorded input-output mapping matrix M (Equation (4.1)).

$$M = \begin{bmatrix} A_1 & B_{r(1)} \\ A_2 & B_{r(2)} \\ \vdots & \vdots \\ A_n & B_{r(n)} \end{bmatrix}, N = 1089 \quad (4.1)$$

Where A_i represents the coordinate index of the *i-th* fiber on face A, and $B_{r(i)}$ denotes its randomly assigned exit coordinate on face B, determined by a permutation function $r_{(i)}$ such that $r_{(i)}$ is a bijective mapping of {1, …, n} onto itself. This bijective mapping defines a unique correspondence between entry and exit points, encoding both geometric randomness and complete traceability of the fiber network. The resulting dataset later serves as the geometric basis for the digital reconstruction and homography alignment (Luo et al., 2023; Wang et al., 2025).

Following the dataset defined by the mapping matrix M, fibers were manually threaded through the mold and fixed before mortar pouring. This configuration was therefore both random in the geometric arrangement of fibers, and controlled through the algorithmic mapping that guaranteed complete traceability. A control specimen containing the same number of fibers aligned in straight, parallel paths was also fabricated for direct comparison of light diffusion and privacy performance (Figure 4.3).

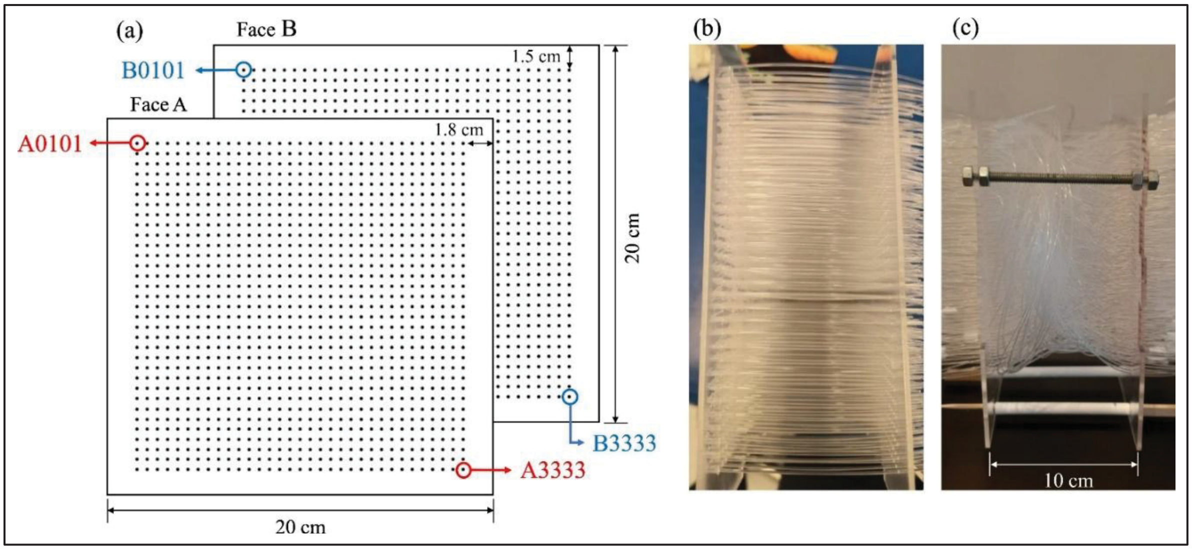

Figure 4.3 Representation of the fiber distribution system. (a) Schematic of the acrylic face A and B, (b) mold with fibers placed straight, and (c) mold with fibers placed randomly

To preserve the integrity of the fiber network during casting, the fibers were mechanically constrained by the rigid acrylic mold plates. Since the fibers pass through fixed grid holes, the mapping matrix M is defined strictly by these fixed boundary coordinates. Therefore, regardless of minor internal displacements caused by mortar flow or hydration, the input-output correspondence remains consistent. To further secure this arrangement, the fibers were prepared with a significant excess length relative to the mold depth (Figure 4.1c), providing sufficient margin to prevent tension forces from dislodging the fiber ends during casting. Finally, the rheology of the LC^3 matrix was optimized to achieve close to a self-compacting consistency, allowing the mortar to infiltrate the entangled fiber network under gravity without the need for heavy vibration, thus minimizing the risk of fiber breakage or displacement (Nam et al., 2023).

4.2.3 Digital reconstruction and reverse engineering

4.2.3.1 Image acquisition and calibration

For the digital reconstruction, images of the specimen's exit face (Face B) were acquired using a portable camera connected to a system running *MATLAB* (including the Computer Vision

Toolbox). To calibrate the image and correct for perspective distortions, four coloured markers were positioned at the corners of the 33×33 grid. A preliminary colour study confirmed that yellow and orange offered the highest visibility and contrast under variable lighting conditions. The selection criteria involved maximizing a visibility metric, defined as the average sum of saturation and luminosity for each tested colour. To manage camera rotations exceeding 90º, one marker was assigned a distinct colour (orange), serving as an orientation reference to prevent misidentification (Figure 4.4b).

4.2.3.2 Automated calibration via homography transformation

The geometric correspondence between the fiber exit grid (Face B) in the image space and the theoretical coordinate system was established through a Homography Transformation Matrix H, similar to that proposed by Wang (C. Wang et al., 2025). This is important for correcting perspective distortion caused by camera position and angle. The homography matrix *H* relates a point $x_1 = (x_1, y_1, 1)^T$ in the image (distorted) plane to its corresponding point $x_2 = (x_2, y_2, 1)^T$ in the rectified (orthogonal) plane (Equation (4.2)).

$$H = \begin{pmatrix} h_{11} & h_{12} & h_{13} \\ h_{21} & h_{22} & h_{23} \\ h_{31} & h_{32} & h_{33} \end{pmatrix} \tag{4.2}$$

Considering four pairs of points, denoted as (x_1, y_1) and (x_2, y_2) for images A and B, respectively, which define a quadrilateral in each image. The correspondence between these coordinates and the coefficients of the homography matrix *H* is then established as Equation (4.3).

$$\begin{cases} x_2 = \dfrac{h_{11}x_1 + h_{12}y_1 + h_{13}}{h_{31}x_1 + h_{32}y_1 + h_{33}} \\ y_2 = \dfrac{h_{21}x_1 + h_{22}y_1 + h_{23}}{h_{31}x_1 + h_{32}y_1 + h_{33}} \end{cases} \tag{4.3}$$

Assuming h_{33}=1, this relationship can be expressed in linear form as AX=B, where $X = [h_{11} \quad h_{12} \quad h_{13} \quad h_{21} \quad h_{22} \quad h_{23} \quad h_{31} \quad h_{32}]^T$, and matrices A and B are constructed from the coordinate pairs of the corresponding points. The coefficients of H are solved by least-squares estimation, and the inverse transformation of H^{-1} satisfies $H \cdot H^{-1} = I$. This homographic model establishes the spatial consistency necessary to ensure that the reconstructed fiber network accurately reflects the real geometry of the specimen, regardless of camera orientation.

Specifically, while the pre-recorded mapping matrix (M) establishes the logical inverse relationship between fiber coordinates, a computational algorithm is essential to bridge the gap between this theoretical map and the dynamic, real-world image capture. The algorithm serves three main functions: first, it performs image processing and segmentation to accurately identify the discrete light signature of each fiber on the physical exit surface. Second, it calculates a homography transformation matrix (H) to dynamically correct the captured image for real-world perspective and projection distortions (camera angle, distance). This step is necessary to ensure the physical light patches are precisely aligned with the theoretical grid defined in M. Only after these geometric and photometric corrections are applied can the system utilize M to reassign the image patches to their virtual, ordered coordinates, rendering hidden objects visible (Luo et al., 2023).

4.2.3.3 Digital reconstruction algorithm

The core of the reconstruction relied on the rectified image of face B and the pre-recorded mapping matrix *M*. The reconstruction procedure involved two steps for each frame:

i) Patch assignment: after image rectification, a small quadrangular image area (patch) was digitally assigned around the exit point of each of the *N*=1089 fibers (Figure 4.4a). This patch represents the light signal transmitted through that specific fiber.

ii) Virtual realignment: the *N* image patches were then repositioned into a new, ordered virtual grid according to the inverse logic of the mapping matrix *M* (Figure 4.4c). For every fiber i, the light patch recorded at the random physical output coordinate $(B_{x_i'}, B_{y_i'})$ was computationally reassigned to the coherent virtual output coordinate (B_{xi}, B_{yi}). This process digitally reverses the scattering effect, converting the physically diffused light pattern into a coherent visual image.

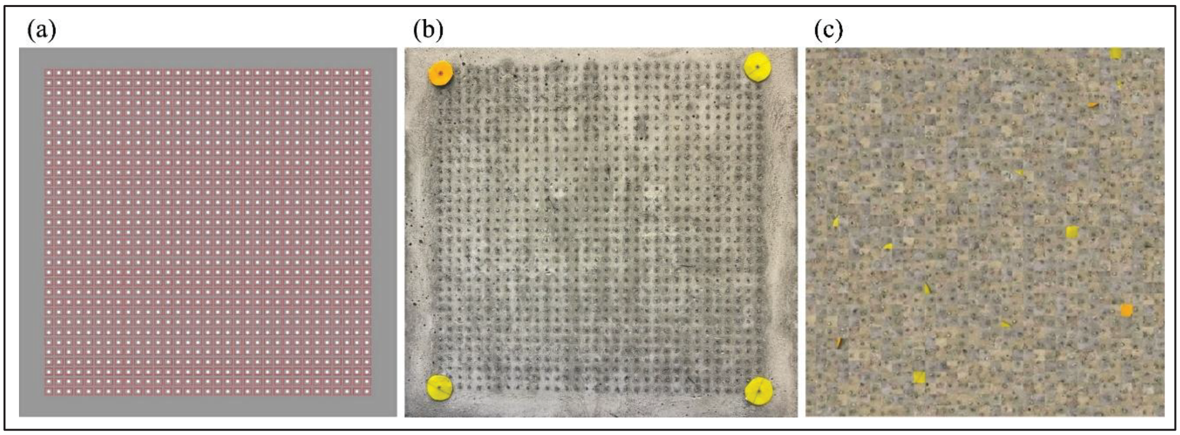

Figure 4.4 Digital acquisition and calibration of the fiber grid: (a) quadrangular areas assigned to each fiber, (b) coloured markers placed at the corners of the grid for calibration; (c) reconstructed view of the grid after homography transformation.

4.2.3.4 Normalized 2D cross-correlation

To quantify the similarity between predefined templates and the target images (reconstruction and privacy-preserving images), this study utilizes the normalized cross-correlation (NCC) function. This technique serves to confirm the fidelity of the reconstructed images by successfully matching known templates taken from a reference image (e.g., the letters 'É', 'T', 'S'), and assessing the effectiveness of the privacy by observing the maximum correlation score, where a lower score indicates greater privacy protection.

NCC is a widely used measure for template matching in computer vision (Atmaja et al., 2025; Han et al., 2012; Li, Su Win, Fan, et al., 2025; Meng et al., 2025). It quantifies the linear relationship between a template T and a patch of an image I (of the same size as T) by normalizing the cross-correlation result. This normalization makes the method robust to changes in image lighting and exposure. The NCC coefficient, $R(u,v)$, at a location (u,v) in the image I, is computed as Equation (4.4).

$$R(u,v) = \frac{\sum_{x,y}\left[I(x,y) - \bar{I}_{u,v}\right] \cdot \left[T(x-u,y-v) - \bar{T}\right]}{\sqrt{\sum_{x,y}\left[I(x,y) - \bar{I}_{u,v}\right]^2 \cdot \sum_{x,y}\left[T(x-u,y-v) - \bar{T}\right]^2}} \tag{4.4}$$

Where $\bar{T}$ is the mean intensity of the template, and $\bar{I}(u,v)$ is the mean intensity of the image patch at position (u,v). The resulting coefficient ranges from -1 to 1, with 1 indicating perfect correlation. In this study, for each template, the maximum NCC value within the target image is recorded as the similarity score. High values indicate successful template reconstruction, while lower values in privacy-preserving images indicate effective obfuscation. By analysing the maximum correlation value, this quantitative approach allows an objective assessment of both reconstruction fidelity (higher values) and privacy effectiveness (lower values).

4.2.3.5 Real-time processing and geometric robustness tests

To assess the dynamic performance and the system's robustness for practical applications, the entire processing pipeline was tested under two conditions:

i) Dynamic scene test, where the specimen was placed in front of a moving object (e.g., a hand opening and closing). The motion was captured as a video sequence, and the algorithm was applied frame-by-frame to demonstrate the temporal fidelity of the reconstructed image, verifying the system's capacity to track rapid changes.

ii) Handheld acquisition test, where the reconstruction algorithm was implemented using a live acquisition system, where the camera was handheld and constantly moving. Robustness to camera motion and orientation changes was confirmed by recalculating the homography matrix H for every frame based on the continuously tracked coloured markers. The system's operational envelope was tested by varying the camera's distance, as well as its pitch, roll, and yaw angles relative to Face B, to determine the limits of stable detection and accurate reconstruction. A mobile implementation, using MATLAB Mobile on a smartphone, was also performed to evaluate the system's performance under hardware constraints.

4.3 Results and discussions

4.3.1 Light transmission and privacy behavior

Direct optical observation confirmed the functional difference between the two configurations (Figure 4.5). The parallel arrangement resulted in coherent light channels that allowed the background object's contour (a hand) to be clearly visible, a conventional outcome for parallel fiber composites. Conversely, the random distribution configuration produced a diffuse, unstructured light pattern, although the same object (a hand) was positioned behind the block. Under identical lighting conditions, the background object was rendered indiscernible, confirming that the random fiber arrangement effectively diffuses transmitted light, successfully achieving visual privacy while preserving light transmission. This behavior represents a topological transition from a highly anisotropic network (parallel fibers), characterized by a maximized orientation index along the transmission axis, to a stochastically isotopic network where the lack of structural connectivity correlations disrupts image coherence (D'Amore et al., 2010). This functional divergence establishes a clear and demonstrable control over the transparency-privacy balance through fiber arrangement alone.

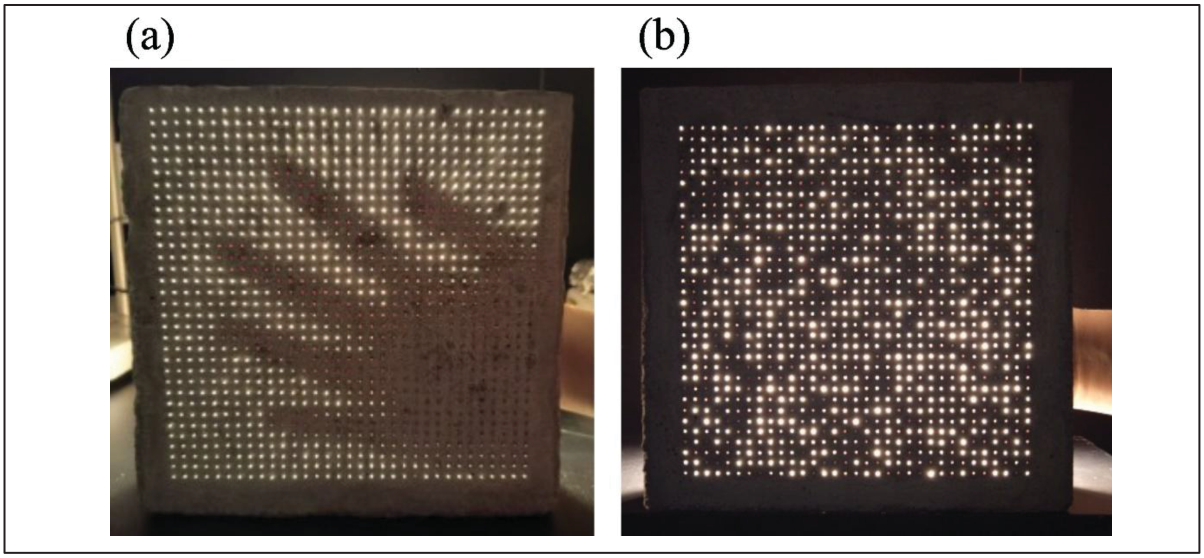

Figure 4.5 Optical response of semi-translucent mortar blocks: (a) parallel fiber configuration showing the visible shape of a hand behind the block, (b) random distribution configuration where the same hand becomes indiscernible

4.3.2 Digital reconstruction of the fiber network

Following the initial observations of light transmission, the optical fiber network in the random distribution specimen was digitally reconstructed based on the recorded input-output mapping. Each fiber’s exit point was identified and associated with its corresponding patch on the surface. These patches were then reassigned according to the virtual reconstruction, producing an ordered image that reveals objects hidden behind the block. As an example, the letters “ÉTS” placed behind the specimen became visible once the network was reconstructed (Figure 4.6). The reconstruction confirmed that, although the physical block diffuses light and conceals shapes, the underlying fiber paths can be computationally realigned to transmit coherent visual information. This functionality can be restricted to authorized users by limiting access to the decoding scheme (i.e., the input-output mapping and related code), while maintaining privacy from external viewers. This establishes a "one-way privacy" functionality in the proposed translucent composite.

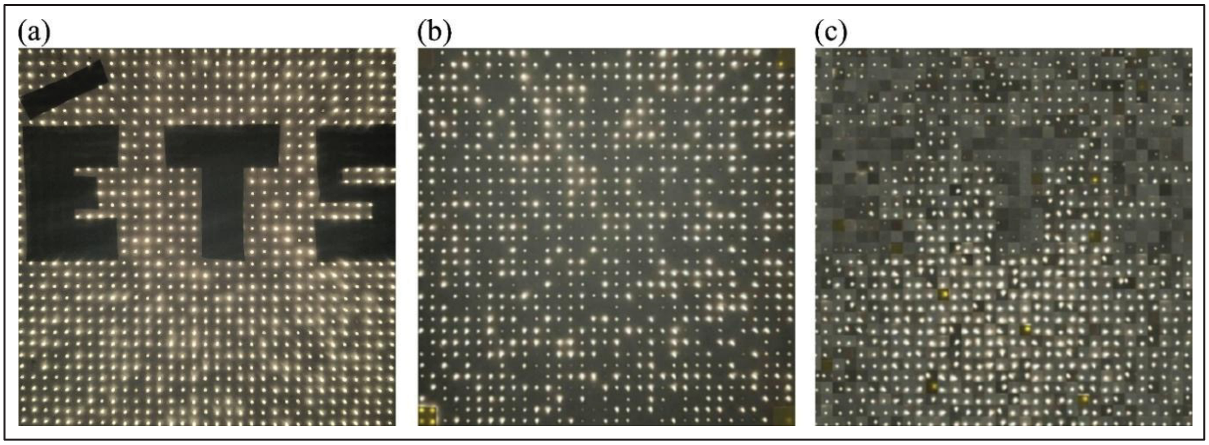

Figure 4.6 Digital reconstruction of the random fiber network revealing hidden letters "ÉTS". (a) Background letters behind the block (face A), (b) view from the block surface (face B) before reconstruction, (c) Face B after digital reconstruction, where letters become clearly discernible

A quantitative analysis of the reconstructed image error (Figure 4.6c) confirms the fidelity of the hidden image retrieval. The reconstruction error (E_{rec}) was calculated by quantifying the number of incorrectly classified fibers relative to the ground truth mask (S_{mask}), in Equation (4.5).

$$E_{rec} = \frac{\sum |S_{rec} - S_{mask}|}{N_{total}} \cdot 100 \tag{4.5}$$

Where N_{total} is the total number of fibers (1089). Specifically, in the "ÉTS" test, the ground truth established that 208 fibers should be classified as masqueraded. The digital reconstruction correctly identified 202 of these fibers as "off", resulting in six misclassified fibers. This analysis yielded a minimal relative pattern error of approximately 2.88% within the dark-fiber subset. This classification error corresponds to a total system error of only 0.55% when normalized by the total fiber count.

This small deviation may result from minor light leakage between neighboring fibers or slight misalignments during the imaging process, or limitations in the digital reconstruction algorithm itself, such as discretization and rounding effects during patch repositioning. Similar to the boundary noise removal strategies employed in high-precision granular reconstruction (Li, Yin, & He, 2025), future iterations of this algorithm could incorporate morphological filtering to further mitigate these discretization artifacts. The slightly uneven or irregular overall alignment observed in Figure 4.6c results from the digital mapping scheme. During the automated mapping process, a quadrangular area was assigned to each individual fiber, which means that not all fibers remained perfectly centered within their assigned region. When these patches are digitally reconstructed, the spacing between neighboring fibers can appear locally wider or narrower. This minor positional distortion does not affect the visual information, as the letters "ÉTS" remain clearly recognizable after processing.

The reconstruction process also highlighted the spatial accuracy of the mapping. Patches (i.e., small image blocks corresponding to individual $n \times n$ "pixel-fibers") were correctly repositioned according to the input-output dataset, confirming that the algorithm preserves the geometric consistency of the fiber network. These results illustrate that the random fiber distribution achieves the intended privacy effect physically, while the digital reconstruction provides a reliable method to selectively recover visual information behind the translucent composite.

The fidelity of the reconstructed images and the effectiveness of the privacy-preserving configuration were assessed by analyzing template-image similarity using NCC. Templates corresponding to the letters "É", "T", and "S" were extracted from the reference image and correlated with the reference, reconstructed, and privacy-preserving images, generating correlation maps (Figure 4.7). The maximum NCC value in each map was recorded as the primary measure of feature similarity.

Table 4.2 summarizes the maximum NCC results. As expected, the reference image shows the highest correlation values, confirming the clear presence of the features and establishing a robust baseline for comparison. In the reconstructed image, the templates were again successfully identified, yielding intermediate NCC scores. These values indicate that the reconstruction partially recovered the structural information corresponding to the templates. The letters are visually recognizable, but the reduced NCC scores reflect the loss of high-frequency fidelity due to minor reconstruction imperfections, such as patch misalignment or quantization effects.

Table 4.2 Maximum NCC Scores for template matching

	E	**T**	**S**
Reference	0.890	0.992	0.994
Reconstructed	0.451	0.606	0.599
Privacy-preserving	0.298	0.380	0.338

Conversely, the privacy-preserving image shows the lowest correlation scores, demonstrating that the templates could not be reliably detected. As observed in the correlation maps, the few localized matches found correspond only to noise artifacts, failing to form recognizable shapes, thus quantitatively confirming the effectiveness of the privacy mechanism. Overall, the NCC analysis successfully separates the partially recovered information in the reconstructed image from the obfuscated and protected features in the privacy-preserving configuration.

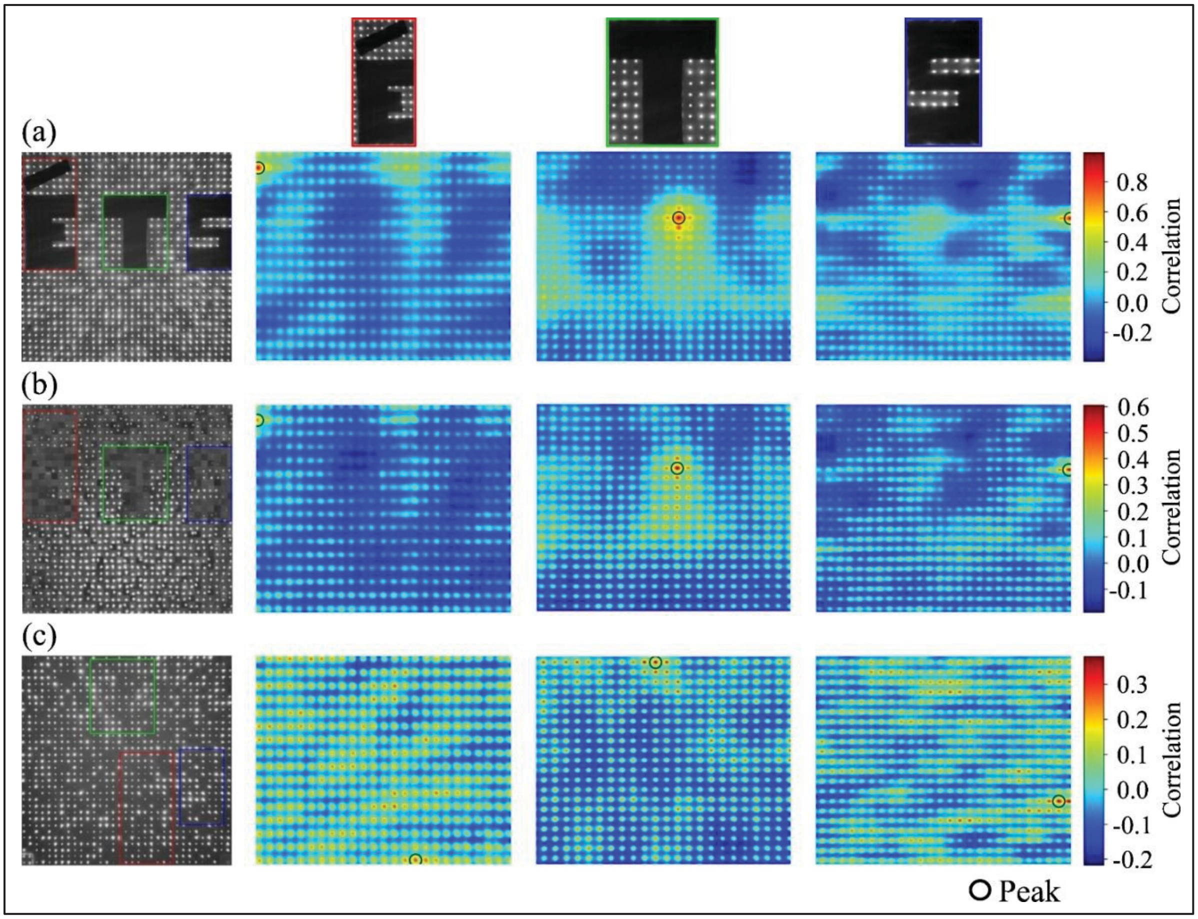

Figure 4.7 NCC maps for template matching across image configurations. The circles highlight the location of the peak correlation. (a) Reference Image. (b) Reconstructed Image. (c) Privacy-Preserving Image. The columns show the correlation maps for templates “E”, “T”, and “S”, respectively

For a quantitative comparison between configurations, we correlated the parallel fiber templates (“É”, “T”, “S”) against the reconstructed random-fiber image (Figure 4.8). The results show that the correlation scores for “T” (0.594) and “S” (0.620) remain similar to those obtained from the reconstructed image (0.606 and 0.599, respectively). This moderate correlation suggests that the reconstruction process, even when targeting a random fiber configuration, retains sufficient generic structural information to allow successful template matching from the parallel configuration.

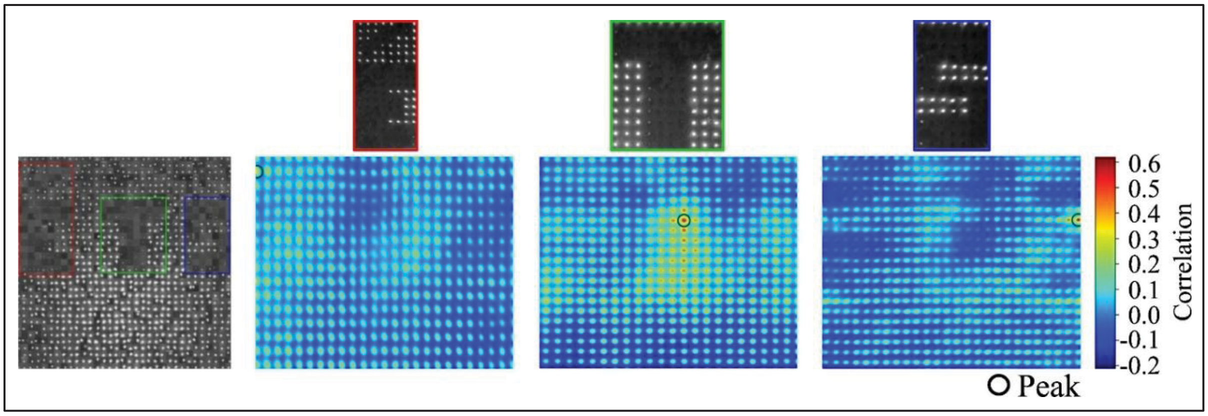

Figure 4.8 NCC analysis for template matching in parallel fibers template with reconstructed configurations

To further assess dynamic performance, a hand was positioned behind the block (face A) and moved from a closed to an open posture in less than half a second. The motion was captured as a video sequence. After digital reconstruction, the opening and closing movements of the hand were clearly recognizable in the reconstructed view of face B (Figure 4.9, static frames shown, full sequence available in Supplementary information). Although individual fibers may exhibit minor misassignments during rapid motion, the overall shape and movement of the hand remain clearly distinguishable, with the dynamic features most evident in the full video sequence. This test demonstrates that the reconstruction algorithm can reassign light patches under rapid motion, confirming the temporal fidelity and spatial accuracy of the method.

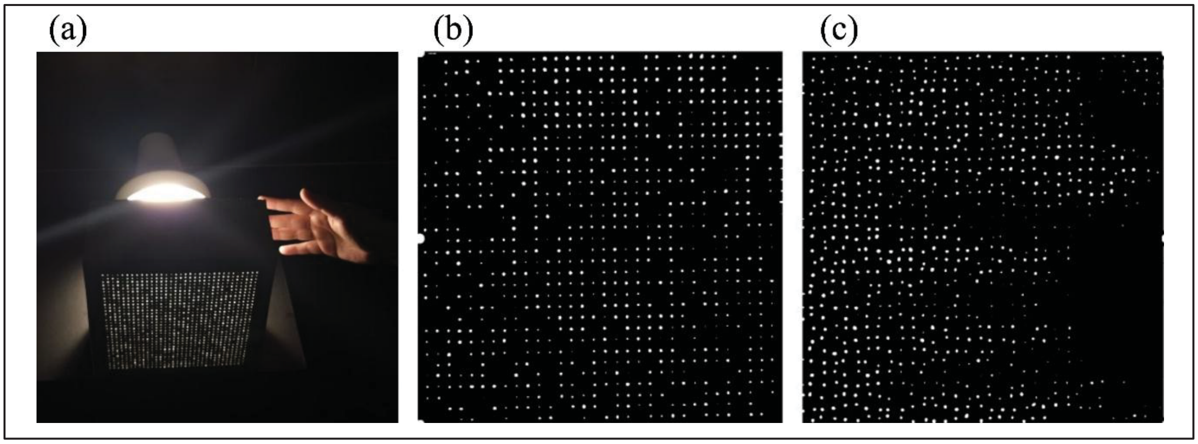

Figure 4.9 (a) Setup and specimen. Binary-converted frames selected from the digital reconstruction of hand movement behind the random-path specimen: (b) view without digital reconstruction, (c) digitally reconstructed frame

It is important to note that the mobile implementation using *MATLAB Mobile* achieved an average processing time of approximately 8 seconds per frame, indicating that the real-time performance is currently limited by the processing power of the handheld device. This latency does not reflect the efficiency of the core algorithm, which remains lightweight, requiring only homography calculation, image segmentation, and a simple pre-calibrated matrix lookup (M) for permutation. This approach differs from 3D reconstruction frameworks that rely on computationally intensive Large Vision Models (Li, Yin, He, et al., 2025) or Optimal Transport (Li, Yin, & He, 2025) algorithms to infer complex internal structures from 2D data. The proposed method employs a pre-calibrated lookup matrix tailored for the fixed optical network, enabling near real-time digital reconstruction of hidden visual information. The observed delay is mainly due to the interpreted research environment and non-optimized cloud communication rather than algorithmic limitations. The *MATLAB Mobile* platform was selected as an easy-to-use development and prototype testing platform for this proof-of-concept study, and allowed for the for rapid algorithm prototyping and testing of the core digital-optical principle (the M vs H correction).

For any practical, real-world application, this processing time can be drastically reduced by porting the reconstruction algorithm to compiled native code (e.g., C++ / OpenCV) and by leveraging on-device GPU acceleration. Overall, the results illustrate that the random fiber distribution achieves the intended privacy effect physically, while digital reconstruction provides a reliable method to selectively recover visual information behind the translucent composite.

4.3.3 Augmented reality visualization and geometric robustness

Building upon the reconstruction process, an augmented-reality reinjection technique was implemented. The reconstructed image was inverse-transformed through the same homography used in calibration and superimposed on the live camera feed. This procedure enabled real-time visualization of the hidden object directly on the surface of the specimen. The reinjection remained stable for moderate camera movements, confirming that the homography maintained geometric consistency within the defined calibration domain. Minor misalignments were occasionally observed near the frame borders due to interpolation artifacts, but overall alignment was preserved. This experiment demonstrated that the random-fiber composite can operate as a physical-digital interface, where hidden information is accessible only through computational decoding and reintegration.

To quantify the functional limits of the system, the spatial and angular dependencies of the calibration stability were analyzed. The system's operational envelope was determined by monitoring the integrity of the marker detection and the accuracy of the homography transformation. First, the angular stability was quantified by testing the camera’s orientation across three axes: roll, pitch, and yaw (Figure 4.10). The system successfully maintained accurate calibration for rotation angles up to approximately ±35° in both pitch and yaw. Beyond these angular limits, the projection error of the markers increased progressively, producing small inaccuracies in the homography estimation and subsequent patch realignment.

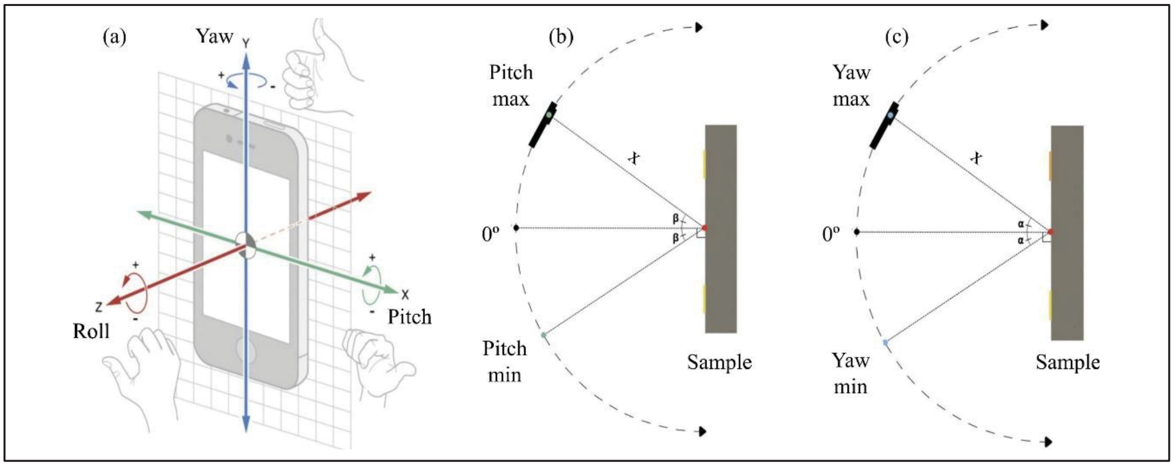

Figure 4.10 Camera orientation and calibration tests: (a) roll, pitch, and yaw relative to the smartphone axes, (b) side view of the yaw test, (c) top view of the pitch test

Subsequently, the viewing distance was tested by varying the camera's position relative to face B, which revealed stable detection and accurate reconstruction for distances ranging from 30 to 110 cm (Figure 4.11). Within this operational range, the mean geometric error remained below 3%, similar to Zeng et al., (2008), ensuring that reconstructed images preserved their correct proportions and spatial correspondence. These tests confirm that the system tolerates moderate camera motion and rotation, which is essential for practical, handheld acquisition. Further optimization of marker design and adaptive homography algorithms could extend this operational range to larger or more complex surfaces (Luo et al., 2023).

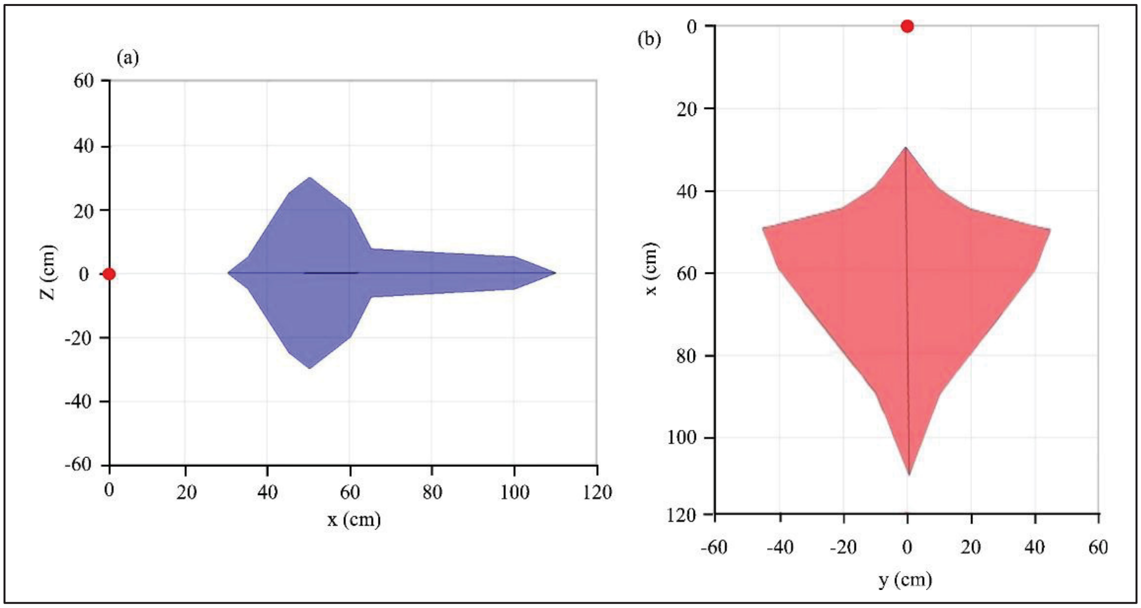

Figure 4.11 Spatial operational limits. Schematic representation of the stable viewing domain. The red circle marks the central axis of the translucent composite

4.4 Conclusions

This study presented the development and experimental validation of a novel cementitious composite that integrates optical privacy and digital recoverability within a single material system. By embedding a traceable, randomly distributed network of optical fibers into an LC3-inspired mortar, the composite effectively diffused light, concealing shapes and achieving visual privacy while maintaining the potential for computational decoding. The core innovation consists of computationally reverse-engineering the light path. Using a pre-recorded input-output mapping matrix and homography-based calibration, a digital algorithm was able to reconstruct coherent images from the diffused light pattern. Validation tests demonstrated the system's robustness in dynamic environments, with stable reconstruction achieved across an operational envelope defined by viewing distances of 30-110 cm and rotation angles up to ±35º (pitch/yaw), maintaining a mean geometric error of less than 3%.

Despite the promising results, some limitations were identified that suggest directions for future work. The current study employed a 33×33 fiber grid (1089 fibers) in a lab-scale specimen, which is sufficient for demonstrating the concept but presents clear challenges for real-world applications. Scaling to larger panels with higher fiber densities introduces significant fabrication complexity and increases the computational load for digital reconstruction. In addition, larger or denser fiber networks may experience increased light attenuation and bending losses, although for typical lengths of a few meters, these effects remain relatively small, with attenuation on the order of 2 dB over 10 m for the fibers used in this study, which is not a limitation in the current application.

From the algorithmic perspective, the current implementation relies on a pre-calibrated lookup matrix and homography-based mapping, which is lightweight but still limited by the processing power of handheld devices. Real-time performance is therefore constrained, and further optimization is necessary to allow fast on-device computation. Minor deviations in patch alignment can also occur due to marker detection errors or environmental variations, which could affect reconstruction fidelity under more dynamic conditions.

To address these challenges and enable larger-scale applications, a modular approach is proposed, in which multiple privacy blocks with independently randomized fiber mappings can be assembled to form larger structures or walls. This strategy allows the benefits of the random fiber configuration to be scaled while maintaining manageable fabrication complexity, ensuring that each module preserves its optical privacy and traceable digital reconstruction. Future work should also explore the optimization of the computational pipeline through migration to compiled native code, adaptive marker detection for enhanced calibration robustness, and strategies to further reduce alignment errors or compensate for environmental influences. Additionally, studies on fiber layout optimization, alternative fiber types, and automated placement techniques could help scale the system while maintaining high fidelity and optical performance.

CONCLUSION

General conclusion

This thesis investigated fiber-optic cementitious composites through three interconnected research axes. These axes addressed optical characterization, mechanical behavior, and functional material design. Their integration allowed the relationships among material composition, fiber configuration, experimental conditions, and the observed responses to be examined within a common framework. The results show that optical transmittance reflects both composite characteristics and measurement configuration. The physically grounded framework developed in this thesis supports consistent detector placement for the specimen geometries and fiber arrangements evaluated. The mechanical analysis showed that the response of the composites is governed by the combined influence of fiber content, geometry, orientation, interfacial condition, loading direction, and matrix properties, with fiber-matrix interaction contributing alongside geometric disruption. Finally, the investigation of random fiber configurations showed that the spatial arrangement of the fibers modifies the transmission of optical information. Under the evaluated conditions, this configuration reduced direct visual recognition while preserving the correspondence required for computational image reconstruction. In summary, these findings provide an integrated basis for the interpretation and design of fiber-optic cementitious composites across optical measurement, mechanical performance, and functional information transfer. The investigated systems demonstrate the feasibility of combining structural, optical, and computational functions within a cementitious composite.

Synthesis of main findings

1. Optical transmittance measurement and interpretation: The results indicate that a substantial part of the variability observed in optical transmittance measurements arises from the experimental configuration in addition to the intrinsic properties of the material. In particular, detector positioning has a direct influence on the measured signal, introducing variations that may mask the material response. The combined experimental and theoretical analysis revealed a nonlinear relationship between detector distance and measured transmittance, with an optimal detection distance identified for the investigated configurations. Based on this behavior, a physically grounded predictive framework was established, relating detector placement to fiber numerical aperture and specimen geometry. These findings help explain inconsistencies reported in the literature and support the development of more reliable and comparable optical characterization methods.

The area-based theoretical transmittance used for comparison serves as a geometric reference for the investigated configurations. The slightly higher values observed for the centered single-fiber configuration are consistent with concentrated beam captured by the finite detector. Similarly, the lower short-distance response of the four-fiber configuration reflects the absence of a central fiber, and the limited overlap of the peripheral light beams near the specimen surface. Within the investigated range, the optical transmittance increased with the number of fibers, and the highest transmittance was obtained for the configuration with the greatest fiber density. The tests therefore support conclusions up to this configuration and defines the fiber-density interval examined in this study. Determining the upper boundary represents a direction for further investigation. The study established detector-placement conditions for the evaluated specimen geometries and fiber arrangements. The upper boundary of fiber density remained outside the experimental scope.

2. Mechanical behavior: The results clarify that the mechanical response of fiber-optic cementitious composites arises from the combined influence of inclusion geometry, fiber-matrix interaction, inclusion density, orientation, and matrix composition. The comparison between specimens containing optical fibers and those containing geometrically equivalent holes separated the contribution of the inclusion material from the geometric discontinuity introduced into the matrix. At selected moderate inclusion levels, embedded fibers maintained or improved compressive strength and, in several configurations, outperformed the corresponding hole specimens, supporting a contribution from fiber-matrix interaction. At the highest investigated inclusion density, the strength generally decreased, indicating that the accumulation of discontinuities progressively offset the contribution associated with the embedded fibers.

Matrix composition influenced the magnitude of this response. The local BSE observations showed differences in fiber-matrix contact and in the morphology of the regions surrounding the holes, providing microstructural context for the distinct behavior of the reference and eco mixtures. The linear-elastic simulations complemented these observations by showing that holes generated more boundary-localized elastic stress fields, whereas fibers produced a more distributed stress pattern within the modeled pre-failure regime. Localized elastic stresses around holes were compatible with maintained or increased specimen-scale strength at selected inclusion levels, emphasizing that local stress distribution and global load-bearing response represent related but distinct aspects of the composite behavior.

Under flexural loading, inclusion orientation produced the clearest variation in mechanical response. Longitudinal inclusions generally preserved or improved strength, whereas transverse arrangements became less favorable as the number of inclusions increased. These results show that the mechanical performance of fiber-optic cementitious composites depends on the coordinated selection of matrix composition, inclusion density, material, and orientation, rather than on fiber content alone.

3. Functional design and controlled information transfer: The results further indicate that fiber configuration influences the spatial organization of the light transmitted through the composite. The proposed random fiber distribution rearranged the spatial correspondence between the input and output positions of the optical fibers, reducing the visual intelligibility of the transmitted scenes under the evaluated conditions. At the same time, the traceability of the fiber network enabled the input images to be reconstructed through the implemented mapping and homography-based procedure. Within the tested geometric envelope, stable reconstruction was maintained for camera distances ranging from 30 to 110 cm and for pitch and yaw rotations of up to approximately ±35°, with a mean geometric error below 3%. These results define the spatial and angular conditions under which the implemented calibration and reconstruction procedure remained stable.

The reconstruction results varied across the evaluated images. Lower performance metrics were observed in reconstructions presenting patch misalignment and quantization artifacts. Patch misalignment was associated with residual errors in homography mapping and patch positioning, which were propagated during resampling. Quantization artifacts arose from the discretization of the continuous fiber output onto the reconstruction grid. Within the implemented processing pipeline, these effects represented the main identified sources of reduced reconstruction fidelity. A systematic sensitivity analysis quantifying their relative contributions represents a direction for extending the present evaluation.

This dual behavior demonstrates the feasibility of using fiber-optic cementitious composites as hybrid physical-digital systems, combining reduced visual intelligibility at the material surface with computational recovery of spatial information under the tested conditions.

These three research axes demonstrate that fiber-optic cementitious composites exhibit configuration-dependent behavior across optical, mechanical, and functional domains. Optical performance depends on fiber characteristics, light distribution, specimen geometry, and measurement conditions. Mechanical performance is influenced by fiber content, geometry, orientation, interfacial condition, and the composition and properties of the cementitious matrix. The combined mechanical, BSE, and numerical results relate inclusion material and matrix composition to local interface morphology, elastic stress distribution, and specimen-scale strength. Functional performance depends on the spatial arrangement of the fiber network and on the correspondence established between its input and output positions. In the random configuration investigated in this thesis, this arrangement reduced direct image recognition while preserving sufficient network traceability for computational reconstruction. Together, these findings connect material composition, fiber architecture, measurement configuration, and computational processing within a common design framework for fiber-optic cementitious composites.

RECOMMENDATIONS

Future research in fiber-optic cementitious composites may focus on the following directions:

- Further investigate and optimize the eco mixture composition by systematically evaluating the proportions and interactions of its constituents to ensure adequate fresh, mechanical, and optical performance.
- Characterize long-term durability under environmental exposure, including moisture, temperature cycling, carbonation, and chemical attack, with emphasis on the evolution of fiber-matrix interfacial integrity and optical transmittance over time.
- Investigate scale effects by analyzing how fabrication constraints at larger dimensions influence fiber positioning, matrix homogeneity, and consistency of optical response, including systems already implemented at architectural scale, where these aspects remain insufficiently characterized.
- Establish relationships between binder chemistry and optical and mechanical performance, particularly in systems incorporating supplementary cementitious materials, geopolymers, or ultra-high-performance matrices, where fiber-matrix compatibility may differ significantly from conventional Portland cement systems.
- Advance standardization of experimental methods for optical transmittance characterization and mechanical testing, to improve reproducibility and enable meaningful comparison across studies, a persistent limitation identified throughout the literature.
- Explore alternative light-guiding technologies, including different fiber materials, diameters, and geometries, as well as non-fiber inclusions such as transparent aggregates or resin rods, to expand the design space and identify better solutions suited to specific optical or structural requirements.
- Develop structural health monitoring applications by exploiting changes in transmitted light patterns as indicators of matrix cracking, fiber debonding, or progressive damage, integrating optical functionality with sensing capability within a single material system.

- Extend the hybrid physical-digital framework toward real-world validation, addressing robustness under varying lighting conditions, transmission distances, and environmental degradation, and exploring applications in embedded sensing networks and material authentication.

ANNEX I

SUMARY OF CONTRIBUTIONS

Journal Articles

- **Arcolezi, K. H.**, Zimmermann C. A., Ung B., Ouellet-Plamondon C. (2026). Experimental and theoretical investigation of optical transmittance in light-transmitting concrete. *Meas. Sci. Technol*. 37 195201. https://doi.org/10.1088/1361-6501/ae6521
- **Arcolezi, K. H.**, Brial, V., Ung, B., Ouellet-Plamondon C. (2026). Mechanical strengthening of cementitious composites by optical fibers through adhesion and geometric disruption. *Manuscript submitted*.
- **Arcolezi, K. H.**, Marion, V., Ung, B., Ouellet-Plamondon C. (2025). Randomly distributed optical fibers in translucent mortar for privacy-preserving light transmission and digital image reconstruction. *Scientific Reports*, 16, 2454. https://doi.org/10.1038/s41598-025-32224-2

Conference Proceedings

- **Arcolezi, K. H.**, Alonso Romero, A., Ben Zaid, H., Hamel, T., Ung, B., Ouellet-Plamondon, C. (2026). Touch-interactive concrete for smart structures. Accepted for publication in *Proceedings of the Canadian Society for Civil Engineering* Annual Conference and presentation. To appear.
- **Arcolezi, K. H.**, Ouellet-Plamondon, C., Ung, B. (2026). Influence of optical fibres on mechanical properties of mortar mixes. In: Billah, A.H.M.M., El Ansary, A. (eds) *Proceedings of the Canadian Society for Civil Engineering Annual Conference 2024*, Volume 4. CSCE 2024. Lecture Notes in Civil Engineering, vol 717. Springer, Cham. https://doi.org/10.1007/978-3-031-98775-5_23
- **Arcolezi, K. H.**, Ouellet-Plamondon, C., Ung, B. (2025). Interactive light- and sound-sensitive mortar for architectural environments. In: Francis, A., Miresco, E., Melhado, S. (eds). *Advances in Information Technology in Civil and Building Engineering*. ICCCBE 2024. Lecture Notes in Civil Engineering, vol. 629. Springer, Cham. https://doi.org/10.1007/978-3-031-87364-5_41

PRESENTATIONS
Oral Presentations

- Touch-interactive concrete for smart structures. Oral presentation scheduled at the Canadian Society for Civil Engineering Annual Conference, June 2026.

- Interactive light- and sound-sensitive mortar for architectural environments. Oral presentation at the International Conference on Computing in Civil and Building Engineering (*ICCCBE*) 2024.
- Influence of optical fibres on the mechanical properties of mortar mixes. Oral presentation at the Canadian Society for Civil Engineering Annual Conference (*CSCE*) 2024.

Poster Presentation

- *Optical fiber-embedded smart concrete for sensing and illumination*. Poster presentation at the 36th COPL Annual Conference, 2025.

Artistic Exhibition

- From Quantum Science to Artistic Experience, by the *INTRIGO Collective*, at Amos Exhibition Centre, Amos - QC, 2025.

ANNEX II

FUNDING, AWARDS AND DISTINCTIONS

Scholarships and Fellowships

- École de technologie supérieure, Montréal, Canada. Doctoral Scholarship, 2022–2026.
- Fonds de recherche du Québec – Nature and Technologies. Merit Scholarship Program for Foreign Students (PBEEE), 2025–2026.

Awards and Distinctions

- Association canadienne-française pour l'avancement des sciences (Acfas) - Research photo contest, La preuve par l'image, image selected among the 20 featured works, Biodôme Montréal, 2026. [https://www.acfas.ca/prix-concours/preuve-image/laureats]
- École de technologie supérieure, Montréal, Canada. Photo contest, Art and Culture Category, Winner, 2025.
- Natural Sciences and Engineering Research Council of Canada (NSERC). Research photo contest, Jury Prize, Science Exposed, 2024. [https://nserc-crsng.canada.ca/en/science-exposed/2024-science-exposed-finalists]

Research support

École de technologie supérieure. Financial support for the dissemination and promotion of research work, 2024 and 2026.

APPENDIX A

TOUCH-INTERACTIVE CONCRETE FOR SMART STRUCTURES

Article accepted for publication and presentation at the Canadian Society of Civil Engineering annual conference proceedings, Quebec City, June 2026

Abstract

Concrete integrating optical fibres has been investigated as a multifunctional material capable of combining light transmission and sensing-related modalities. In this context, this study investigates a touch-interactive concrete system based on embedded plastic optical fibres coupled with a compact optoelectronic detection and signal-processing architecture. Cubic cementitious composite samples (50 mm) were prepared using an LC^3-inspired cementitious matrix incorporating four polymethylmethacrylate fibres, enabling light transmission, single-point touch detection, and basic directional interaction. The sensing mechanism relies on intensity-based Fresnel reflection at the exposed fibre-air interface, where physical contact alters the refractive index' contrast and modulates the back-reflected light intensity. A custom-printed circuit board incorporating a transimpedance amplifier and a low-pass filter was used to condition the photodiode signal, improving the signal-to-noise ratio from 9.5 dB to 22.6 dB. Touch events were identified using a finite state machine implemented in LabVIEW, comprising listening, pre-confirmation, confirmation, and dead time states, which enabled reliable discrimination between intentional interactions and transient noise. Directional gestures were interpreted from the temporal sequence of fibre activations within a defined 1-second time window, allowing recognition of horizontal, vertical, and diagonal swipe-like movements. Experimental results demonstrate stable single-touch detection and a directional recognition success rate of 92%. The results demonstrate the feasibility of implementing tactile interactivity in cement-based materials by integrating optical fibres, optoelectronic conditioning, and structured signal processing.

A.1 Introduction

The incorporation of optical fibres into cementitious materials has been widely investigated, especially in the context of structural health monitoring and sensing applications in civil engineering. Fibre-optic techniques, such as fibre Bragg gratings, distributed optical sensing, and intensity-based measurements have been employed to monitor strain, temperature, cracking, and damage in concrete structures, benefiting from their durability, electromagnetic immunity, and long-term stability in harsh environments (Leung et al., 2015; Makul, 2020; Qiao et al., 2023; Taheri, 2019; Theodosiou & Kalli, 2020; Wang, Li, Hao, Sai, & Liu, 2022).

In parallel, optical fibres have also been embedded in concrete for light-transmission purposes, resulting in the development of translucent concrete elements explored for architectural and functional applications. Previous studies have examined fibre material, geometry, and distribution, showing that guided light transmission can be achieved without significant degradation of mechanical performance when properly designed (Chiew, Ibrahim, Mohd Ariffin, et al., 2020; Henriques et al., 2020; Huynh Phuong Nam et al., 2022; Rong et al., 2023; Sharifi et al., 2023b; Sobo, Farooq, & Azhar, 2021). In most of these investigations, however, optical fibres are used as passive components, and the transmitted or reflected light is generally not explored for interactive or responsive behaviour (Inaudi et al., 2005).

In a broader context of smart materials, increasing attention has been directed toward intelligent materials, human-computer interaction, and immersive technologies such as virtual and augmented reality, which emphasize dynamic interaction between users and their surrounding environment (Hapenciuc, Banescu, & Mihai, 2016; Hirsch, Rossmy, & Butz, 2021; Larsen, 2015; Salvador-Herranz, Contero, & Camba, n.d.; Schöning et al., 2009). Extending these concepts to the built environment raises the question of whether traditionally inert construction materials can be adapted to support interactive capabilities. Within this perspective, optical fibres embedded in concrete offer a potential pathway for enabling tactile interaction through optoelectronic mechanisms. One such mechanism relies on Fresnel reflection at the fibre-air interface, where variations in the refractive index induced by physical contact result in measurable changes in back-reflected light intensity. Although Fresnel-based sensing principles are well established in optics, their implementation in cementitious materials remains limited, due to optical attenuation in dense matrices and the reliance on complex or high-cost interrogation equipment (Zhang et al., 2024; Zhao, Li, Zhang, Zhang, & Jin, 2013).

Interactive concrete can present a variety of sensing and feedback properties depending on the embedded components and intended application. Embedded sensors can detect touch, temperature, sound, or proximity, providing real-time feedback or structural health monitoring (Beesley, 2010). Touch interaction can trigger visual or auditory responses, such as lighting changes or sound generation, enabling responsive pavements, interactive facades, or playful architectural surfaces (Hirsch et al., 2021). Optical fibres in particular allow light-transmitting concrete to illuminate or change colour in response to environmental conditions, combining aesthetic and functional interactivity. In addition, surface coatings with reactive materials can further extend functionality, enabling interactions with environmental factors such as pollution or facilitating self-cleaning behaviours (Hunger & Brouwers, 2009). These examples demonstrate the versatility of interactive concrete as both a sensory medium and an interface for human-environment engagement.

Within this context, the present study investigates a touch-interactive concrete system based on optical fibres embedded into concrete and coupled to a compact optoelectronic detection unit. A four-fibre configuration is adopted to enable both localized touch detection and directional interaction across the concrete surface. By combining Fresnel-reflection-based sensing with dedicated analogue signal conditioning and a finite state machine framework for event validation, this work explores a practical and scalable approach to introducing tactile interactivity into cementitious materials, contributing to ongoing efforts to integrate sensing and interaction capabilities into the built environment.

A.2 Materials and methods

A.2.1 Smart touch-interactive concrete preparation

The smart touch-interactive concrete was prepared using a composite mortar matrix consisting of general use (GU) Portland cement (CSA A3000 compliant), calcined clay (CC), limestone filler (LF), natural sand (Sa), and a polycarboxylate-based superplasticizer (SP). This blend forms an LC^3-inspired binder system (Limestone Calcined Clay Cement). The mix design adhered to a water-to-binder ratio of 0.392, ensuring both adequate workability and mechanical performance, as per ASTM C109 standards (Jin et al. 2025; Scrivener et al. 2018). Table AI-1 presents the specific proportions of the components. Mixing procedures followed ASTM C305, using a mechanical mixer to achieve a homogeneous dispersion of all components. The fresh mixture was cast into 5 cm cubic molds, with plastic optical fibres embedded before casting. The tips of the polymethylmethacrylate (PMMA) fibres were positioned at the sample's surface to allow tactile interaction. The fibres had a 1 mm core diameter, a refractive index of 1.49, a step-index profile, and a numerical aperture of 0.5, promoting efficient light coupling and transmission with minimal attenuation of <0.002 dB/cm at 650 nm (Romero et al. 2023).

Table-A II-1 Composition and properties of the composite material

GU	CC	LF	Sa	Water	SP	Flow*	Density	Compressive strength**
kg/m³						%	kg/m³	MPa
390	162.5	97.5	1310	255	7	144	2234	63 ± 0.6

*Measured as per ASTM C1437-20
**Average of three samples as per ASTM C109-21

The preparation and finishing of the exposed fibre tips were controlled to ensure consistent tactile interaction and optical response. After demolding and curing, the fibre ends were trimmed using a standard fibre cutter and lightly polished with 400-grit abrasive paper. This procedure was applied solely to remove surface irregularities and ensure that the fibre tips were flush with the concrete surface, without intentional protrusion or recess, resulting in a smooth and continuous surface texture when contacted by the user's hand. After casting, the specimens were demolded after 24 hours and placed in a curing chamber maintained at 23 ± 2 °C and relative humidity greater than 95%, in accordance with ASTM C109. After 28 days of curing, compressive strength testing was performed on three specimens from each batch. An average strength of approximately 63 MPa was recorded. Additional samples were set aside for touch interactivity testing and sensor integration.

A.2.2 Optoelectronic system and detection component

The interactive behaviour of the smart concrete is enabled by a compact optoelectronic system in which optical fibres operate as waveguides for both forward-propagating and back-reflected light. Light is injected into the fibre and guided through the concrete matrix, while a portion of the signal reflected at the exposed fibre end is collected for detection. The sensing mechanism is governed by Fresnel reflection at the fibre air interface, where changes in the optical boundary condition caused by physical contact lead to measurable variations in the back-reflected light intensity.

For normal incidence, the Fresnel reflectance (R) at the interface between two media with refractive indices n_1 and n_2 can be expressed as Equation-A II-1, where n_1 denotes the refractive index of the optical fibre core and n_2 represents the refractive index of the external medium in direct contact with the exposed fibre end (e.g., air, $n_2 = 1.0$; human skin, $n_2 \cong 1.4\text{-}1.5$). For air, the reflectance is approximately 3.9%, while for human skin it drops to around 0.2%. Although the refractive index of skin may vary depending on factors such as moisture, pressure, and contact area, this order-of-magnitude reduction in reflectance consistently results in a pronounced attenuation of the back-reflected signal. This decrease in Fresnel reflectance explains the substantial reduction in the detected optical intensity upon touch, in agreement with the experimentally observed voltage drop at the photodiode output.

$$R = \left(\frac{n_1 - n_2}{n_1 + n_2}\right)^2 \tag{A II-1}$$

In the absence of interaction, the fibre tip is surrounded by air, and the refractive index contrast between the fibre core and air results in a relatively stable reflected signal. When the exposed fibre end is touched or obstructed, the effective refractive index at the interface increases, reducing the reflectance and consequently attenuating the intensity of the light returned to the detector. This modulation of the reflected signal forms the basis of the touch sensitive response of the system.

A Rohm RLD63NPC8 optoelectronic module was employed as the light source and detector. This integrated device combines a red laser diode emitting at a wavelength of 635 nm with an optical output power of 24 mW, along with an internal monitoring photodiode, all within a single package. The integrated configuration minimizes optical alignment sensitivity and supports compact system integration, which is advantageous for embedded and scalable implementations. The weak photocurrent generated by the photodiode is conditioned using a custom-printed circuit board (PCB) designed in KiCad. Signal conditioning begins with a transimpedance amplifier (TIA) based on the LTC6268, which converts the photodiode current into a voltage signal and increases its amplitude (Potet et al., 2025). The output is subsequently filtered using a low-pass filter implemented with a TL081 operational amplifier, featuring a cut-off frequency of approximately 60 Hz and a gain of 1.5. The cut-off frequency was selected to effectively suppress power-line-related interference and high-frequency electrical noise while preserving the temporal characteristics of human touch interactions, which typically occur at frequencies below 10 Hz. This filtering stage attenuates high-frequency electrical noise and stabilizes the signal for reliable detection.

The conditioned analogue voltage is acquired using a National Instruments USB 6002 data acquisition system with a sampling rate of 1 kHz. The recorded data enable real-time monitoring and quantitative evaluation of light intensity variations induced by physical interaction with the optical fibre, thereby allowing assessment of the interactive performance of the concrete system. An overview of the system architecture is provided in Figure-A II-1, which illustrates the interaction between the embedded optical fibres and the optoelectronic module. The figure conceptually represents the optical response of the fibre under different interaction conditions, highlighting the contrast between unperturbed light transmission and the attenuation caused by direct physical contact at the exposed fibre end. It also presents the internal signal detection pathway within the optoelectronic device, offering a visual reference for the main functional elements involved in light emission, detection, and signal conditioning.

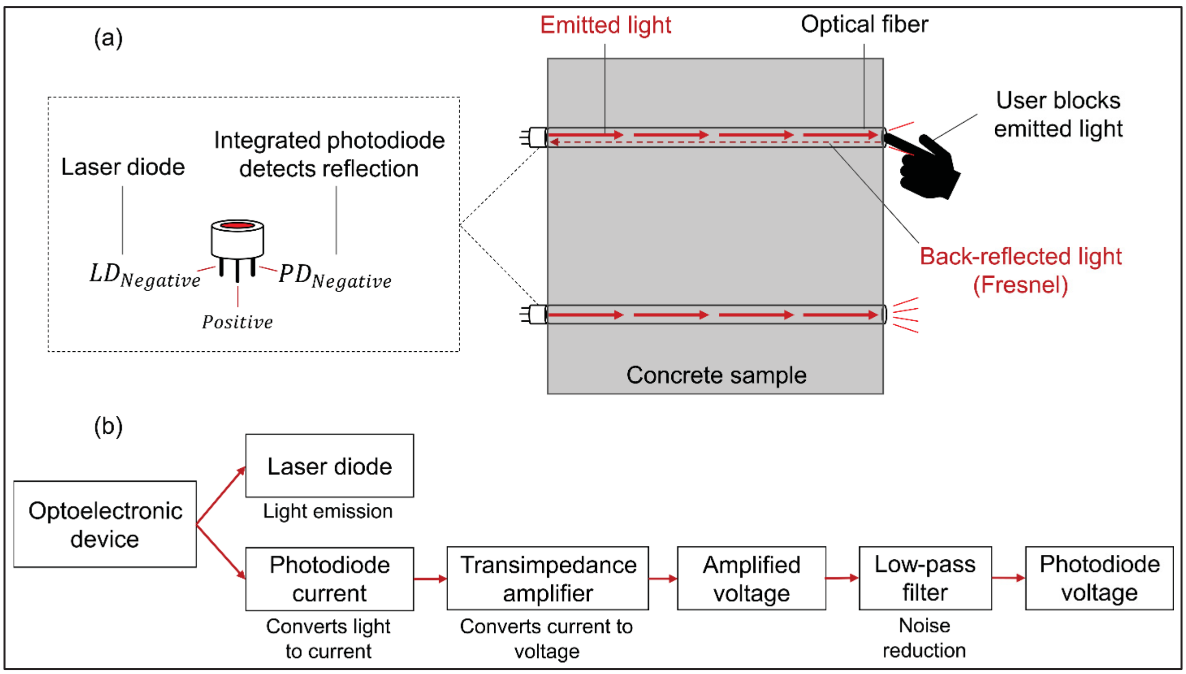

Figure-A II-1 Schematic representation of the interactive smart concrete system. (a) Optical fibre embedded in the concrete, illustrating light transmission in both the absence and presence of physical interaction at the exposed fibre end. (b) Simplified electronic stages of the optoelectronic module

A.2.3 Touch-responsive testing and signal processing

The touch-responsive behaviour of the smart concrete system was evaluated through controlled cyclic interaction tests designed to reproduce typical usage conditions. Each test consisted of alternating interaction and non-interaction phases and was repeated over multiple cycles to assess the repeatability and temporal stability of the system response. All tests were performed on a specimen incorporating four embedded optical fibres, each individually connected to the optoelectronic detection system and treated as an independent sensing channel. This configuration enabled both single-point touch detection and the evaluation of directional interactions, including horizontal, vertical, and diagonal movements across the concrete surface.

To examine the robustness of the setup, experiments were conducted under different ambient lighting conditions, including tests performed with room lighting on and with lights turned off. This approach allowed verification that the optoelectronic configuration and signal conditioning stages were sufficiently insulated from external light interference. Because the sensing mechanism relies on back-reflected light within the fibre rather than ambient illumination, no measurable influence of external lighting was observed. The passive low-pass filter further contributed to signal stability by attenuating high-frequency noise and limiting the influence of environmental fluctuations. The complete experimental arrangement, including the concrete sample and the optoelectronic circuitry, is shown in Figure-A II-2.

The reliability of the tactile interface is quantified by the signal-to-noise ratio (SNR), which determines the system's ability to distinguish a legitimate touch event from the electromechanical noise floor. The SNR, expressed in decibels (dB), is calculated using the following Equation-A II-2.

$$SNR = 20 \cdot \log_{10} \frac{V_{Signal}}{V_{Noise}} \tag{A II-2}$$

Where V_{Signal} represents the mean voltage drop amplitude during a confirmed interaction phase, and V_{Noise} represents the standard deviation (or peak-to-peak amplitude) of the voltage during the idle "listening" state. A high SNR is essential for the finite state machine (FSM) to operate without false positives or missed triggers. The system response was characterized by monitoring variations in the conditioned output voltage during interaction phases. Signal amplitude and temporal behaviour were analyzed to evaluate sensitivity to touch, response time, and potential signal drift over repeated interaction cycles. These measurements enabled assessment of both short-term responsiveness and consistency under repeated use. Signal interpretation and event detection were performed using a custom application developed in LabVIEW, which served as the central processing and visualization platform. Given the presence of electrical and mechanical noise inherent to concrete-based systems, the software architecture was designed to reliably discriminate intentional touch events from transient disturbances.

Touch detection was implemented using a finite state machine framework, which processes the voltage signal from each of the four fibre channels through four sequential states, as presented in Figure-A II-2.

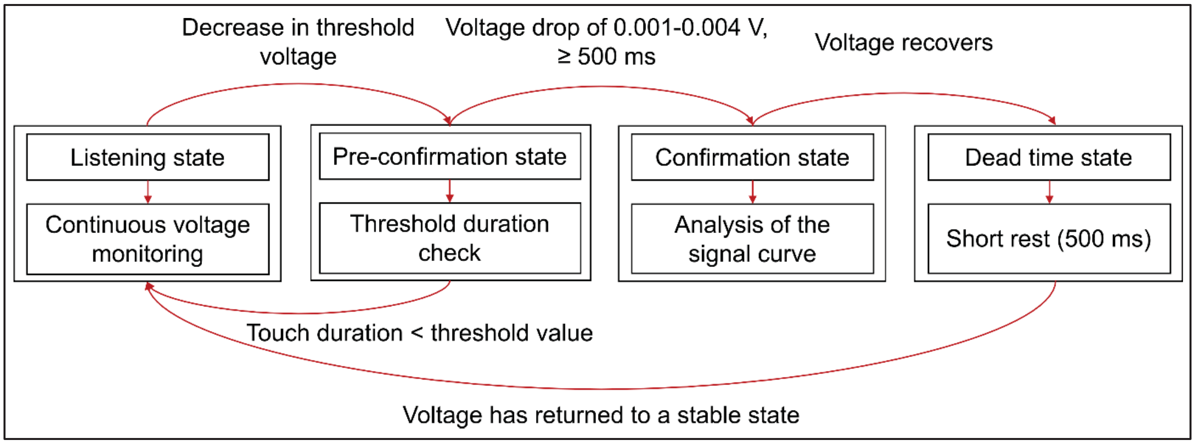

Figure-A II-2 Experimental setup for touch-responsive testing of the smart concrete system

In the “listening” state, the system continuously monitors the baseline voltage of each photodiode to detect significant deviations indicative of a potential touch. Upon detecting a threshold breach, the system enters the “pre-confirmation” state, applying a time-based filter to reject transient noise by ensuring the signal persists for at least 500 milliseconds and exhibits a slope consistent with normal human interaction. This duration was selected based on typical human touch dynamics, which occur on time scales longer than electrical transients. If these criteria are met, the “confirmation” state validates the event as a true touch by analyzing the signal’s shape, duration, and stability. Following confirmation, a “dead time” state of 500 milliseconds is enforced to prevent multiple triggers from a single contact and allow the system to return to a stable baseline.

In addition to single-point touch detection, the software implements a directional movement algorithm that interprets the temporal sequence of activations across the four embedded fibres. A directional gesture is registered when two fibres are triggered in a predefined spatial order within a maximum time window of 1-second. This temporal window was chosen to balance user interaction flexibility with reliable discrimination between sequential gestures and independent touch events. This method allowed recognition of horizontal (43, 34, 12, 21), vertical (23, 32, 14, 41), and diagonal (42, 24, 13, 31) swipe-like interactions across the concrete surface, with the numbered vectors in parentheses representing the corresponding events (Figure-A II-3).

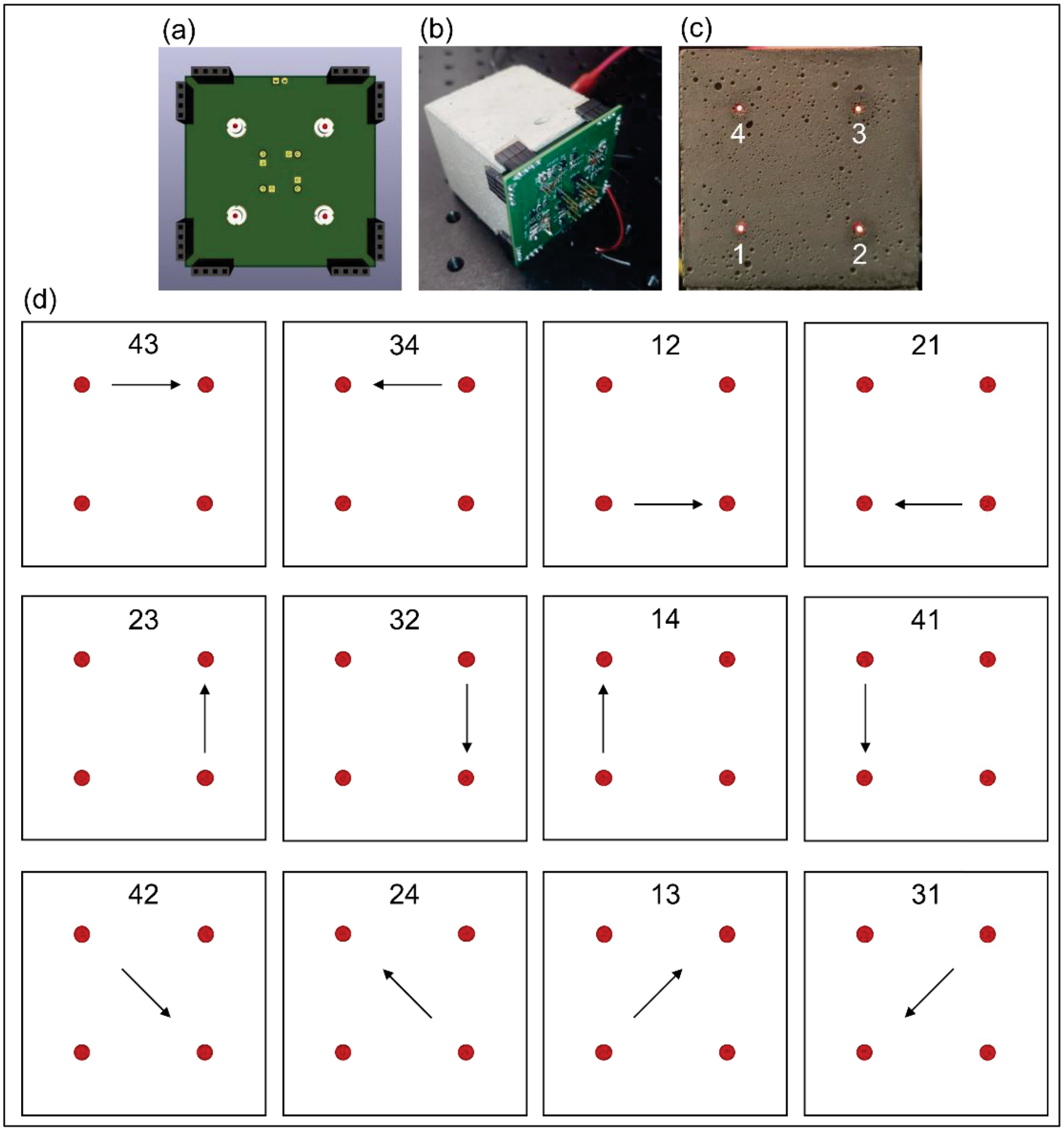

Figure-A II-3 Experimental and algorithmic framework: (a) design of the PCB for signal conditioning, (b) optoelectronic unit attached to the concrete specimen, (c) concrete specimen illuminated with the fibres and detection codes, and (d) movement-code correspondence

A.3 Materials and methods

A.3.1 Smart touch-interactive concrete preparation

The detection capability of the smart concrete system is closely dependent on the quality of the optoelectronic signal. Figure-A II-4 presents the typical voltage response obtained from a single optical fibre embedded in the concrete during repeated tactile interaction and release. The signal exhibits a reproducible voltage decrease upon contact, followed by a recovery after release. While the interaction is identifiable, the raw response shows low-frequency fluctuations and non-instantaneous transitions. These characteristics are consistent with typical human touch interactions and highlight the challenges of processing unconditioned optoelectronic signals within a dense concrete matrix.

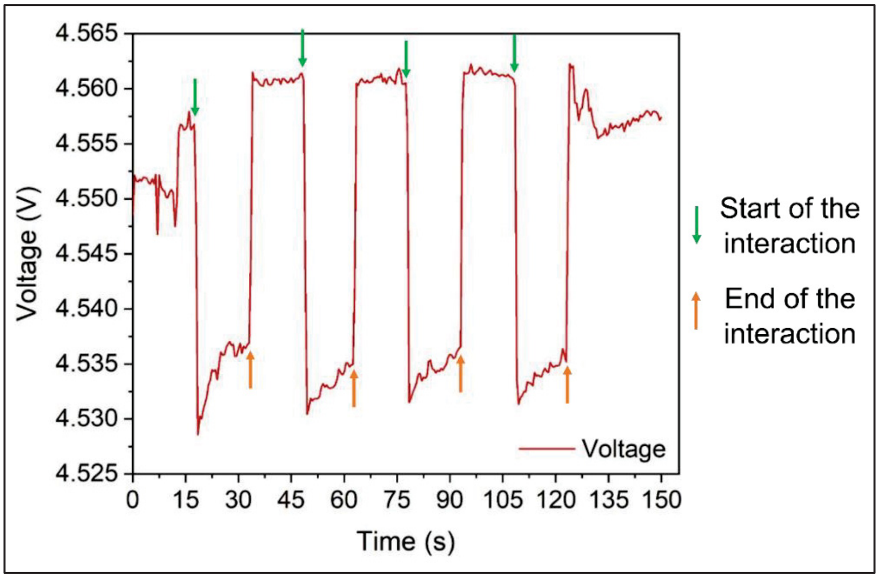

Figure-A II-4 Voltage response of the photodiode during tactile interaction. The clear voltage drop distinguishes the touch event from the baseline

Initial characterization of the raw signal, measured directly from the photodiode without conditioning, highlighted the severity of signal attenuation within the concrete matrix. The photocurrent variation observed between the "touch" state and the "idle" state was approximately 3 µA. This minute variation was heavily compromised by background electrical noise, estimated at 1 µA, resulting in a low SNR of 9.5 dB. At this signal quality level, reliable discrimination between intentional interaction and random fluctuations was not achievable.

To overcome these limitations, a custom-printed circuit board (PCB) was designed, integrating a transimpedance amplifier (TIA) and a second-order active low-pass filter with a 60 Hz cutoff frequency. The TIA converts the low-level photocurrent into a proportional voltage signal suitable for digital processing, while the filter suppressed high-frequency interference, including power-line noise and transient switching artifacts, stabilizing the noise floor to approximately 2 mV. Simultaneously, the amplification stage increased the voltage variation associated with touch events to 27 mV. As a result, the SNR improved from 9.5 dB to 22.6 dB, representing an enhancement of over 13 dB. With this improvement, the conditioned signal exhibits distinct and repeatable voltage transitions, providing a stable input for the subsequent finite state machine without generating false positives under idle conditions.

A.3.2 Touch and movement detection performance

The performance of the proposed sensing system was evaluated by processing the conditioned signals from four embedded optical fibres using the developed LabVIEW-based algorithm. The analysis focused on two aspects: the reliability of single-touch detection and the accuracy of directional movement recognition. Stable touch detection required not only electronic conditioning but also structured digital processing. Although signal conditioning substantially reduced electrical noise, residual transient fluctuations were still present in the voltage signal. As established in the FSM framework, the system relies on the temporal validation of signals. While signal conditioning significantly improved the SNR, the implementation of the Pre-confirmation state, requiring the voltage drop to persist for a minimum duration of 500 ms (ΔV cutoff) was the critical factor in suppressing residual transient fluctuations. This programmed logic ensured that only intentional human interactions were recorded, effectively eliminating false positives from environmental electrical noise.

Following event validation, a dead time state of 500 ms is enforced to prevent sustained contact from being interpreted as multiple consecutive inputs, ensuring that each physical interaction produces a single digital event. The sequential progression through listening, pre-confirmation, confirmation, and dead time states demonstrates that digital logic plays a complementary role to analog conditioning in achieving reliable tactile sensing. Beyond single-touch detection, the system was evaluated for its ability to recognize directional movements across the concrete surface. Directional gestures are identified by analyzing the temporal sequence of activations among the four embedded fibres. When two fibres are triggered in a predefined spatial order within a maximum time window of 1 s, the algorithm registers a movement vector (horizontal, vertical, or diagonal) and displays the corresponding direction on the user interface (Figure-A II-5).

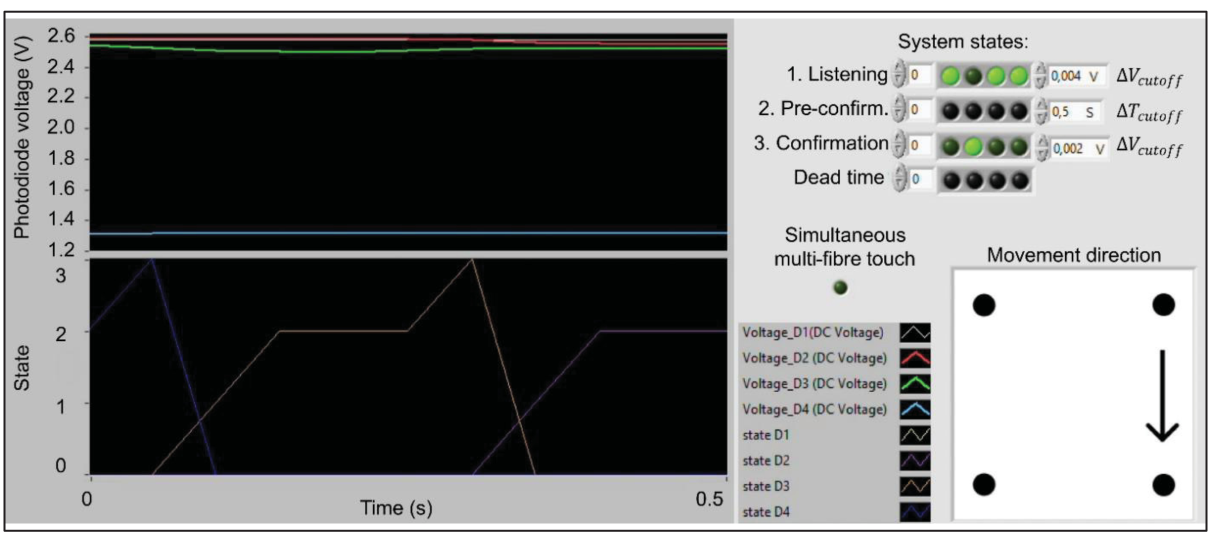

Figure-A II-5 LabVIEW interface used for directional movement detection, illustrating real-time visualization of fibre activation and recognized gesture direction

Experimental trials resulted in a movement detection success rate of 92% over 50 interaction trials. Successful detections correctly identified both the activated fibre pair and the associated movement direction. The remaining 8% of unsuccessful cases were primarily associated with two algorithmic constraints. First, gestures performed more slowly than the predefined temporal window were interpreted as independent touch events rather than continuous movements. Second, simultaneous activation of multiple fibres is intentionally rejected to avoid ambiguous directional interpretation, requiring gestures to be performed sequentially rather than as overlapping contacts. These results indicate that the proposed system reliably detects deliberate, sequential touch and swipe interactions within a constrained temporal framework. While the current algorithm imposes constraints on user input timing and sequence, it provides a consistent and interpretable response suitable for touch-interactive concrete interfaces.

A.4 Conclusions

This study demonstrates the integration of an optoelectronic sensing architecture into a cementitious composite, enabling touch-responsive and directional interaction capabilities. By exploiting Fresnel reflection at exposed plastic optical fibre tips and combining analogue signal conditioning with structured digital processing, the proposed system achieves reliable tactile detection within a dense concrete matrix illuminated through embedded optical fibers coupled to laser diodes. Analogue amplification and low-pass filtering improved the signal-to-noise ratio from 9.5 dB to 22.6 dB, enabling stable discrimination between intentional touch events and background noise. The implementation of a finite state machine further enhanced detection reliability by introducing temporal validation and event sequencing. Directional gesture recognition based on the temporal order of fibre activation achieved a success rate of 92% under controlled interaction conditions. While the current implementation is limited by interaction speed constraints, manual threshold calibration, and a modest number of sensing points, the results demonstrate the feasibility of Fresnel-reflection-based tactile sensing in cementitious materials using compact and low-cost optoelectronic components. Future work will focus on increasing sensing density, developing self-adaptive calibration algorithms to compensate for environmental variability, and evaluating long-term durability under realistic service conditions. Overall, the findings support the potential of optically enabled interactive concrete as a functional interface material, complementing ongoing efforts to integrate sensing and interaction capabilities into smart and responsive built environments.

LIST OF BIBLIOGRAPHICAL REFERENCES

Ahuja, A., & Mosalam, K. M. (2017). Evaluating energy consumption saving from translucent concrete building envelope. *Energy and Buildings*, *153*, 448–460. https://doi.org/10.1016/j.enbuild.2017.06.062

Akeed, M. H., Qaidi, S., Ahmed, H. U., Emad, W., Faraj, R. H., Mohammed, A. S., … Azevedo, A. R. G. (2022). Ultra-high-performance fiber-reinforced concrete. Part III: Fresh and hardened properties. *Case Studies in Construction Materials*, *17*, e01265. https://doi.org/10.1016/j.cscm.2022.e01265

Alghamdi, H., Shoukry, H., Abadel, A. A., & Khawaji, M. (2023). Performance assessment of limestone calcined clay cement (LC3)-Based lightweight green mortars incorporating recycled waste aggregate. *Journal of Materials Research and Technology*, *23*, 2065–2074. https://doi.org/10.1016/j.jmrt.2023.01.133

Alonso Romero, A., Amouzou, K. N., Sengupta, D., Zimmermann, C. A., Richard-Denis, A., Mac-Thiong, J.-M., … Ung, B. (2023). Optoelectronic Pressure Sensor Based on the Bending Loss of Plastic Optical Fibers Embedded in Stretchable Polydimethylsiloxane. *Sensors*, *23*(6), 3322. https://doi.org/10.3390/s23063322

Al-Sodani, K. A. A. (2025). Production, Thermal, Durability, and Mechanical Properties of Translucent Concrete and Its Applications in Sustainable Construction: A Review. *Buildings*, *15*(18), 3314. https://doi.org/10.3390/buildings15183314

Altlomate, A., Alatshan, F., Mashiri, F., & Jadan, M. (2016). Experimental study of light-transmitting concrete. *International Journal of Sustainable Building Technology and Urban Development*, *7628*(December), 1–7. https://doi.org/10.1080/2093761X.2016.1237396

Ambali, D. P. P. P., Lolo, J. A., Handyaningtyas, G. M., Tasik, G. K., & Goran, H. K. (2023). Compressive Strength and Light Transmission of Translucent Concrete by Using Optical Fiber. *JTERA (Jurnal Teknologi Rekayasa)*, *8*(2), 247. https://doi.org/10.31544/jtera.v8.i2.2023.247-254

Anmeeganathan, S. R., Ravichandran, T., & Subramanian, S. (2018). *FINITE ELEMENT ANALYSIS ON FLEXURAL STRENGTH OF HIGH STRENGTH RUBBERIZED CONCRETE*. *9*(11), 990–996.

Antony Samy, L. M., Ayyanar, D., Ganesan, K., Singamuthu, N., & Veeriah, R. (2025). LUMINANCE AND STRENGTH CHARACTERISTICS OF TRANSLUCENT CONCRETE FOR SUSTAINABLE DEVELOPMENT. *Suranaree Journal of Science and Technology*, *32*(5), 010367(1-8). https://doi.org/10.55766/sujst7604

Arcolezi, K. H., Brial, V., Ung, B., & Ouellet-Plamondon, C. M. (2026). Mechanical strengthening of cementitious composites by optical fibers through adhesion and geometric disruption. *Submitted*.

Arcolezi, K. H., Claudiane Ouellet-Plamondon, & Bora Ung. (2024). Interactive Light and Sound-Sensitive Mortar for Architectural Environments. *Advances in Information Technology in Civil and Building Engineering*, *2*, 489–497. Montreal, Canada: Springer Nature Link. https://doi.org/https://doi.org10.1007978-3-031-87364-5_41

Arcolezi, K. H., Marion, V., Ung, B., & Ouellet-Plamondon, C. (2025). Randomly distributed optical fibers in translucent mortar for privacy-preserving light transmission and digital image reconstruction. *Scientific Reports*, *16*(1), 2454. https://doi.org/10.1038/s41598-025-32224-2

Arcolezi, K. H., Ung, B., & Ouellet-Plamondon, C. (2026). Influence of Optical Fibres on Mechanical Properties of Mortar Mixes. In: Billah, A.H.M.M., El Ansary, A. (eds) *Proceedings of the Canadian Society for Civil Engineering Annual Conference 2024*, Volume 4. CSCE 2024. Lecture Notes in Civil Engineering, vol 717. Springer, Cham. https://doi.org/10.1007/978-3-031-98775-5_23

Arcolezi, K. H., Zimmermann, C. A., Ung, B., & Ouellet-Plamondon, C. (2026). Experimental and theoretical investigation of optical transmittance in light- transmitting concrete. *Measurement Science and Technology*, https://doi.org/10.1088/1361-6501/ae6521

Arias-Erazo, J., Villaquirán-Caicedo, M. A., & Goyes, C. E. (2021). Ecological light transmiting concrete made from glass waste and acrylic sheets. *Construction and Building Materials*, *304*(124644). https://doi.org/10.1016/j.conbuildmat.2021.124644

Ashraf, S., & Rucka, M. (2023). Microcrack monitoring and fracture evolution of polyolefin and steel fibre concrete beams using integrated acoustic emission and digital image correlation techniques. *Construction and Building Materials*, *395*(June), 132306. https://doi.org/10.1016/j.conbuildmat.2023.132306

ASTM International, ASTM C109/C109M - 21—Standard test method for compressive strength of hydraulic cement mortars. Bureau of Indian Standards, 4031(Part 6), 3–7.

ASTM International, ASTM C1437-20. (2020). Standard Test Method for Flow of Hydraulic Cement Mortar. ASTM International.

ASTM International, ASTM C305-14. (2014). Standard Practice for Mechanical Mixing of Hydraulic Cement Pastes and Mortars of Plastic Consistency. 14(2), 147.

ASTM International, ASTM C348-21—Standard Test Method for Flexural Strength of of Hydraulic-Cement Mortars. Annual Book of ASTM Standards, 1–6.

ASTM International, ASTM C618-25. (2025). Specification for Coal Ash and Raw or Calcined Natural Pozzolan for Use in Concrete. ASTM International.

Atmaja, D. S. E., Wibirama, S., Herliansyah, M. K., & Sudiarso, A. (2025). Comparative study of integral image and normalized cross-correlation methods for defect detection on Batik klowong fabric. *Results in Engineering*, *25*, 104124. https://doi.org/10.1016/j.rineng.2025.104124

Bado, M. F., & Casas, J. R. (2021). *A Review of Recent Distributed Optical Fiber Sensors Applications for Civil Engineering Structural Health Monitoring*. *1818*(21). https://doi.org/https://doi.org/10.3390/s21051818

Bai, J., Zhang, W., Tian, J., Wu, X., & Zheng, M. (2024). Development of Optical Fiber Light-Transmitting Concrete (LTC)—A Review. *Buildings*, *15*(1), 104. https://doi.org/10.3390/buildings15010104

Baranikumar, A., Torrence, C. E., & Grasley, Z. (2021). Temperature dependence of viscoelastic Poisson's ratio of cement mortar. *Materials and Structures*, *54*(3), 101. https://doi.org/10.1617/s11527-021-01693-y

Bashbash, B. F., Alqedra, M. A., Hajrus, R. M., & Wafi, D. F. (2013). Basics of Light Transmitting Concrete. *Global Advanced Research Journal of Engineering, Technology and Innovation*, *2*(3), 76–083. https://doi.org/10.13140/RG.2.2.30481.33121

Beesley, P. (2010). *Liminal responsive Architecture*.

Belay, G. Y., Kinds, Y., Goossens, L., Gurung, K., Bosmans, N., Diltoer, R., … Van Erps, J. (2022). Dynamic optical beam shaping system to generate Gaussian and top-hat laser beams of various sizes with circular and square footprint for Additive Manufacturing applications. *Procedia CIRP*, *111*, 75–80. Elsevier B.V. https://doi.org/10.1016/j.procir.2022.08.134

Benezet, J. C., & Benhassaine, A. (1999). The influence of particle size on the pozzolanic reactivity of quartz powder. *Powder Technology*, *103*(1), 26–29. https://doi.org/10.1016/s0032-5910(99)00010-8

Born M & Wolf E. *Principles of Optics: Electromagnetic Theory of Propagation, Interference and Diffraction of Light*. 7th ed. Cambridge University Press; 1999.

Bremer, K., Wollweber, M., Weigand, F., Rahlves, M., Kuhne, M., Helbig, R., & Roth, B. (2016). Fibre Optic Sensors for the Structural Health Monitoring of Building Structures. *Procedia Technology*, *26*, 524–529. https://doi.org/10.1016/j.protcy.2016.08.065

Canadian Standards Association – *CSA A3000: Cementitious materials compendium*. (2018).

Chang, H., Kong, Z., Fan, S., Cai, Y., Guo, F., Ran, Q., … Feng, P. (2025). Investigation of fracture property of the fiber-reinforced cementitious composites casted using a novel fiber orientation method. *Cement and Concrete Composites*, *161*, 106111. https://doi.org/10.1016/j.cemconcomp.2025.106111

Chen, H., Wang, P., Pan, J., Lawi, Abubakar. S., & Zhu, Y. (2021). Effect of alkali-resistant glass fiber and silica fume on mechanical and shrinkage properties of cement-based mortars. *Construction and Building Materials*, *307*, 125054. https://doi.org/10.1016/j.conbuildmat.2021.125054

Chiadighikaobi, P. C., Adegoke, M. A., Kharun, M., Paul, V. J., Abu Mahadi, M. I., & Finbarrs-Ezema, B. (2023). A Review of the Structural Properties of Translucent Concrete as Sustainable Material. *The Open Construction & Building Technology Journal*, *17*(1). https://doi.org/10.2174/0118748368268119231003055958

Chiew, S. M., Ibrahim, I. S., & Mohd Ariffin, M. A. (2024a). Compressive Strength of Light-Transmitting Concrete (LTC) Incorporated with Optical Fibre. In N. Sabtu (Ed.), *Proceedings of AWAM International Conference on Civil Engineering 2022—Volume 2* (pp. 311–326). Singapore: Springer Nature Singapore. https://doi.org/10.1007/978-981-99-6018-7_23

Chiew, S. M., Ibrahim, I. S., & Mohd Ariffin, M. A. (2024b). Natural light transmittance of light-transmitting concrete (LTC) incorporated with optical fibres. *Materials Today: Proceedings*, *110*, 27–32. https://doi.org/10.1016/j.matpr.2023.08.131

Chiew, S. M., Ibrahim, I. S., Mohd Ariffin, M. A., Lee, H. S., & Singh, J. K. (2021). Development and properties of light-transmitting concrete (LTC) – A review. *Journal of Cleaner Production*, *284*. https://doi.org/10.1016/j.jclepro.2020.124780

Chiew, S. M., Ibrahim, I. S., Mohd Ariffin, M. A., Lee, H. S., & Singh, J. K. (2023). Assessment and ANN model development of natural light transmittance of light-transmitting concrete. *Results in Engineering*, *20*. https://doi.org/10.1016/j.rineng.2023.101416

Chiew, S. M., Ibrahim, I. S., Rus, A. Z. M., Fadzir, M. A. M., & Abd Rabbi, M. A. (2025). Preliminary study on influence of UV radiation on the light transmittance of light-transmitting concrete. *Journal of Cleaner Production*, *521*, 146262. https://doi.org/10.1016/j.jclepro.2025.146262

Chiew, S. M., Ibrahim, I. S., Sarbini, N. N., Ariffin, M. A. M., Lee, H. S., & Singh, J. K. (2020). Development of light-transmitting concrete—A review. *Materials Today: Proceedings*, *39*, 1046–1050. https://doi.org/10.1016/j.matpr.2020.05.166

Chiew, S., Syahrizal Ibrahim, I., Azreen Mohd Ariffin, M., Lee, H. S., & Kumar Singh, J. (2022). Evaluation of light transmittance performance of light-transmitting concrete with optical fibre. *Construction and Building Materials*, *351*(July), 128949. https://doi.org/10.1016/j.conbuildmat.2022.128949

Cui, X., Li, R., Li, Z., Xu, Z., Huang, J., & Fang, Z. (2025). Fabrication of superhydrophobic insulation surfaces on PMMA by nanosecond-pulsed DBD in filamentary-homogeneous mixed mode. *Surfaces and Interfaces*, *60*, 106043. https://doi.org/10.1016/j.surfin.2025.106043

D'Amore, A., Stella, J. A., Wagner, W. R., & Sacks, M. S. (2010). Characterization of the complete fiber network topology of planar fibrous tissues and scaffolds. *Biomaterials*, *31*(20), 5345–5354. https://doi.org/10.1016/j.biomaterials.2010.03.052

Dadavali, D., & Reddy, D. S. R. (2025). *EXPERIMENTAL STUDY OF LIGHT TRANSMITTING CONCRETE (LITRACON) USING VARIOUS PERCENTAGES OF OPTICAL FIBRES*. *13*(1).

Damineli, B. L., Kemeid, F. M., Aguiar, P. S., & John, V. M. (2010). Measuring the eco-efficiency of cement use. *Cement and Concrete Composites*, *32*(8), 555–562. https://doi.org/10.1016/j.cemconcomp.2010.07.009

Delnavaz, M., Najari, S., Hashemian, S. P., & Amiri, S. (2026). A comprehensive study on the integration of light-transmitting concrete in optimizing energy efficiency in buildings. *Environmental Progress & Sustainable Energy*, e70369. https://doi.org/10.1002/ep.70369

Dinesh, B. K., Mercy, S. R., & Suji, D. (2019). Effect of fiber pattern in strength of light transmitting concrete. *International Journal of Recent Technology and Engineering*, *7*(5), 736–739.

Drechsler, A., Frenzel, R., Caspari, A., Michel, S., Holzschuh, M., Synytska, A., … Mechtcherine, V. (2019). Surface Modification of Polymeric Fibers to Control the Interactions with Cement-Based Matrices in Fiber-Reinforced Composites. *Key Engineering Materials*, *809*, 225–230. https://doi.org/10.4028/www.scientific.net/KEM.809.225

Dutta, M., Reeti, R., & Mandal, S. K. (2018). Light Transmitting and Self Cleansing Concrete as a Smart Building Material-a Review. *2018 International Conference on Smart City and Emerging Technology (ICSCET)*, 1–5. Mumbai: IEEE. https://doi.org/10.1109/ICSCET.2018.8537328

Edris, W. F., Odah, E., Abu-Qasmieh, I., & Hendy, A. (2021). Mechanical properties of translucent concrete using plexiglass bars and fiberglass. *Civil Engineering and Architecture*, *9*(2), 293–300. https://doi.org/10.13189/cea.2021.090203

Emanet, S., & Arda Buyuktaskin, H. A. (2023). Mechanical Properties of Light-Transmitting Concrete and Its Durability Performance under the Effects of Accelerated Aging. *Journal of Testing and Evaluation*, *51*(5), 3273–3293. https://doi.org/10.1520/JTE20220412

Gagg, C. R. (2014). Cement and concrete as an engineering material: An historic appraisal and case study analysis. *Engineering Failure Analysis*, *40*, 114–140. https://doi.org/10.1016/j.engfailanal.2014.02.004

Gillen-Christandl, K., Gillen, G. D., Piotrowicz, M. J., & Saffman, M. (2016). Comparison of Gaussian and super Gaussian laser beams for addressing atomic qubits. *Applied Physics B: Lasers and Optics*, *122*(5). https://doi.org/10.1007/s00340-016-6407-y

Golewski, G. L. (2023). Mechanical properties and brittleness of concrete made by combined fly ash, silica fume and nanosilica with ordinary Portland cement. *AIMS Materials Science*, *10*(3), 390–404. https://doi.org/10.3934/matersci.2023021

Hai, N. M., Quang, P. D., & Nam, H. P. (2025). Evaluation of lighting energy savings and embodied carbon of light-transmitting concrete incorporating polymethyl methacrylate for building envelopes. *Journal of Building Engineering*, *112*, 113807. https://doi.org/10.1016/j.jobe.2025.113807

Han, B., Zhang, L., & Jinping, O. (2017). *B. Han, L. Zhang, and J. Ou, Smart and Multifunctional Concrete Towards Sustainable Infrastructures, 2017: Springer Singapore.*

Han, Y., Kim, D.-W., & Kwon, H.-J. (2012). Application of digital image cross-correlation and smoothing function to the diagnosis of breast cancer. *Journal of the Mechanical Behavior of Biomedical Materials*, *14*, 7–18. https://doi.org/10.1016/j.jmbbm.2012.05.007

Hapenciuc, A. D., Banescu, O., & Mihai, A. (2016). Responsive Interior Architecture—Interactive Surfaces. *3rd International Multidisciplinary Scientific Conference on Social Sciences and Arts SGEM 2016, Book 4*, *2*(SGEM2016 Conference Proceedings, ISBN 978-619-7105-54-4 / ISSN 2367-5659), 563–570.

Hassan, A. M. S., Shoukry, H., Perumal, P., Abd El-razik, M. M., Aly, R. M. H., & Alzahrani, A. M. Y. (2023). Evaluation of the thermo-physical, mechanical, and fire resistance performances of limestone calcined clay cement (LC3)-based lightweight rendering mortars. *Journal of Building Engineering*, *71*(April), 106495. https://doi.org/10.1016/j.jobe.2023.106495

Hecht, E. (2017). *Optics* (5 ed). Boston: Pearson Education, Inc.

Henriques, T. D. S., Dal Molin, D. C., & Masuero, Â. B. (2020). Optical fibers in cementitious composites (LTCM): Analysis and discussion of their influence when randomly arranged. *Construction and Building Materials*, *244*, 118406. https://doi.org/10.1016/j.conbuildmat.2020.118406

Henriques, T. dos S., Dal Molin, D. C., & Masuero, Â. B. (2018). Study of the influence of sorted polymeric optical fibers (POFs) in samples of a light-transmitting cement-based material (LTCM). *Construction and Building Materials*, *161*, 305–315. https://doi.org/10.1016/j.conbuildmat.2017.11.137

Henriques, T. dos S., Dal Molin, D. C., & Masuero, Â. B. (2020). Optical fibers in cementitious composites (LTCM): Analysis and discussion of their influence when randomly arranged. *Construction and Building Materials*, *244*, 118406. https://doi.org/10.1016/j.conbuildmat.2020.118406

Hirsch, L., Rossmy, B., & Butz, A. (2021). Shaping Concrete for Interaction. *TEI 2021 - Proceedings of the 15th International Conference on Tangible, Embedded, and Embodied Interaction*. https://doi.org/10.1145/3430524.3440625

Huang, B. (2020). Light transmission performance of translucent concrete building envelope. *Cogent Engineering*, *7*(1). https://doi.org/10.1080/23311916.2020.1756145

Huang, B., & Lu, W. (2020). Experimental investigation of the multi-physical properties of an energy efficient translucent concrete panel for a building envelope. *Applied Sciences (Switzerland)*, *10*(19), 1–16. https://doi.org/10.3390/app10196863

Huang, B., Wang, Y., Lu, W., & Cheng, M. (2022). Fabrication and energy efficiency of translucent concrete panel for building envelope. *Energy*, *248*, 123635. https://doi.org/10.1016/j.energy.2022.123635

Hunger, M., & Brouwers, H. J. H. (2009). Self-cleaning surfaces as an innovative potential for sustainable concrete. *Excellence in Concrete Construction through Innovation - Proceedings of the International Conference on Concrete Construction*, 545–552. https://doi.org/10.1201/9780203883440.ch81

Huong, O. W., & Kassim, U. (2019). *Translucent Concrete by Plastics Fibre Optics as A Sustainable Material That Benefit to Residential Building*. *6*(1).

Huynh Phuong Nam, Nguyen Minh Hai, Nguyen Van Huong, Pham Duc Quang, Nguyen Duc Tuan, Do Viet Hai, … Tran Quang Vy. (2022). Experimental study on 80 MPa grade light transmitting concrete with high content of optical fibers and eco-friendly raw materials. *Case Studies in Construction Materials*, *18*, e01810. https://doi.org/10.1016/j.cscm.2022.e01810

Inaudi, D., Posenato, D., & Glisic, B. (2005). *Combined static and dynamic monitoring of civil structures with long-gauge fiber optic sensors*. Presented at the 23rd International Modal Analysis Conference. Florida.

Jin, W., Caron, J.-F., & Ouellet-Plamondon, C. M. (2025). Minimizing the carbon footprint of 3D printing concrete: Leveraging parametric LCA and neural networks through multiobjective optimization. *Cement and Concrete Composites*, *157*, 105853. https://doi.org/10.1016/j.cemconcomp.2024.105853

John, E., Matschei, T., & Stephan, D. (2018). Nucleation seeding with calcium silicate hydrate – A review. *Cement and Concrete Research*, *113*, 74–85. https://doi.org/10.1016/j.cemconres.2018.07.003

Juan, S., & Zhi, Z. (2019). Preparation and Study of Resin Translucent Concrete Products. *Advances in Civil Engineering*, *2019*, 8196967. https://doi.org/10.1155/2019/8196967

Kasap, S. O. (2018). *Principles of electronic materials and devices* (Fourth edition). New York, NY: McGraw-Hill, a business unit of The McGraw-Hill Companies, Inc.

Kavitha Karthikeyan, Keerthana, & Shanmugapriya. (2016). Light Transmitting Mortar Blocks. *International Journal of Engineering Research And*, *V5*(02), IJERTV5IS020184. https://doi.org/10.17577/IJERTV5IS020184

Kenny, A., & Katz, A. (2015). Statistical relationship between mix properties and the interfacial transition zone around embedded rebar. *Cement and Concrete Composites*, *60*, 82–91. https://doi.org/10.1016/j.cemconcomp.2015.04.002

Kim, B. (2017). Light Transmitting Lightweight Concrete with Transparent Plastic Bar. *The Open Civil Engineering Journal*, *11*(1), 615–626. https://doi.org/10.2174/1874149501711010615

Larsen, L. K. (2015). *Feedforward and feedback modalities for embedded touch interaction with hi-fi systems*. Aarhus University.

Leung, C. K. Y., Wan, K. T., Inaudi, D., Bao, X., Habel, W., Zhou, Z., … Imai, M. (2015). Review: Optical fiber sensors for civil engineering applications. *Materials and Structures/Materiaux et Constructions*, *48*(4), 871–906. https://doi.org/10.1617/s11527-013-0201-7

Li, G., Su Win, N. S., Fan, M., Li, J., & Lin, L. (2025). Enhance registration precision of transmission breast images utilizing improved Levenberg-Marquardt optimization algorithm with normalized cross-correlation. *Computers in Biology and Medicine*, *186*, 109654. https://doi.org/10.1016/j.compbiomed.2025.109654

Li, L., Li, X., Wang, B., Tao, J., & Shi, K. (2025). A review on interfacial bonding behavior between fiber and concrete. *Journal of Building Engineering*, *105*, 112455. https://doi.org/10.1016/j.jobe.2025.112455

Li, M., Lu, Y., & Yang, S. (2022). Properties of Light-Transmitting Cementitious Materials. *ACI Materials Journal*, *119*(1), 39–45. https://doi.org/10.14359/51733147

Li, R., Yin, Z.-Y., & He, S.-H. (2025). 3D reconstruction of arbitrary granular media utilizing vision foundation model. *Applied Soft Computing*, *169*, 112599. https://doi.org/10.1016/j.asoc.2024.112599

Li, R., Yin, Z.-Y., He, S., & Sheil, B. (2025). Enhancement and assessment of large vision models for 3D particle reconstruction from X-ray tomography. *Canadian Geotechnical Journal*, *62*, 1–28. https://doi.org/10.1139/cgj-2024-0736

Li, Yan, Zhang, J., Cao, Y., Hu, Q., & Guo, X. (2021). Design and evaluation of light-transmitting concrete (LTC) using waste tempered glass: A novel concrete for future photovoltaic road. *Construction and Building Materials*, *280*, 122551. https://doi.org/10.1016/j.conbuildmat.2021.122551

Li, Yue, Li, J., & Guo, H. (2015a). Preparation and study of light transmitting properties of sulfoaluminate cement-based materials. *Materials and Design*, *83*, 185–192. https://doi.org/10.1016/j.matdes.2015.06.021

Li, Yue, Li, J., Wan, Y., & Xu, Z. (2015b). Experimental study of light transmitting cement-based material (LTCM). *Construction and Building Materials*, *96*, 319–325. https://doi.org/10.1016/j.conbuildmat.2015.08.055

Li, Yue, Xu, Z., Gu, Z., & Bao, Z. (2012). Research on the light transmitting cement mortar. *Advanced Materials Research*, *450–451*, 397–401. https://doi.org/10.4028/www.scientific.net/AMR.450-451.397

Lian, F., & Yin, Z. (2022). Mechanical, light transmittance properties and simulation study of sustainable translucent lightweight aggregate concrete. *Materials Research Express*, *9*(2). https://doi.org/10.1088/2053-1591/ac5552

LitraCon – light-transmitting concrete. Retrieved April 20, 2026, from https://www.litracon.hu/en

Liu, H., Feng, X., Liu, L., Li, T., & Tang, C. (2023). Mechanical properties and failure characteristics of anisotropic shale with circular hole under combined dynamic and static loading. *International Journal of Rock Mechanics and Mining Sciences*, *170*, 105524. https://doi.org/10.1016/j.ijrmms.2023.105524

Lone, U. A., Zhao, B., Fan, Y., & Zhou, Z. (2025). Experimental and numerical study on flexural properties of shredded prepreg carbon cloth waste fibre reinforced concrete. *Materials Today Sustainability*, *31*, 101149. https://doi.org/10.1016/j.mtsust.2025.101149

Losonczi, Á., & Bittis, A. (2005). Transparent concrete causing a sensation. *Betonwerk Und Fertigteil-Technik/Concrete Precasting Plant and Technology*, *71*(3), 66–69. Scopus. Retrieved from Scopus.

LUCEM Luccon. Retrieved April 20, 2026, https://lucem.com/

Luhar, I., Luhar, S., Savva, P., Theodosiou, A., Petrou, M. F., & Nicolaides, D. (2021). Light transmitting concrete: A review. *Buildings*, *11*(10), 1–18. https://doi.org/10.3390/buildings11100480

Luo, Y., Wang, X., Liao, Y., Fu, Q., Shu, C., Wu, Y., & He, Y. (2023). A Review of Homography Estimation: Advances and Challenges. *Electronics*, *12*(24), 4977. https://doi.org/10.3390/electronics12244977

Lyu, Q., Dai, P., & Chen, A. (2024). Mechanical strengths and optical properties of translucent concrete manufactured by mortar-extrusion 3D printing with polymethyl methacrylate (PMMA) fibers. *Composites Part B: Engineering*, *268*, 111079. https://doi.org/10.1016/j.compositesb.2023.111079

Lyu, X., Elchalakani, M., Wang, X., Sun, J., Huang, B., Saafi, M., … Wang, Y. (2024). Mechanical performance and anisotropic analysis of rubberised 3D-printed concrete incorporating PP fibre. *Environmental Science and Pollution Research*, *31*(36), 49100–49115. https://doi.org/10.1007/s11356-024-34437-w

Mahto, S., & Kujure, J. (2017). Light weight translucent concrete. *International Journal of Advances in Mechanical and Civil Engineering*, *4*(3), 112–115.

Mainini, A. G., Poli, T., Zinzi, M., & Cangiano, S. (2012). Spectral light transmission measure and radiance model validation of an innovative transparent concrete panel for façades. *Energy Procedia*, *30*, 1184–1194. https://doi.org/10.1016/j.egypro.2012.11.131

Makul, N. (2020). Advanced smart concrete—A review of current progress, benefits and challenges. *Journal of Cleaner Production*, *274*, 122899. https://doi.org/10.1016/j.jclepro.2020.122899

Marangu, J. M. (2020). Physico-chemical properties of Kenyan made calcined Clay - Limestone cement (LC3). *Case Studies in Construction Materials*, *12*. https://doi.org/10.1016/j.cscm.2020.e00333

Marin, P., Philippe, L., & Blanchi, Y. (2014). *Interactive Concrete Surface: An exploration of smart materials*. (March). https://doi.org/10.5176/2301-394X

Marques, A. I., Morais, J., Morais, P., Veiga, M. D. R., Santos, C., Candeias, P., & Ferreira, J. G. (2020). Modulus of elasticity of mortars: Static and dynamic analyses. *Construction and Building Materials*, *232*, 117216. https://doi.org/10.1016/j.conbuildmat.2019.117216

Mbabazi, J., Luo, Z., Du, Q., Wang, Y., & Lyu, Q. (2026). Light-transmitting foamed concrete composites with tailored mechanical-optical-thermal functionality. *Journal of Building Engineering*, *119*, 115202. https://doi.org/10.1016/j.jobe.2026.115202

Mbabazi, J., Wang, Y., Luo, Z., Gao, L., Du, Q., & Lyu, Q. (2026). Structural and functional performance of 3D-printed light-transmitting foamed concrete with different cavity geometries and fiber orientations. *Structures*, *87*, 111769. https://doi.org/10.1016/j.istruc.2026.111769

Meng, L., Ding, L., Pu, Y., Wang, X., Mushtaq, R. T., Alkahtani, M., & Shakeel, M. (2025). Optimizing 2D irregular packing via image processing and computational intelligence. *Scientific Reports*, *15*(1), 12320. https://doi.org/10.1038/s41598-025-97202-0

Meng, T., Ying, K., Yu, H., & Hong, Y. (2022). An approach to effectively improve the interfacial bonding of paste–limestone by incorporating different nanomaterials. *Composites Part B: Engineering*, *242*, 110046. https://doi.org/10.1016/j.compositesb.2022.110046

Merzbacher, C. I., Kersey, A. D., & Friebele, E. J. (1996). Fiber optic sensors in concrete structures: A review. *Smart Materials and Structures*, *5*(2), 196–208. https://doi.org/10.1088/0964-1726/5/2/008

Momin, A. A., Kadiranaikar, R. B., Jagirdar, V., & Inamdar, A. (2014). Study on Light Transmittance of Concrete Using Optical Fibers and Glass Rods. *IOSR Journal of Mechanical and Civil Engineering*, 67–72.

Mukherjee, A., Deepmala, Srivastava, P., & Sandhu, J. K. (2023). Application of smart materials in civil engineering: A review. *Materials Today: Proceedings*, *81*(2), 350–359. https://doi.org/10.1016/j.matpr.2021.03.304

Nam, H. P., Hai, N. M., Tuan, N. D., Quang Huy, L., Quang, P. D., Van Huong, N., & Hai, D. V. (2025). Mechanical, permeability, and optical properties of concrete integrating light-transmitting materials with high contents and large diameters. *Journal of Asian Architecture and Building Engineering*, *24*(6), 5380–5395. https://doi.org/10.1080/13467581.2024.2434537

Nam, H. P., Hai, N. M., Tuan, N. D., Quang, P. D., Van Huong, N., Huy, L. Q., & Hai, D. V. (2024). Experimental study of light transmitting concrete with ultra-high content of polymethyl methacrylate. *Construction and Building Materials*, *438*, 137156. https://doi.org/10.1016/j.conbuildmat.2024.137156

Nam, H. P., Hai, N. M., Van Huong, N., Quang, P. D., Tuan, N. D., Hai, D. V., … Vy, T. Q. (2022). Experimental study on 80 MPa grade light transmitting concrete with high content of optical fibers and eco-friendly raw materials. *Case Studies in Construction Materials*, *18*(e01810). https://doi.org/10.1016/j.cscm.2022.e01810

Navabi, D., Amini, Z., Rahmati, A., & Tahbaz, M. (2023). Case Studies in Construction Materials Developing light transmitting concrete for energy saving in buildings. *Case Studies in Construction Materials*, *18*, e01969. https://doi.org/10.1016/j.cscm.2023.e01969

Navabi, D., Javidruzi, M., Hafezi, M. R., & Mosavi, A. (2021). The high-performance light transmitting concrete and experimental analysis of using polymethylmethacrylate optical fibers in it. *Journal of Building Engineering*, *38*(July 2020), 102076. https://doi.org/10.1016/j.jobe.2020.102076

Pagliolico, S. L., Lo Verso, V. R. M., Torta, A., Giraud, M., Canonico, F., & Ligi, L. (2015). A preliminary study on light transmittance properties of translucent concrete panels with coarse waste glass inclusions. *Energy Procedia*, *78*, 1811–1816. https://doi.org/10.1016/j.egypro.2015.11.317

Palanisamy, C., Krishnaswami, N., kumar Velusamy, S., Krishnamurthy, H., kumaar Velmurugan, H., & Udhayakumar, H. (2022). Transparent concrete by using optical fibre. *Materials Today: Proceedings*, *65*, 1774–1778. https://doi.org/10.1016/j.matpr.2022.04.799

Pilipenko, A., Bazhenova, S., Kryukova, A., & Khapov, M. (2018). Decorative light transmitting concrete based on crushed concrete fines. *IOP Conference Series: Materials Science and Engineering*, *365*, 032046. https://doi.org/10.1088/1757-899X/365/3/032046

Potet, J., Gay, M., Bramerie, L., Simon, G., Saliou, F., Chanclou, P., & Joindot, M. (2025). Analytical study of receivers performances for 100 Gbit/s OOK IM/DD fiber access link. *Optical Fiber Technology*, *97*, 104502. https://doi.org/10.1016/j.yofte.2025.104502

Pourkazemi, M., Vahdati, M., Mirvalad, S., & Mahdikhani, M. (2024). Light-transmitting concrete: Performance and novel casting methods. *Construction and Building Materials*, *449*, 138270. https://doi.org/10.1016/j.conbuildmat.2024.138270

Qiao, H., Lin, Z., Sun, X., Li, W., Zhao, Y., & Guo, C. (2023). Fiber Optic-Based Durability Monitoring in Smart Concrete: A State-of-Art Review. *Sensors*, *23*(18), 7810. https://doi.org/10.3390/s23187810

Rativa, D., & Vohnsen, B. (2011). Single- and multimode characteristics of the foveal cones: The super-Gaussian function. *Journal of Modern Optics*, *58*(19–20), 1809–1816. https://doi.org/10.1080/09500340.2011.573879

Robles, A., Arenas, G. F., & Stefani, P. M. (2020). Light transmitting cement-based material (LTCM) as a green material for building. *Journal of Applied Research in Technology & Engineering*, *1*(1), 9. https://doi.org/10.4995/jarte.2020.13832

Rong, T. C., Mei, C. S., Al-Fasih, M. Y. M., Ibrahim, I. S., Sarbini, N. N., & Padil, K. H. (2023). LIGHT-TRANSMITTING CONCRETE PROPERTIES OF SHORT WALL PANEL. *ASEAN Engineering Journal*, *13*(1), 109–117. https://doi.org/10.11113/aej.V13.18433

Roye, A., Barlé, M., Janetzko, S., & Gries, T. (2009). Faser—Und textilbasierte Lichtleitung in Betonbauteilen—Lichtleitender Beton. *Beton- Und Stahlbetonbau*, *104*(2), 121–126. https://doi.org/10.1002/best.200808235

Sahana, T R Chandana, G N Manoj, H J Ajay, M S Tarun, & A Uma. (2023). An Experimental Study of Transparent Concrete by Using Optical Fibers. *International Journal for Research in Applied Science and Engineering Technology*, *11*(6), 3590–3597. https://doi.org/10.22214/ijraset.2023.54243

Said, S. H. (2020). State-of-the-art developments in light transmitting concrete. *Materials Today: Proceedings*, *33*, 1967–1973. https://doi.org/10.1016/j.matpr.2020.06.128

Saleem, M., Elshami, M. M., & Najjar, M. (2017). Development, Testing, and Implementation Strategy of a Translucent Concrete-Based Smart Lane Separator for Increased Traffic Safety. *Journal of Construction Engineering and Management*, *143*(5), 1–8. https://doi.org/10.1061/(asce)co.1943-7862.0001240

Saleh, B. E. A., & Teich, M. Carl. (2019). *Fundamentals of photonics*. Wiley.

Salvador-Herranz, G., Contero, M., & Camba, J. (n.d.). *Use of Tangible Marks with Optical Frame Interactive Surfaces in Collaborative Design Scenarios Based on Blended Spaces*.

Sangeetha, S. P., Subathra, P., Divahar, R., & Aravind Raj, P. S. (2022). Strength and light transmitting characteristics of translucent concrete using plastic optic fibers. *Journal of Building Pathology and Rehabilitation*, *7*(1), 1–10. https://doi.org/10.1007/s41024-022-00195-w

Sawant, A. B., Jugdar, R. V., & Sawant, S. G. (2014). Light Transmitting Concrete by using Optical Fiber. *International Journal of Inventive Engineering and Sciences*, *3*(1).

Schöning, J., Hook, J., Motamedi, N., Olivier, P., Echtler, F., Brandl, P., … von Zadow, U. (2009). Building Interactive Multi-Touch Surfaces. *Journal of Graphics, GPU, and Game Tools*, *14*(3), 35–55. https://doi.org/10.1080/2151237x.2009.10129285

Scrivener, K. L., John, V. M., & Gartner, E. M. (2018). Eco-efficient cements: Potential economically viable solutions for a low-CO2 cement-based materials industry. *Cement and Concrete Research*, *114*(June), 2–26. https://doi.org/10.1016/j.cemconres.2018.03.015

Scrivener, K., Martirena, F., Bishnoi, S., & Maity, S. (2018). Calcined clay limestone cements (LC3). *Cement and Concrete Research*, *114*, 49–56. https://doi.org/10.1016/j.cemconres.2017.08.017

Shafei, B., Kazemian, M., Dopko, M., & Najimi, M. (2021). State-of-the-Art Review of Capabilities and Limitations of Polymer and Glass Fibers Used for Fiber-Reinforced Concrete. *Materials*, *14*(2), 409. https://doi.org/10.3390/ma14020409

Sharifi, S., Navabi, D., & Mosavi, A. (2023). Translucent Concrete: Comprehensive Review of Concepts, Recent Technologies and Advances in Light Transmitting Concrete. *SACI 2023 - IEEE 17th International Symposium on Applied Computational Intelligence and Informatics, Proceedings*, 685–691. Institute of Electrical and Electronics Engineers Inc. https://doi.org/10.1109/SACI58269.2023.10158620

Sharma, K., Devi, K., & Saini, N. (2025). Mechanical properties and optical efficiency of light-transmitting concrete using plastic optical fibre and industrial wastes. *Research on Engineering Structures and Materials*. https://doi.org/10.17515/resm2025-997me0703rs

Sharma, K., Devi, K., & Saini, N. (2026). Experimental Investigation on the Structural and Economic Feasibility of Light-Transmitting Concrete Using Industrial By-Products. *Journal of Building Material Science*, 58-76. https://doi.org/10.30564/jbms.v8i2.13455

Shealy, D. L., & Hoffnagle, J. A. (2005). Beam shaping profiles and propagation. *SPIE Conf. Laser Beam Shape VI*, *5876–13*.

Shen, J., & Zhou, Z. (2013). Some Progress on Smart Transparent Concrete. *Pacific Science Review*, *15*(1), 51–55.

Shen, J., & Zhou, Z. (2021). Light transmitting performance and energy-saving of plastic optical fibre transparent concrete products. *Indoor and Built Environment*, *30*(5), 635–649. https://doi.org/10.1177/1420326X20903368

Shen, J., Li, M., Zheng, M., Liu, J., & Wang, S. (2026). Experimental and numerical investigation of heat transfer, daylighting, and thermal comfort of light-transmitting concrete (LTC) wall. *Case Studies in Construction Materials*, *24*, e05889. https://doi.org/10.1016/j.cscm.2026.e05889

Shenoy, A., Nayak, G., Tantri, A., & Shetty, K. K. (2022). Thermal transmission characteristics of plastic optical fibre embedded light transmitting concrete. *Materials Today: Proceedings*, *65*, 1759–1773. https://doi.org/10.1016/j.matpr.2022.04.798

Shenoy, A., Nayak, G., Tantri, A., Shetty, K. K., & Mahesha, M. G. (2025). Characterization of light-transmitting concrete incorporating bundled optical fibres. *Innovative Infrastructure Solutions*, *10*(1), 8. https://doi.org/10.1007/s41062-024-01794-x

Shenoy, A., Nayak, G., Tantri, A., Shetty, K. K., & Shendkar, M. R. (2023). Annual Transmittance Behavior of Light-Transmitting Concrete with Optical Fiber Bundles. *Materials*, *16*(21). https://doi.org/10.3390/ma16217037

Singh, T., Bhatnagar, D. J., & Singh, D. A. (2023). LABORATORY RESEARCH ON TRANSLUCENT CONCRETE USING OPTICAL FIBRE. *The Genesis*, *10*(4). https://doi.org/http://doi.org/10.47211/tg.2023.v10i04.011

Snoeck, D., Debo, J., & De Belie, N. (2020). Translucent self-healing cementitious materials using glass fibers and superabsorbent polymers. *Developments in the Built Environment*, *3*(April), 100012. https://doi.org/10.1016/j.dibe.2020.100012

Sobo, C. A., Farooq, S., & Azhar, S. (2021). Plastic Fiber Optics Embedded in Concrete (to study its Light-Transmitting Properties) for Sustainable and Economical Buildings. *Mehran University Research Journal of Engineering and Technology*, *40*(2), 399–414. https://doi.org/10.22581/muet1982.2102.14

Spiesz, P., Rouvas, S., & Brouwers, H. J. H. (2016). Utilization of waste glass in translucent and photocatalytic concrete. *Construction and Building Materials*, *128*, 436–448. https://doi.org/10.1016/j.conbuildmat.2016.10.063

Štochl, N., Vychytil, J., & Hájek, P. (2023). Illumination of Interior Spaces through Structures Made of Unified Slabs of High-Performance Light-Transmitting Concrete with Embedded Optical Fibers. *Materials*, *16*(8). https://doi.org/10.3390/ma16083142

Stutzman, P. E., & Clifton, J. R. (1999). SPECIMEN PREPARATION for SCANNING ELECTRON MICROSCOPY. *Twenty-First International Conference on Cement Microscopy*, 10–22.

Su, X., Zhang, L., & Liu, Z. (2023). Daylighting and energy performance of the combination of optical fiber based translucent concrete walls and windows. *Journal of Building Engineering*, *67*(January), 105959. https://doi.org/10.1016/j.jobe.2023.105959

Su, X., Zhang, L., Liu, Z., Luo, Y., Lian, J., & Liang, P. (2020). Daylighting performance simulation and analysis of translucent concrete building envelopes. *Renewable Energy*, *154*, 754–766. https://doi.org/10.1016/j.renene.2020.03.041

Su, X., Zhang, L., Liu, Z., Luo, Y., Liang, P., & Lian, J. (2022). An optical and thermal analysis of translucent concrete considering its dynamic transmittance. *Journal of Cleaner Production*, *364*, 132588. https://doi.org/10.1016/j.jclepro.2022.132588

Su, X., Zhang, L., Luo, Y., & Liu, Z. (2022). Energy & Buildings An energy analysis of translucent concrete embedded with inclined optical fibers. *Energy & Buildings*, *273*, 112409. https://doi.org/10.1016/j.enbuild.2022.112409

Subathra, P., & Sangeetha, S. P. (2020). Study on pellucid concrete incorporating optical fibers–a review. *Materials Today: Proceedings*, *45*, 6682–6686. https://doi.org/10.1016/j.matpr.2020.12.110

Supriya, Chaudhury, R., Sharma, U., Thapliyal, P. C., & Singh, L. P. (2023). Low-CO2 emission strategies to achieve net zero target in cement sector. *Journal of Cleaner Production*, *417*, 137466. https://doi.org/10.1016/j.jclepro.2023.137466

Taheri, S. (2019). A review on five key sensors for monitoring of concrete structures. *Construction and Building Materials*, *204*, 492–509. https://doi.org/10.1016/j.conbuildmat.2019.01.172

Tahwia, A. M., Abdelaziz, N., Samy, M., & Amin, M. (2022). Mechanical and light transmittance properties of high-performance translucent concrete. *Case Studies in Construction Materials*, *17*(June), e01260. https://doi.org/10.1016/j.cscm.2022.e01260

Tahwia, A. M., Abdel-Raheem, A., Abdel-Aziz, N., & Amin, M. (2021). Light transmittance performance of sustainable translucent self-compacting concrete. *Journal of Building Engineering*, *38*, 102178. https://doi.org/10.1016/j.jobe.2021.102178

Tang, S., Liu, X. Y., & Strom, C. S. (2009). Producing Supramolecular Functional Materials Based on Fiber Network Reconstruction. *Advanced Functional Materials*, *19*(14), 2252–2259. https://doi.org/10.1002/adfm.200801590

Theodosiou, A., & Kalli, K. (2020). Recent trends and advances of fibre Bragg grating sensors in CYTOP polymer optical fibres. *Optical Fiber Technology*, *54*(November 2019), 102079. https://doi.org/10.1016/j.yofte.2019.102079

Tuaum, A., Shitote, S. M., & Oyawa, W. O. (2018). *Experimental Evaluation on Light Transmittance Performance of Translucent Concrete*. *13*(2).

Tuaum, A., Shitote, S., Oyawa, W., & Biedebrhan, M. (2019). Structural Performance of Translucent Concrete Façade Panels. *Advances in Civil Engineering*, *2019*(1), 4604132. https://doi.org/10.1155/2019/4604132

Urmila M Bhanuse, Abhijeet B Babar, & Anil C Ranveer. (2015). Smart Light Translucent Concrete By Using Optical Fiber. *Journal of Environmental Science, Computer Science and Engineering & Technology*, *5*(1), 10–18.

Wang, C., Ding, Y., Cui, K., Li, J., Xu, Q., & Mei, J. (2025). A Perspective Distortion Correction Method for Planar Imaging Based on Homography Mapping. *Sensors*, *25*(6), 1891. https://doi.org/10.3390/s25061891

Wang, L., Li, J., Hao, J., Sai, Y., & Liu, X. (2022). Crack width estimate in reinforced concrete with FBG sensor: Experimental and numerical analysis. *Optoelectronics Letters*, *18*(1), 43–47. https://doi.org/10.1007/s11801-022-1027-8

Wang, S. F., Zhang, J., Luo, D. W., Gu, F., Tang, D. Y., Dong, Z. L., … Kong, L. B. (2013). Transparent ceramics: Processing, materials and applications. *Progress in Solid State Chemistry*, *41*(1–2), 20–54. https://doi.org/10.1016/j.progsolidstchem.2012.12.002

Yoshizaki, R., & Nakao, M. (2023). Ultrashort pulse laser processing of single crystalline diamond for efficient and smooth grooving with top-hat beam modulation. *CIRP Annals*, *72*(1), 189–192. https://doi.org/10.1016/j.cirp.2023.04.001

Zeng, H., Deng, X., & Hu, Z. (2008). A new normalized method on line-based homography estimation. *Pattern Recognition Letters*, *29*(9), 1236–1244. https://doi.org/10.1016/j.patrec.2008.01.031

Zhang, F., Li, B., Zhang, X., Guo, P., Guo, L., & Gong, X. (2024). A highly sensitive fiber-tip temperature sensor based on enhanced Fresnel reflection induced by modified materials. *Ceramics International*, *50*(9), 16463–16473. https://doi.org/10.1016/j.ceramint.2024.02.131

Zhang, X., Long, L., Broere, W., & Bao, X. (2025). Smart sensing of concrete crack using distributed fiber optics sensors: Current advances and perspectives. *Case Studies in Construction Materials*, *22*, e04493. https://doi.org/10.1016/j.cscm.2025.e04493

Zhao, C.-L., Li, J., Zhang, S., Zhang, Z., & Jin, S. (2013). Simple Fresnel Reflection-Based Optical Fiber Sensor for Multipoint Refractive Index Measurement Using an AWG. *IEEE Photonics Technology Letters*, *25*(6), 606–608. https://doi.org/10.1109/LPT.2013.2243833

Zheng, Z., Liang, H., Hua, B.-S., Wong, Y. H., Ang, P., Yi Chui, A. P., & Yeung, S.-K. (2024). CoralSCOP: Segment any COral Image on this Planet. *2024 IEEE/CVF Conference on Computer Vision and Pattern Recognition (CVPR)*, 28170–28180. Seattle, WA, USA: IEEE. https://doi.org/10.1109/CVPR52733.2024.02661

Zhou, Z., Ou, G., Hang, Y., Chen, G., & Ou, J. (2009). Research and development of plastic optical fiber based smart transparent concrete. *Smart Sensor Phenomena, Technology, Networks, and Systems 2009*, *7293*, 72930F. SPIE. https://doi.org/10.1117/12.816638

Zhu, C., Li, D., Zhang, S., Jiao, H., Guo, J., & Chen, X. (2025). Optimal mix ratio and numerical simulation study of concrete modified by nano-silica synergistically reinforced with basalt fibers. *Polymer Testing*, *150*, 108913. https://doi.org/10.1016/j.polymertesting.2025.108913